Thesis for the Degree of Doctor of Philosophy

Towards quantitative single cell analysis using optical tweezers and microfluidics

Emma Eriksson

UNIVERSITY OF GOTHENBURG

Department of Physics
UNIVERSITY OF GOTHENBURG
Gothenburg, Sweden 2009

TITLE: Towards quantitative single cell analysis using optical tweezers and microfluidics

EMMA ERIKSSON
ISBN 978-91-628-7751-4
Internet-ID: http://hdl.handle.net/2077/19485

Cover picture: *S. cerevisiae* expressing Hog1-GFP stressed with
1 M sorbitol trapped with holographic optical tweezers.

Department of Physics
University of Gothenburg
SE-412 96 Gothenburg, Sweden
Phone +46-(0)31-7721000

Typeset using LaTeX.

Printed by Chalmers Reproservice
Gothenburg, Sweden 2009

TOWARDS QUANTITATIVE SINGLE CELL ANALYSIS USING OPTICAL TWEEZERS AND MICROFLUIDICS

Emma Eriksson
Department of Physics, University of Gothenburg

Abstract

Experiments on single cells have the potential to uncover information that would not be possible to obtain with traditional biological techniques, which only reflect the average behavior of a population of cells. In the averaging process, information regarding heterogeneity and cellular dynamics, that may give rise to a nondeterministic behavior at the population level, is lost. In this thesis I have demonstrated how optical tweezers, microfluidics and fluorescence microscopy can be combined to acquire images with high spatial and temporal resolution that allow quantitative information regarding the response of single cells to environmental changes to be extracted.

Two main approaches for achieving the environmental changes are presented, one where optically trapped cells are moved with respect to a stationary flow, and one where the fluid media are moved relative to cells positioned stationary on the bottom of a microfluidic device. Both approaches allow precise and reversible environmental changes to be performed. The first approach achieves environmental changes in less than 0.2 s, and is thus suited for studies of fast cellular processes. This is approximately ten times faster than the second approach, which is, however, more convenient for studies over longer periods of time where statistical information on a large number of individual cells are requested. The experimental approaches are verified on different signalling pathways in *Saccharomyces cerevisiae*, where the main focus is the HOG pathway. The cellular response is followed either via brightfield images, where the volume changes of cells are monitored, or through fluorescence images where the spatio-temporal distributions of GFP tagged proteins are extracted.

A possible approach to increase the throughput using stationary flows is demonstrated by introducing holographic optical tweezers, allowing several cells to simultaneously be trapped and exposed to environmental changes. Automated image analysis combined with 3D manipulation is shown to allow the temporal resolution to be increased, or enable studies over longer periods of time thanks to the reduced photobleaching.

Keywords: Optical tweezers, holographic optical tweezers, microfluidics, lab-on-a-chip, fluorescence microscopy, spatial light modulator, single cell analysis, quantitative systems biology, GFP, *Saccharomyces cerevisiae.*

Appended Papers

This thesis is based on the work described in the following papers:

I. **A microfluidic system in combination with optical tweezers for analyzing rapid and reversible cytological alterations in single cells upon environmental changes**
E. Eriksson, J. Enger, B. Nordlander, N. Erjavec, K.Ramser, M.Goksör, S. Hohmann, T. Nyström and D. Hanstorp
Lab on a Chip, **7**, 71-76 (2007).

II. **Optical manipulation and microfluidics for studies of single cell dynamics**
E. Eriksson, J. Scrimgeour, A. Granéli, K. Ramser, R. Wellander, J. Enger, D. Hanstorp and M. Goksör
Journal of Optics A: Pure and Applied Optics **9**, S113-S121 (2007).

III. **Holographic optical tweezers combined with a microfluidic device for exposing cells to fast environmental changes**
E. Eriksson, J. Scrimgeour, J. Enger, M. Goksör
Proceedings of SPIE, Vol. **6592**, 65920P (2007).

IV. **The effect of external forces on discrete motion within holographic optical tweezers**
E. Eriksson, S. Keen, J. Leach, M. Goksör and M. J. Padgett
Optics Express **15**(26), p. 18268-18274 (2007).

V. **Automated focusing of nuclei for time lapse experiments on single cells using holographic optical tweezers**
E. Eriksson, D. Engström, J. Scrimgeour, and M. Goksör
Optics Express, **17**(7), p. 5585-5594, (2009).

VI. **An experimental approach for quantitative studies of single cells in dynamically changing environments**
E. Eriksson, K. Sott, F. Lundqvist, M. Sveningsson, J. Scrimgeour, D. Hanstorp, M. Goksör and A. Granéli
In manuscript.

VII. **Biophysical properties of *Saccharomyces cerevisiae* and their relation to HOG pathway activation**
J. Schaber, M. Àngel Adrover, **E. Eriksson**, S. Pelet, E. Petelenz, D. Klein, F. Posas, M. Goksör, M. Peter, S. Hohmann, E. Klipp
In manuscript.

My contributions to the appended papers:

Paper I. I designed the experimental setup and performed the biological experiments together with Jonas Enger. I performed the evaluation of the microfluidic device and the image analysis. I wrote the paper.

Paper II. I developed the design of the microfluidic device and performed the numerical simulations of the microfluidic device. I also performed the experiments on yeast subjected to osmotic stress. I wrote parts of the paper.

Paper III. I performed the experiments and wrote the paper.

Paper IV. I performed the experiments together with Stephen Keen, I performed the data analysis, and I wrote the paper together with Stephen Keen.

Paper V. I performed the experiments and wrote the paper.

Paper VI. I designed and built the experimental setup, including the design of the microfluidic device based on numerical simulations. Further, I wrote the programs for controlling and synchronizing the different events in the experiments. I also evaluated the device experimentally using solutions containing fluorescein. Finally, I wrote the Materials and Methods, Results, Discussion and Conclusion together with Dr. Kristin Sott.

Paper VII. I designed and built the experimental setup, and performed the measurements and image analysis for data set no 2. The experiments were performed together with Elzbieta Petelenz. I wrote the corresponding sections of the paper.

Scientific publications which are not included in this thesis:

- **Optical systems for single cell analyses**
  K. Sott, **E. Eriksson**, E. Petelenz and M. Goksör
  Expert Opinion in Drug Discovery, **3**(11), p. 1323-1344, (2008)

- **Improved beam steering accuracy of a single beam with a 1D phase-only spatial light modulator**
  D. Engström, J. Bengtsson, **E. Eriksson**, and M. Goksör
  Optics Express **16**(22), p. 18275-18287 (2008).

- **Acquisition of single cell data in an optical microscope**
  K. Sott, **E. Eriksson**, and M. Goksör
  Lab-on-a-Chip Technology: Biomolecular Separation and Analysis, Caister Academic Press (2009).

- **Steering accuracy of a spatial light modulator-based single beam steerer: guidelines and limitations**
  D. Engström, J.Bengtsson, **E. Eriksson** and M. Goksör
  Proceedings of SPIE, Vol. **7038**, 703829 (2008).

- **Visualizing cellular heterogeneity**
  K. Sott, **E. Eriksson**, and M. Goksör
  Proceedings of the Asia Optical Fiber Communication and Optoelectronic Exhibition and Conference (2008).

- **Lab-on-a-chip: The future of single cell analysis?**
  E. Eriksson, J. Scrimgeour, M. Goksör
  Proceedings of the Fourth International WLT-Conference on Lasers in Manufacturing 2007, Munich, (2007).

- **Laser Surgery for Microbiological Research**
  J. Scrimgeour, **E. Eriksson** and M. Goksör
  Methods in Cell Biology - Laser Manipulation of Cells and Tissues, **82** p. 629-646 Academic Press, 2007.

- **Dielectrophoresis-Induced Separation of Metallic and Semiconducting Single-Wall Carbon Nanotubes in a Continuous Flow Microfluidic System**
  M. Mattsson, A. Gromov, S. Dittmer, **E. Eriksson**, O.A. Nerushev and E.E.B. Campbell
  Journal of Nanoscience and Nanotechnology. **7**, 3431-343, (2007).

- **A micro-fluidic system for studies of stress response in single cells using optical tweezers**
  A. Granéli, **E. Eriksson**, J. Enger, K. Ramser, M. Goksör, S. Hohmann and D. Hanstorp
  Proceedings of SPIE, Vol. **6326**, 63260O (2006).

- **Sorting particles in a microfluidic system using SLM-reconfigurable intensity patterns** in *Imaging, Manipulation and Analysis of Biomolecules, Cells and Tissues*
  I. R. Perch-Nielsen, **E. Eriksson**, M. Goksör, J. Enger, P. J. Rodrigo, D. Hanstorp and J. Glückstad
  Proceedings of SPIE, Vol. **6088**, 60881H (2006).

Contents

Chapter 1

Introduction

As I started my graduate studies in 2004, experiments on the single cell level had just started to gain interest. The first review paper that I have found which summarizes single cell techniques is actually from that very year [1]. Today the field of single cell analysis is expanding rapidly [2, 3], where published papers are no longer only proof-of-concepts demonstrating that single cell experiments can be performed, but also showing robust systems where statistically relevant data can be collected.

So, why is there an interest in studying single cells rather than populations? In short, it has to do with the possibility to resolve intercellular heterogeneity that can have an impact on the overall behavior, but cannot be resolved by measuring the average response of a population. Obvious reasons for the existence of this heterogeneity are different genotypes and variations due to the cell cycle stage or age. Even in a monoclonal population, with the same history and in the same environment, different phenotypes can exist due to the stochastic nature of gene expression. This is often referred to as *genetic noise*, and stems from stochastic fluctuations in the transcription and translation processes in the cell. Such stochastic phenotypic variations would be hard, if not impossible, to resolve with techniques relying on average measurements on large populations of cells.

Traditional techniques for looking at gene expression or protein levels of cells are methods such as Northern and Western blotting, real-time PCR and microarrays. These are all based on measurements on populations of cells, are well established techniques in cell and molecular biology research and are relatively easy to use. However, they only provide information representing a snapshot of population averages. For example, Western blots can reveal how protein levels change over time, but each sampling point only represents the average protein level for a population of cells. Further, each

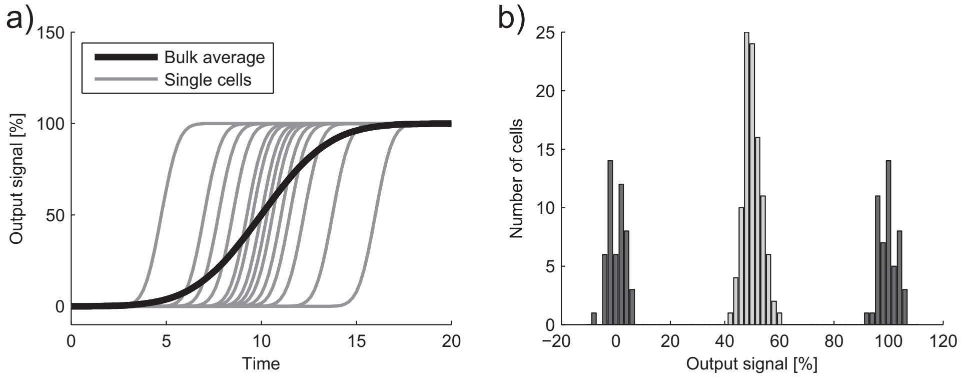

Figure 1.1: Two examples of how averaging techniques would be misleading. a) An example of how the average response (black) would lead to false conclusions regarding the kinetics of the cellular response. From the averaged response it looks as the cells respond quite slowly, while the individual cell responses (gray) reveal that the response is much quicker, but that there is a distribution among the cells in the timing of the response. b) The difference between cells responding in a gradual fashion (light gray) versus a binary response (dark gray).

time point is based on a different set of cells. In addition, the sampling is manual, which is time consuming and limits the time resolution. The average cell response is often useful for determining overall biological effects. Nevertheless, one should be aware that it only partly provides information regarding the true cellular response, since the response of each cell can vary as a consequence of its physiological and genetic state. Simply relying on an averaged result, rather than looking at the distribution, might even lead to false conclusions, e.g., in the case of a bimodal (or other non-normal) distribution of protein levels [4]. The average response of a population or subpopulation of cells could be misleading regarding both the kinetics and the actual averaged value. This is illustrated in figure 1.1 a), where the averaged response suggest that the cells respond quite slowly, while the individual cell responses reveal that the response is much quicker. However, there is a distribution among the cells in the timing of the response. In addition, looking at the averaged value at time 10, we would conclude that the cells have answered with 50% intensity, while the single cell responses reveal a bimodal distribution. Another example concerns whether the cells respond in a gradual (analogue) way or in an all-or-nothing (binary) fashion. Assume, for instance, an output signal measured to be 50% of the signal under a different condition. With a population averaging technique, it is difficult to distinguish between a situation where this result is due to all cells responding with 50% of the maximum intensity, or a situation where

50% of the cells respond with full intensity while the rest do not respond at all, as in figure 1.1 b). The population behavior can also be something in between these two extremes. Thus it is necessary to perform experiments on a single cell level, in order to determine how the cells really react and thus get a complete picture of how the cells function.

To understand how cells function on a single cell level, it is important to understand the intricate interplay between the proteins within the cell. An important step was the sequencing of the genomes of a multitude of organisms, including humans. However, the interpretation of the base pair sequences more or less only represents a list of the proteins that can be produced by the cell. Relevant questions are thus what the functions of those proteins are, when they are expressed, and in particular how they interact with each other in order for the cell (and ultimately the entire organism) to function properly. These kind of interactions are described by signalling transduction pathways, and the understanding of these pathways is crucial in order to understand how cells function. One particular class of pathways of importance for the work presented in this thesis, is pathways that are activated upon changes in the cell's external environment. In order to stay alive and healthy the cell needs to adjust to the new conditions through the activation and downregulation of the appropriate signalling pathways. By changing the environment in a controlled fashion while monitoring the cellular response, it is thus possible to get more insight into these pathways, ultimately resulting in a better understanding of the cell. Systems biology is an emerging field where the understanding of signalling pathways is one of the key components [5]. Systems biology aims for a better understanding of complex biological systems, via mathematical models used to simulate the behavior of the system. An important part is to gain insight into various biological processes, with the goal of predicting the system behavior from events on the molecular level. This includes the description of the network of signalling pathways within cells. To understand such pathways and mechanisms of signal propagation in cells, there is a growing need for quantitative experimental data, in particular on a single-cell level, measuring signal reactions with high spatial and temporal resolution.

One experimental technique commonly used for the acquisition of data on single cells is flow cytometry. Here, single cells in suspension are passed through a narrow measurement region, where the fluorescent properties, as well as the scattered light can be anlyzed. With an extension of the technique it is also possible to separate fractions of cells based on the previously measured properties. This is often referred to as FACS, Fluorescence Activated Cell Sorting. Even though noise in gene expression has been studied using flow cytometry [6, 7], there is no possibility to follow a specific cell over time. Instead, once the cell is measured, it is lost among the other cells. Flow cytometry can thus only provide snapshots of the distribution of fluorescence intensities among cells, but it cannot tell us about the spatial distribution of fluorescence in the cells, nor follow single cells over time. A technique that is often compared to flow cytometry is laser scanning cytometry (LSC) [8]. With LSC it is possible to extract information regarding the spatial localization of fluorescent proteins or probes and follow single cells over time, but not with the resolution provided with optical microscopy. LSC produces data comparable to flow cytometry data, but with a lower throughput and with limited sorting possibilities. The high throughput of flow cytometry enables large amounts of data to be obtained in a short period of time. However, in general there is a trade-off between the throughput and the amount of details that can be acquired about cells. Obtaining information regarding spatial localization of fluorescent probes with high resolution generally requires microscope images to be acquired and analyzed, which is more time-consuming compared to the measurements of fluorescence events with a detector, as in flow cytometry. Nevertheless, several research groups strive towards making single cell techniques, where it is possible to monitor single cells over time, more high throughput by allowing several cells to be studied in parallel [4, 9–12]. This is important, since even though the purpose of single cell analysis is to gain knowledge on the individual cell level, it is still necessary to perform the experiments on a statistically relevant number of cells. If too few cells are analyzed, there is a risk of drawing wrong conclusions, by interpreting the behavior of those few cells as the general behavior of the entire population [2]. A natural question is thus how many cells that should be studied. This question is difficult to answer, since techniques for the study of single cells have become available only recently and data acquired with those techniques is needed to reveal the variations in a population. The answer probably also depends on the type of cells and properties that are studied. The issues of throughput, high resolution and the possibility to study cell-to-cell variations (i.e., studying populations on a single cell basis) are listed as the current bottlenecks in building reliable models within the field of yeast systems biology in a recent review by Petranovic *et al.* from 2008 [13].

Today experiments on single cells with high resolution (both temporally and spatially) are performed. Those experiments are to a large extent possible thanks to the development of a variety of fluorescence based microscopy techniques with high precision microscope stages and sensitive cameras [14, 15], as well as the development of fluorescent proteins and other fluorescent probes [16, 17]. Fluorescent proteins possesses the unique feature that the gene encoding for the fluorescent protein can be fused to almost any gene of interest in the cell. Thus the corresponding protein will be tagged with the fluorescent protein, enabling the study of gene expression and to follow intracellular processes *in vivo*. The large impact of the green fluorescent protein (GFP) in cell biology and medicine was highlighted recently with the 2008 Nobel prize in chemistry [18].

With fluorescent proteins as reporters and sensitive fluorescence detection methods, it has become possible to study cellular heterogeneity among single living cells in both prokaryotic and eukaryotic cells [3]. In an elegant experiment, Elowitz *et al.* were able to study noise in eukaryotic gene expression by expressing two different fluorescent proteins (cyan fluorescent protein, CFP, and yellow fluorescent protein, YFP) from identical promoters on the same chromosome [19]. The noise could be further divided into intrinsic and extrinsic noise, where extrinsic noise arises from fluctuations in cellular components and is a global effect (but vary from one cell to another), while intrinsic noise arises from the stochasticity in the biochemical process of gene expression. The experiments demonstrated that noise in gene expression gives rise to fluctuations in protein levels in a clonal population of *Escherichia coli*, and that the relative contributions of extrinsic and intrinsic factors to the total noise vary with the expression level. Raser and O'Shea modified this method to measure gene expression in diploid yeast cells (*Saccharomyces cerevisiae*) [20]. Here it was found that noise in gene expression was dominated by extrinsic noise for all the gene promoters that were investigated. Using sensitive imaging techniques and fluorescent proteins it has also shown possible to probe gene expression and transcription factor dynamics in living *E. coli* bacteria one molecule at a time [21, 22]. Another recent example is a time-lapse study of single yeast cells, where the transcription factor Crz1, tagged with a fluorescent protein, was shown to exhibit short bursts of nuclear localization after the addition of extracellular calcium [23]. The calcium concentration modulated only the frequency of the localization bursts and not the duration. Across a population of cells, the average degree of nuclear localization would thus be interpreted as a partial adaptation to the raised extracellular calcium levels.

The local environment of the cells played a key role in the interpretation of the observed noise in these experiments. Lack of control of the extracellular microenvironment introduces experimental uncertainties that might increase the variation among cells and possibly even mask the feature under study. In some experiments it might be of interest to keep the chemical environment of the cells constant and homogenous. In other experiments, the possibility of changing it in a controlled manner offers new possibilities to study, for instance, signalling events within cells occurring upon environmental stimuli, thus providing insights into the regulatory mechanisms in living cells. For both purposes microfluidic devices have turned out to be extremely promising. Microfluidics is a research field that deals with the fabrication and applications of small channel systems, typically $10 - 500$ μm in width and height, where nano-liters of fluids can be handled. When fabricated in a transparent material these are well suited to be combined with fluorescence microscopy, allowing the cellular response to be monitored. By exploiting the properties of laminar flow in such small geometries it has shown possible to control the environment with high precision, both spatially and temporally [24]. It has even been demonstrated that it is possible to expose only parts of cells to a certain stimulus using a microfluidic device [25]. Another example that demonstrates both the unique feature of microfluidic devices to precisely control the environment and the importance of studying single cells is the mechanism of bacterial persistence. When bacteria are exposed to antibiotics a small fraction of the population survives without having acquired resistance genetically. However, when these bacteria are regrown they are as sensitive to antibiotics as the original population. This phenomenon, referred to as persistence, was discovered already in 1944 [26], and cannot be explained on a population level. By following individual *E. coli* bacteria in a microfluidic device, Balaban *et al.* were able to show that persistence was linked to pre-existing heterogeneity in the population existing even before the exposure to antibiotics [27]. They demonstrated that the persister cells had a reduced growth rate compared to normally growing cells. The switching between normally growing cells and persister cells, which allows a subpopulation of cells to survive the antibiotic treatment, could be described mathematically.

A number of recent studies have demonstrated the use of microfluidic devices for changing the environment around single cells, allowing the signalling pathways involved in the response to the environmental conditions in mind to be studied in detail, when combined with time-lapse fluorescence microscopy. Using a microfluidic system Mettetal *et al.* were able to study the frequency dependence of signal transduction in osmo-adaptation of single *S. cerevisiae* [28]. In a similar way Hersen *et al.* measured the bandwidth of the same signalling pathway responding to high osmolarity conditions [29]. The pathway was shown to act as a low-pass filter, averaging the signal when the extracellular medium changes rapidly and following it closely for slow changes. In those studies the environmental change was more or less in the form of square pulses, while Bennett *et al.* demonstrated a microfluidic device capable of subjecting a population of cells to a continuously varying supply of medium (e.g., ramping up the concentration or altering it in a sinusoidal fashion) [30]. With this device they were able to show that the metabolic system in yeast also acts as a low-pass filter. A high-throughput microfluidic imaging platform for studies of single-cell response to time-varying environmental conditions was demonstrated recently by Taylor *et al.* With this system they investigated the mating pheromone response in *S. cerevisiae*, and were able to identify dynamic phenotypes that are not observed in static environmental conditions.

Fluorescence microscopy is indeed an extremely useful tool for following the behaviour of single cells. Unfortunately, there is no possibility for the user to manipulate the cells; he or she is merely a passive observer. Introducing microfluidics offers some degree of cell manipulation possibilities, but essentially only by guiding the flow of cells to a certain region within the device [28–30]. In order to change the environment of cells, the cells' positions must be independent of the flow. This is often achieved by allowing the cells to attach to the bottom of the device through sedimentation, with small possibilities to control the exact positions of cells and the cell density. Attempts of incorporating cell trapping functions within microfluidic devices have been made [31–33], but still with limited possibilities of choosing what cells to be trapped and no means of dynamic positioning of cells relative to each other. However, such manipulation possibilities are provided by introducing optical tweezers. Already in the 1980's Arthur Ashkin demonstrated the possibility to use a single strongly focused laser beam - optical tweezers - for manipulating biological objects [34, 35]. Since then, optical tweezers have found widespread use within the life sciences for manipulating single cells or even single molecules as well as measuring adhestion forces in the sub pico-Newton range [36, 37]. The same microscope objective as is used for imaging can be used to focus the laser light forming the optical tweezers, allowing the microscopist to not only look at the cells but also to move them around in the sample. In contrast to many other micromanipulation techniques, optical tweezers are contact free and therefore allow sterile handling of samples. The technique is also easily combined with both microfluidic devices and most modern optical imaging techniques.

For the study of single cells, optical trapping have for instance been used to sort out bacterial viability [38], and to study the role of microtubules in nuclear positioning and the role of the nucleus in division-plane positioning in fission yeast, *Schizosaccharomyces pombe* [39, 40]. In another study, it was shown that one yeast species could inhibit the growth of another yeast species which was confined by the first yeast [41]. Recently Lanigan *et al.* demonstrated the use of small optically trapped lipid-coated or detergent-coated oil droplets for spatially selective sampling of single cells, allowing membrane proteins from a single cell to be extracted [42, 43]. Optical tweezers are indeed a single cell technique. However, as discussed previously, it is important to perform experiments on a statistically relevant number of cells. A possible solution to increase the throughput when working with optical tweezers was demonstrated in the late 1990's, by the introduction of holographic optical tweezers (HOTs) [44]. With this technique it is possible to trap and manipulate several cells simultaneously, thus allowing several cells to be investigated in parallel.

In this thesis, I will describe how microfluidics, optical tweezers and optical microscopy can be combined in order to acquire data on a single cell level with high spatial (down to the optical diffraction limit) and temporal resolution (down to sub-second time scales). In particular, my work has focused on developing an experimental platform that allows quantitative information regarding the response of single cells to environmental changes to be acquired. The environmental changes are realized using microfluidic devices that are specifically designed for this purpose, while optical tweezers are introduced to allow precise positioning of cells within the devices. The cellular response is mainly monitored through fluorescence imaging of the spatial localization of fluorescent proteins, but also through ordinary transmission images by looking at the cell appearance.

The thesis is organized as follows: The basics of fluorescence microscopy relevant for the study of living single cells is shortly described in chapter 2. In the following chapter, microfluidic devices are introduced together with a description of the physical phenomena occurring on these small scales that are important for controlling the environment within the devices. In chapter 4, the physics behind optical tweezers is explained, and in particular the concepts of holographic optical tweezers are discussed. The experimental system has been verified on three different signalling pathways in *S. cerevisiae*, one dealing with changes in the osmolarity of the extracellular medium, another one dealing with oxidative stress and a third one dealing with glucose starvation. The signalling pathway dealing with osmoregulation, the High Osmolarity Glycerol (HOG) pathway, has been the focus of most of my experiments. The main parts of this pathway are described in chapter 5 together with the model organism *S. cerevisiae*. The complete experimental setup is presented in chapter 6 together with experimental results illustrating the kind of single cell data that can be obtained using this experimental approach. Finally, conclusions and an outlook are presented in chapters 7 and 8 .

Chapter 2

Fluorescence imaging

To study living single cells in detail, a technique to acquire data from which relevant information can be extracted is required. The technique should preferably be fast and sensitive in order to allow intracellular processes, potentially only involving few signalling molecules, to be monitored. In addition, it should be non-invasive and render the cells, which are often small and transparent, visible. Fluorescence microscopy has proved to be an efficient technique for fulfilling these requirements.

The scientific use of the microscope originates back to the work of Antonie van Leeuwenhoek in the 17th century. With his simple microscope, containing a single lens, he was able to study and make drawings of microorganisms, such as bacteria, spermatozoa and red blood cells. However, already in the late 16th century Hans and Zacharias Jansen had developed the first compound microscope. Instead of having a single lens, the compound microscope produces a two-stage magnification by the combination of two lenses, the objective and the ocular. During the 18th century the mechanics of the microscope was improved, and in the 19th century the microscope was perfected optically with the introduction of optics correcting both for chromatic aberrations and spherical aberration. This allowed the resolution to reach the theoretical diffraction limit. This was to a large extent thanks to the work of Ernst Abbe, a German physicist. In 1893, August Köhler reported a method that optimized the illumination conditions of the sample [45].

An optical microscope should in essence fulfil three different conditions. Firstly, it should produce a magnified image of the object. Secondly, it should resolve details in the image, thereby separating neighboring objects. Finally, it should provide high contrast to render details visible against the background. A normal brightfield microscope generally provides quite poor contrast, since most cells are almost transparent and have similar refractive index as the surrounding medium, which is typically water-based. Thus, only the phase of the light passing through the sample is altered, while an amplitude difference is needed to achieve an image with good contrast. However, with fluorescence imaging it is possible to increase the contrast between what is interesting (signal) and what is not (background). The principle idea behind fluorescence imaging is that the objects under study can emit light and thus provide a bright signal against an otherwise black background. Some organic and inorganic substances have the natural property of emitting light when being illuminated. Generally, the emitted light has a longer wavelength than the illuminating light. The Irish physicist George S. Stokes coined this phenomenon “fluorescence”, after having noticed that the mineral fluorite emitted red light when it was illuminated by ultraviolet (UV) light. In order to image a fluorescent object in a microscope, the optical system must thus offer a way of illuminating the sample as well as collecting the emitted light. Today almost all fluorescence microscopes use a scheme of episcopic illumination where the same objective is used both for illuminating and imaging the sample, by collecting the fluorescence light emitted from the sample. Apart from epi-fluorescence microscopy, there are a number of advanced fluorescence imaging techniques suitable for the study of single cells, such as confocal and multiphoton microscopy and the recent super-resolution techniques STED and 4Pi [46].

Parallel to the development of fluorescence imaging techniques is the development of fluorescent molecules that can be used to label specific cellular and subcellular structures. These are usually referred to as fluorescent probes. The development of the green fluorescent protein (GFP) and its spectral variants has been extremely important in order to enable dynamic processes within single living cells to be followed. Fluorescent proteins (FPs) are, as the name implies, proteins that have the ability to fluoresce. The gene coding for the fluorescent protein can be fused onto more or less any gene of interest in the cell strain under study without altering the function of the corresponding protein. Thus, the fluorescent protein marks the location within the cell of the protein that it is fused to, allowing intracellular processes to be followed *in vivo*.

The goal of much of the work presented in this thesis has been to produce images where quantitative information regarding the behavior of single cells subjected to environmental changes can be extracted. To extract and interpret such information correctly, it is necessary to have a good understanding of the technique with which the images are acquired. It is important to understand the image forming process both for optimizing the experimental conditions during image acquisition and to avoid possible pitfalls in the interpretation of the resulting images. The basics behind fluorescence, fluorescent probes, fluorescent proteins and fluorescence microscopy relevant for the experiments performed in this thesis will therefore be described in this chapter.

2.1 Principles of fluorescence

The excitation and emission processes of a molecule or atom are usually described using a Jablonski diagram, see Figure 2.1. Fluorescent molecules are normally found in their ground state (S_0). The ground state for most organic molecules is an electronic singlet in which the spins of the electrons are paired ($+1/2$ and $-1/2$). The molecules can absorb energy from a photon, thus changing its electronic, vibrational and/or rotational state. If the absorbed energy is large enough an electron can move to an orbital of higher energy (S_1 or S_2). The excitation of a molecule by absorption normally occurs without a change in electron spin-pairing, thus the excited state is also a singlet. The transition to this excited state happens on the order of femtoseconds. Following this, the molecule undergoes vibrational relaxation and/or internal conversion so that the electron ends up in the lowest level of the first excited state (S_1). This process occurs on a timescale of picoseconds. From this state, the molecule can go back to the ground state through the emission of a photon, a phenomenon referred to as fluorescence. There are also non-radiative ways of relaxing back to the ground state, not discussed in detail here. The fluorescence lifetime, i.e., the time the molecule spends in the lowest excited state before emitting a photon, is usually on the order of nanoseconds. Due to the band structure of the electronic levels, there is a range of photon energies that can be absorbed, and similarly a range of photon energies that can be emitted. Some energy levels have a higher probability of being populated, and the transitions between energy levels also have different probabilities. These probabilities are reflected in the absorption spectrum and emission spectrum of the molecule. The difference between the wavelengths of highest probability of absorption and emission, respectively, is called the Stokes shift. The main reason for the Stokes shift is the rapid relaxation of excited electrons to the lowest vibrational level of the first excited state, before fluorescence emission occurs. In addition, when fluorescence emission occurs the electron often ends up in one of the higher vibrational energy levels of the ground state. An example of such absorption and emission spectra, for EGFP, is shown in figure 2.2. Generally, the emitted photons have lower energies, i.e., longer

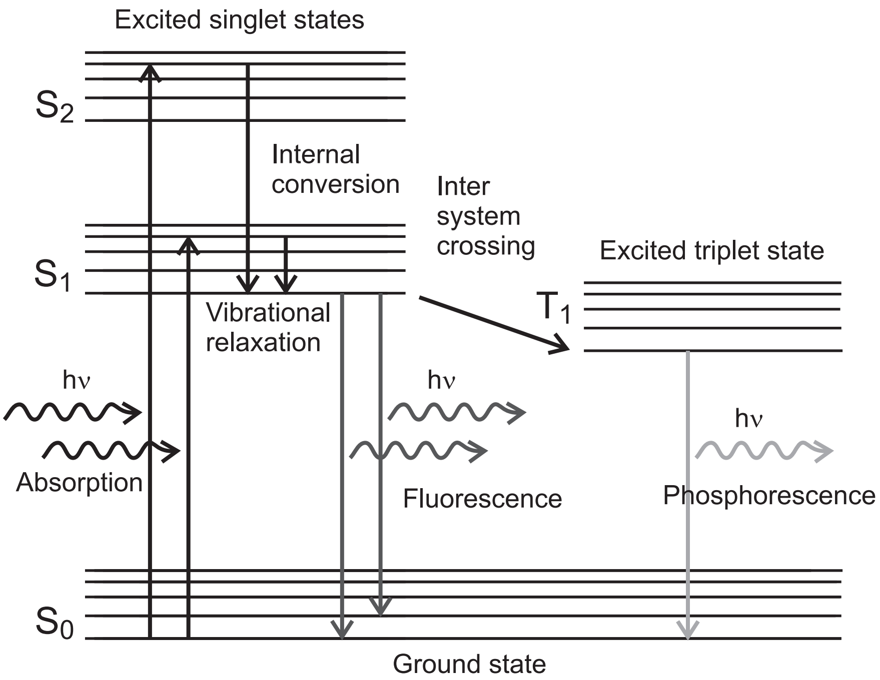

Figure 2.1: A Jablonski diagram can be used to explain the excitation and emission processes of fluorescence. For simplicity only the electronic and vibrational levels are shown. A molecule in the ground state S_0 can absorb an incoming photon and move to an orbital of higher energy (S_1 or S_2). Through vibrational relaxation and/or internal conversion the molecule ends up in the lowest vibrational level of the first excited state. By emission of a photon the molecule can return to the ground state. There is also another less probable alternative, where the excited molecule can undergo a spin reversal and end up in a much more long-lived triplet state (T_1). From this state the molecule can relax non-radiatively or by the emission of a photon, referred to as phosphorescence.

wavelengths, than the exciting photons. However, there is often an overlap between the the two spectra.

The excited electron might also undergo a spin flip such that the spins become parallel, and end up in a triplet state, which is referred to as intersystem crossing. The triplet state vibrational energy levels overlap with the lowest energy level in S_1 in many fluorophores, which enhances intersystem crossing. This kind of transition is forbidden, and relatively unlikely. Nevertheless, it occurs, and from this state the molecule can return to the ground state by spin-reversal and emission of a photon (phosphorescence) or by non-radiative relaxation. The phosphorescence life time is much longer (microseconds) than the fluorescence lifetime. It is also possible for the

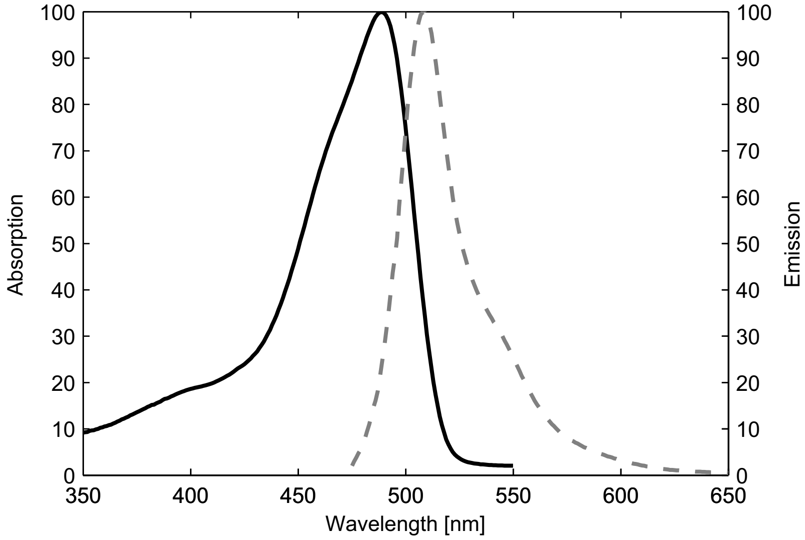

Figure 2.2: Absorption (black solid line) and fluorescence emission (gray dashed line) spectra of enhanced green fluorescent protein (EGFP) in pH 7 buffer. Used with permission from Invitrogen Corp. [47].

molecule to undergo another spin conversion, thus returning to the singlet state, resulting in delayed fluorescence. Yet another option is that the molecule can go to a higher triplet state by absorbing another photon. All these parallel processes compete with the desired process of fluorescence, and result in a smaller number of molecules taking part of the fluorescence absorption-emission cycle. The result is a reduced fluorescence. Even worse is that in the triplet state the molecules are much more chemically reactive, which can result in irreversible bleaching and phototoxicity.

2.1.1 Photobleaching

Incoming photons can also cause chemical damage and irreversible covalent modifications of the molecule, resulting in a permanent loss of the ability to fluoresce. This process is referred to as photobleaching. The average number of excitation and emission cycles that the molecule can undergo before photobleaching occurs is dependent on the molecular structure and the local environment. Good fluorophores are estimated to be able to go through about 10 000 - 40 000 cycles before permanent bleaching occurs [48]. Chemical reactions between the fluorescent molecule and other molecules can occur in the long lived triplet state, leading to photobleaching. One particular kind of photobleaching is photodynamic photobleaching, which

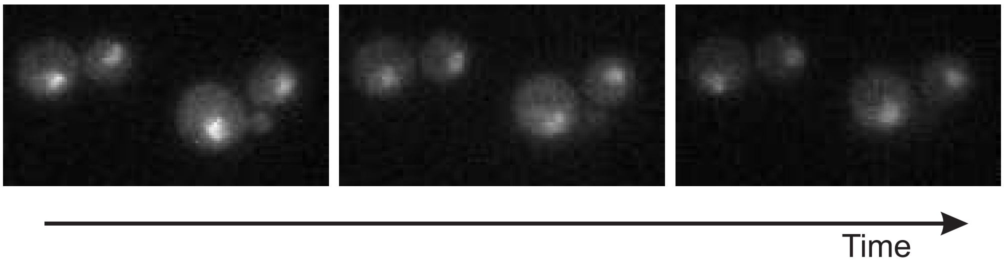

Figure 2.3: Example of photobleaching. Yeast cells expressing Hog1-GFP are bleached over time.

includes the interaction of the fluorophore with light and molecular oxygen. In addition to the bleaching process, free radical singlet oxygen is produced that can chemically modify other molecules in the cell.

For the imaging of living cells, photobleaching is undesired for several reasons: it might result in chemical damage to the cell, the fading signal makes quantitative image measurements more difficult and it sets a limit to the number of useful images that can be acquired, either limiting the time resolution or the total time the sample can be imaged to produce relevant images. An example of unwanted photobleaching of GFP in yeast cells is shown in figure 2.3.

2.1.2 Quenching

Photobleaching is a term that includes all the processes that cause the fluorescence signal to permanently fade over time. Quenching, on the other hand, refers to the reversible processes in which the reduced fluorescence signal can recover over time. Two common forms of quenching are collisional (dynamic) quenching and static quenching. In collisional quenching, the excited molecule can collide with another (non-fluorescent) molecule, resulting in a non-radiative return to the ground state. In most cases neither of the molecules are chemically altered, but the process results in a reduced lifetime of the excited state. Common collisional quenching agents include oxygen, halogens, amines, and many electron-deficient organic molecules. Static quenching occurs when a ground state molecule forms a non-fluorescent complex with another molecule. The number of excitable molecules are thus reduced, resulting in lower fluorescence intensity. In static quenching, fluorescence emission is thus reduced without altering the excited state lifetime.

Quenching can thus be problematic in the quantification of fluorescence events that happen in response to, e.g., a changing environment. An ex-

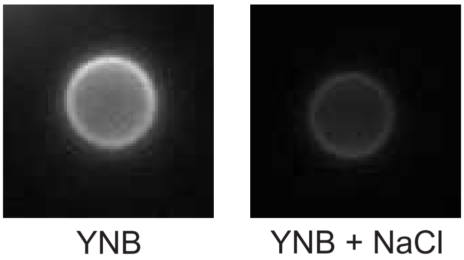

Figure 2.4: Example of quenching. A yeast cell stained with CalcoFluor White. In the left image the yeast cell is in pure nutrition medium (yeast nitrogen base, YNB) and in the right image NaCl is added, which reduces the signal considerably.

ample of a strongly reduced signal as a consequence of an environmental change is illustrated in figure 2.4.

2.2 Fluorescent probes

Some biomolecules are naturally fluorescent (autofluorescent). This can be an advantage if that particular biomolecule is under study, since it removes the need for staining. On the other hand, if the molecules present in the specimen autofluoresce in a spectral region overlapping with the signal of interest, this results in a reduced signal-to-noise ratio. Examples of naturally fluorescent biomolecules are NAD(P)H, tryptophan (and some other aromatic amino acids), porphyrins and flavins [49]. To visualize other non-autofluorescent biomolecules or cellular parts of interest it is necessary to introduce a fluorophore to the sample.

Fluorophores, or fluorochromes, are molecules that are able to fluoresce. When used for biological applications, often conjugated to a larger molecule (such as a nucleic acid, lipid, enzyme, or protein) they are often called fluorescent probes. Most fluorophores have some degree of conjugated double bonds, often in ring structures with π bonds that easily distribute valence electrons over a wide area. Generally, more conjugated bonds in the molecule tend to red-shift the excitation and emission spectra.

Two important parameters for describing the performance of fluorophores are the molar extinction coefficient (ε) and quantum yield (Φ). The molar extinction coefficient reflects the ability of a fluorophore to absorb photons. It is measured in units of $M^{-1}cm^{-1}$ and is measured at the wavelength of maximum absorption. Small organic fluorophores have ε values between 25 000 and 200 000 [48], while EGFP has an ε of about 60 000 at 488 nm, five times higher than wild-type GFP (at 470 nm). The quantum yield, on the other hand, is the fraction of excited molecules that returns to the ground state via fluorescence. Thus, the quantum yield is a number between 0 and 1. Apart from a higher fluorescence intensity (at a given ε), high quantum yield implies that processes competing with fluorescence, such as intersystem crossing, which might lead to bleaching and free radical formation, are less likely. Thus, for many reasons, the closer the quantum yield is to 1 the better. The fluorescent dye *fluorescein* has a quantum yield of about 0.9, while it is about 0.8 for GFP [48]. The measure “brightness” can be used to compare various fluorophores with each other (at least within each spectral class) [16]. It is defined as the product between the extinction coefficient and the quantum yield.

Today several different organic fluorophores with high specificity towards different targets inside the cell, e.g., nucleic acid, ions, lipids, proteins or other biomolecules, are commercially available [47]. Fluorophores can also be conjugated to purified antibodies in order to visualize various parts of cells or tissue, which is referred to as immunolabelling. This usually requires a fixed and permeabilized sample, which is not compatible with live cell imaging. Unfortunately, organic fluorophores can also have a toxic effect on the cell, which can present a problem during time-lapse experiments. The introduction of fluorescent proteins (FPs) offers a flexible tool for the study of intracellular processes *in vivo*.

2.2.1 Fluorescent proteins

The green fluorescent protein was originally found in the jellyfish *Aequorea victoria*. It was also the first fluorescent protein to be cloned [50] and later expressed in *E. coli* and *Caenorhabditis elegans* [51]. This demonstrated that GFP was able to fluoresce without cofactors, thus making it possible to monitor gene expression and protein localization in living organisms. GFP is generally considered non-toxic to cells and not affecting the normal function of the tagged protein in the living cell. The visualization and quantification of fluorescent proteins in the natural environment inside living cells provide the most physiologically relevant information currently available [52].

GFP consists of 238 amino acids forming a β barrel structure with an α-helix running through the axis of the cylinder [50, 53]. The chromophore is localized in the α-helix, close to the center of the cylinder, and is made up of a tri-peptide chain (Ser65-Tyr66-Gly67). With this arrangement the chromophore is sheltered by the barrel structure, making it less sensitive to changes in the cellular environment. The fluorescence of mature GFP is relatively stable towards changes in pH or ionic strength, and it is stable and fluorescent at temperatures up to 65°C [53]. The maturation of the chromophore in GFP only requires oxygen and does not depend on the presence of enzymes or other auxiliary factors.

The excitation spectrum of wild-type GFP has a peak at 395 nm and a smaller one around 470 nm, while the emission spectrum has a maximum at 505 nm and a shoulder around 540 nm [51]. Mutations in the chromophore allows engineering of fluorescent proteins in other parts of the visible spectrum. To a high degree this has become possible through the work of one of the 2008 Nobel prize laureates in chemistry, Roger Tsien, who made large contributions to the understanding of the fluorescent properties of GFP and its spectral variants. This work has led to the development of brighter and more photostable proteins, such as the enhanced GFP (EGFP), with improved folding properties and more rapid maturation of the chromophores. Fluorescent proteins with emission in the blue to yellow range have been developed through modifications of the GFP. However, proteins that fluoresce at red or far-red wavelengths are of specific interest, since eukaryotic cells and tissues display reduced autofluorescence at those wavelengths [17]. They also allow multi-color imaging using the full visible spectrum. In addition, photodamage tends to decrease with increasing wavelengths [52].

The orange and red fluorescent proteins that exist today are not derived from the jellyfish, but instead from different coral species. However, those wild-type proteins are tetrameric. Oligomerization of fluorescent proteins should in general be avoided in order for the protein not to interfere with the host protein to which it is fused [17]. The first true monomer red fluorescent protein was derived from *Discosoma sp*, and today there are a number of monomeric orange and red fluorescent proteins commercially available (the “mFruits”), where mCherry seems to be the best choice regarding photostability in the red part of the spectrum. Excellent reviews comparing various fluorescent proteins within each spectral class and giving recommendations have been written by Shaner *et al.* [16, 54].

Fluorescent proteins can be cloned on episomal vectors or introduced by recombination into the genome of the target organism using PCR-based approaches. In this way it is possible to fuse the fluorescent protein to almost any protein of interest of the target organism. It is important to assess that the expressed fluorescent protein does not interfere with the normal cellular function of the protein to which it is fused. Integrating the fluorescent protein into the genome allow the protein levels to remain at normal levels, but as a consequence the fluorescence signal might be low. On the other hand, introducing the tagged protein on a plasmid leads to various degrees of over-expression and consequently better signal-to-noise ratio. In this case, care should be taken not to make false conclusions [52]. There are reports suggesting that chromosomal integration results in a more homogenous signal distribution in the cell population compared to over-expressed fusions, which shows a larger heterogeneity [55]. For time-lapse studies where quantitative measurements of protein levels are to be made, it is important to consider the maturation time of the fluorescent protein. For some fluorescent proteins, like the mCherry, it is as short as 15 minutes [56].

2.3 Fluorescence microscopy

Today there are a number of fluorescence imaging techniques available. The most basic and widely used technique is epi-fluorescence microscopy. In this configuration the microscope objective not only serves to image the specimen, i.e., to collect the emitted fluorescence light, but also to act as a condenser, illuminating the sample with the excitation light (so called episcopic illumination). This setup makes it easier to detect the weak emission light compared to in a transmission fluorescence microscope (diascopic illumination). The excitation is equally effective in both transmission and epi-fluorescence mode, while there is a much smaller proportion of the excitation light reflected off the sample in the epi-configuration compared to the transmitted excitation light in transmission mode. This excitation light needs to be blocked by filters before reaching the detector or camera. In this context it is also worth mentioning that the emission light radiates spherically in all directions [57].

The light source in epi-fluorescence microscopes is usually a broad band mercury or xenon lamp. The lamp house also incorporates a heat filter, suppressing infrared wavelengths that would otherwise heat the sample. The light path usually also contains a set of neutral density filters in order to attenuate the illuminating light intensity. The separation of the excitation and emission light is performed through the use of a filter set containing a dichroic mirror and excitation and emission filters. These are normally mounted in a filter cube, see figure 2.5. A modern microscope has room for several different filter cubes, which can be used in multi-color imaging. The dichroic mirror is a thin piece of coated glass mounted at a 45° angle with respect to the optical path of the microscope. It is designed to reflect the excitation wavelengths, while transmitting the emitted fluorescence wavelengths from the sample. The cut-off between reflection and transmission is designed to lie between the excitation and emission peaks of the fluorophore. The excitation filter serves to filter out only the wavelengths

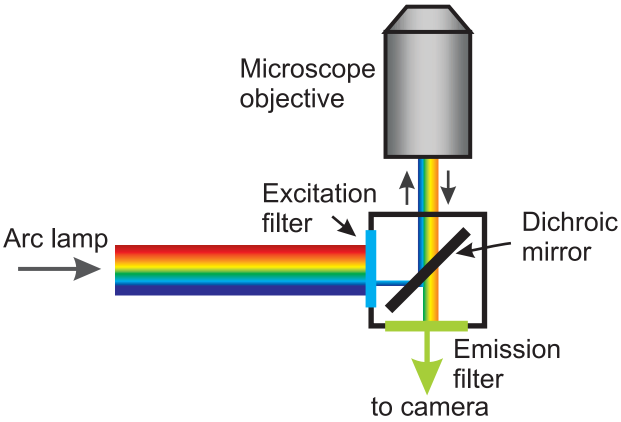

Figure 2.5: The principle of a filter cube used for separating excitation and emission light. The broad band light from the lamp goes through an excitation filter in order to only select the wavelengths needed for efficient excitation of the fluorophore. The dichroic mirror is mounted at 45°, reflecting the excitation wavelengths while transmitting the longer emitted wavelengths. An additional emission filter is used to block out any remaining excitation light before reaching the detector or camera.

needed for the excitation of the fluorophore, while the emission filter (or barrier filter) similarly filters out the emission light and strongly attenuates scattered excitation light, since the dichroic mirror is generally not blocking all of the reflected excitation light. The strong attenuation of the scattered excitation light is necessary to obtain a good signal-to-noise ratio, since the excitation light is typically 10^5 to 10^6 times brighter than the emitted light [57]. The range of wavelengths transmitted through these filters are dependent on which and how many fluorophores that are imaged. When a single fluorophore is imaged, it is advantageous to use the excitation and emission bands as efficiently as possible, while minimizing the overlap of the transmission curve of the emission filter with the excitation spectrum, in order to obtain a strong signal. However, in multi-labelling experiment where several filter sets are used, it is sometimes necessary to use narrower excitation and emission filter bandwidths to avoid “crosstalk”, i.e., to make sure that only one fluorophore is detected with each filter set. An example of how the transmission characteristics of a filter set can look can be seen in figure 2.6.

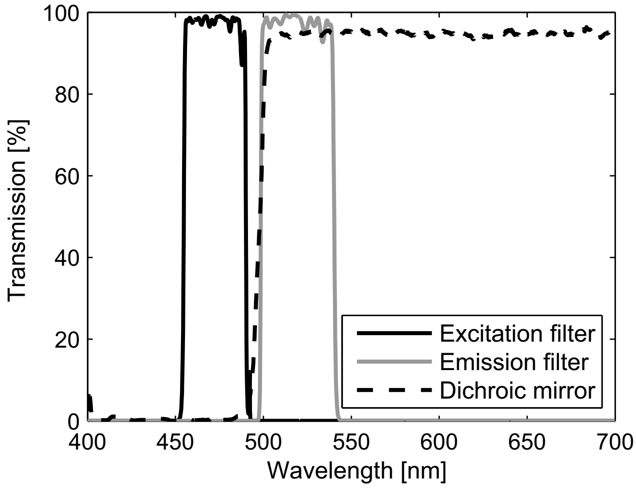

Figure 2.6: Example of spectra for the excitation filter (solid black), emission filter (solid gray) and dichroic mirror (dashed black). Data for Semrock GFP filter cube 3035B. Used with permission from Semrock, IDEX Corporation [58].

2.3.1 The microscope objective

A central component of an optical microscope is the objective. The microscope objective consists of several lenses put together in order to project a magnified image of the specimen. There are a number of optical parameters and characteristics that are important to know when working with microscopy in order to choose the best objective for a given application. Some of the most important are the magnification, the numerical aperture and the degree of aberration correction.

Modern objectives are infinity corrected, meaning that the objects are positioned in the front focal plane of the objective and that the image is formed at infinity. A so called tube lens is thus needed to form an image at a finite distance, see figure 2.7. The tube lens forms this, so called, intermediate image at a focal length distance from the tube lens, with a magnification according to the inscription on the objective, e.g., 20×, 40× or 100×. Thus, using a 100× microscope objective and a 20 cm tube lens, the effective focal length of the objective will be 2.0 mm. It might seem that a large magnification is always better, but it is important to remember that the image will then be distributed over a larger area. The image intensity will thus be inversely proportional to the magnification squared. In situations where the fluorescent signal from the sample is low it might

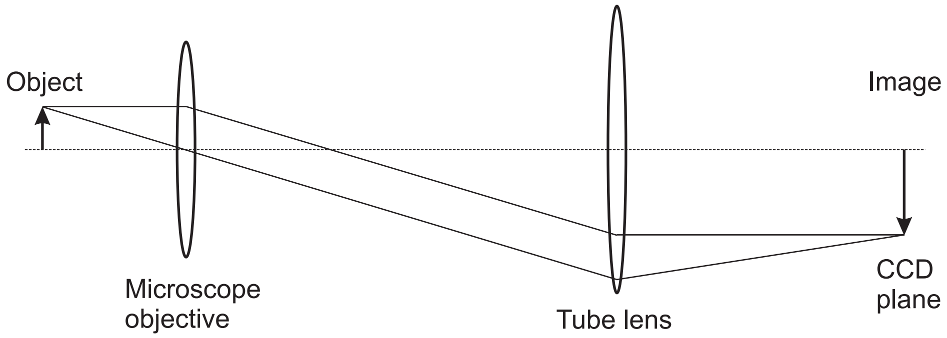

Figure 2.7: Image formation in an optical microscope using an infinity corrected microscope objective. The microscope objective projects an image of the object at infinity. A tube lens is used to move the image to a finite distance. The CCD camera used for imaging can be positioned in this image plane or in a conjugate plane to the image plane.

therefore be appropriate to consider a lower magnification objective with a high numerical aperture.

The numerical aperture (NA) of the objective is defined as

$$NA = n \sin \theta_{max}, \tag{2.1}$$

where n is the refractive index of the medium between the front lens of the objective and the specimen, and θ_{max} is the half angular aperture of the objective. The NA is strongly related to the resolution limit of an optical microscope, which is limited by the diffraction of light. The Rayleigh criterion describes the ability to separate two equally bright neighboring point sources. The point sources can be resolved if they are separated by a distance larger than

$$d = \frac{1.22\lambda}{2NA} \tag{2.2}$$

for a circular aperture. Thus, the NA governs the achievable resolution in the final image, and to achieve a high resolution a high NA objective or a short wavelength, λ, is desired. The NA also affects the depth of field. As long as air is the medium between the objective and the coverslip it is in theory not possible with a NA larger than 1, and in practice not larger than 0.95, corresponding to a maximum acceptance angle of the light cone of 72° [59]. To increase the NA above 1 it is necessary to introduce an immersion medium between the objective lens and the coverslip. The objectives with the highest NA use oil as immersion medium. The oil has a refractive index of about 1.5, which is matched to the refractive index of the coverslip in order to avoid introducing spherical aberrations and minimizing reflections. With oil immersion objectives it is possible to obtain NAs above 1.4, providing the best resolution. When oil immersion objectives are used in fluorescence microscopy it is important to choose an immersion oil that has low autofluorescence at the excitation wavelength.

The NA is also important in order to collect the fluorescence light efficiently, as well as illuminating the sample efficiently, since a larger NA implies a larger half angle of the cone of light that can be collected or produced. The amount of excitation light that can be used to excite the specimen is roughly proportional to $(NA)^2$, while the amount of fluorescence emission collected is also proportional to $(NA)^2$. The fluorescence intensity that reaches the detector is thus proportional to $(NA)^4$. A microscope objective suitable for fluorescence imaging should also have low autofluorescence of its lens elements and a high transmission for UV, visible and near infrared light.

Microscope objectives can generally be divided into different categories, depending on the degree of aberration correction [59]. The simplest ones are the achromatic objectives, which are corrected for spherical aberrations for green colours and corrected for chromatic aberrations for two colors (bringing red and blue light to a common focus). Objectives of the next degree of correction are referred to as fluorites or semi-apochromats. They are corrected spherically also for blue colors, and chromatically for red and blue, where the foci are usually also closer to the focus of the green light. The best degree of correction is achieved with the apochromatic objectives. They are corrected chromatically for four colors: deep blue, blue, green and red, and spherically corrected for two or three colors: deep blue, blue and green. The apochromats generally have higher NA than fluorites or achromats for a given magnification. Without extra measures, the projected image would be curved rather than flat. Objectives that are designed to produce flat images across the field of view are referred to as plan-achromats, plan-fluorites or plan-apochromats. For the imaging of weak fluorescent signals it is important to know that objectives with a higher degree of correction generally contains more lens elements, which reduces the light transmission of the objective.

2.3.2 The camera

The most common type of camera used for epi-fluorescence imaging is a CCD (charged coupled device), a pixelated device able to detect low light intensities. For multi-color imaging a color camera can be used in combination with a filter set with multiple excitation and emission bands. However, for applications where weakly fluorescent samples are imaged, a monochrome camera is preferred. Here, color imaging is achieved through sequential imaging using different filter cubes, where each filter set is optimized to collect as much fluorescence light as possible without crosstalk. The images taken with the different filter sets can then be combined, using color tables, into a single color image. When imaging weak fluorescent samples it is important to keep in mind that the fluorescence intensity scales inversely with the square of the size of the image (c.f. the previous discussion regarding the magnification of the microscope objective). Large pixels are therefore able to detect more photons per pixel, while the resolution is decreased. For a given pixel size, one way of increasing the sensitivity is by binning the pixels together, at the cost of lower resolution. Optimization of the pixel size is also important for high-resolution applications. Here, the Nyquist criterion states that we should sample the image with at least twice the highest spatial frequency that we wish to resolve, thus setting an upper limit to the pixel size.

For applications where the speed of the image acquisition is an important parameter, it is preferable to only read out a part of the image from the camera chip, a so called region of interest (ROI). When quantitative measurements of the microscope images are made it is also important that the camera response is linear with intensity, such that a detected signal of double magnitude actually corresponds to the double amount of fluorescence, or that the relation between fluorescence intensity and camera response is known. When choosing a CCD camera the spectral response characteristics of the CCD should also be considered for optimum performance. For applications where the signal is extremely low or where it is important to reduce photobleaching and phototoxicity, a good choice might be an electron multiplying CCD (EMCCD). These cameras have an on-chip multiplication gain that enables detection of very low light levels, while keeping the read-out noise low.

Chapter 3

Microfluidics

Microfluidics deals with miniaturized fluid handling devices - networks of small channels where at least one dimension typically is in the range of $10 - 500$ μm. These kind of devices are also often referred to as lab-on-a-chip (LOC) devices or micro total analysis systems (μTAS), which emphasizes the unique possibilities to accomplish laboratory tasks and analysis in a miniaturized format. Microfluidic devices have been shown to be suitable for a variety of applications, in particular within biochemistry and biology. Potential applications for microfluidics in biochemistry includes miniaturized analytical systems for DNA sequencing, polymerase chain reaction (PCR), electrophoresis, DNA separation, enzymatic assays and immunoassays [60]. Microfluidic systems have also shown to be of interest for applications in cell biology, such as cell counting, cell sorting, cell culture, flow cytometry-like techniques, the exposure of cells to chemical gradients, and for the analysis of single cells, by controlling the cellular microenvironment [24, 61–63]. The possibility to control the microenvironment temporally and spatially, opens up for new exciting experiments in, e.g., cell biology.

Initially microfluidic devices were fabricated using technology from the the microelectronics industry, but today there are techniques specifically developed for the production of microfluidic systems, which has become a research field on its own. A popular technique for fabricating microfluidic devices is soft lithography, where different structures are molded in an elastomer from a lithographic master. Poly(dimethylsiloxane), PDMS, is a silicone elastomer that is commonly used for this purpose. Microfluidic systems fabricated in PDMS have the advantage of being transparent, thus they are easily combined with optical microscopy.

Miniaturization of devices offers a number of more or less obvious advantages, such as requiring small volumes of solvent, sample (e.g., cells), and reagents, portability, low power consumption, versatility in design, potential for parallel operation and for integration with other miniaturized devices [60]. However, shrinking macroscale devices might be counterproductive. On the microscale other physical phenomena than we are used to from our everyday experience dominate. Here viscous forces dominate over inertial forces, flows are purely laminar (i.e., turbulence is non-existent), surface tension can be a considerable force, diffusion is the basic mechanism for mixing, evaporation is an issue on open liquid surfaces, and the devices usually have extremely high surface area to volume ratios. By integrating knowledge of these effects in the design of microfluidic devices it is possible to perform experiments not possible on the macroscale.

There are essentially two main methods for establishing a flow in microscale devices: electro-osmosis and pressure-driven flow [64]. Electro-osmotic flow has the advantage that it provides a blunt flow velocity profile, but unfortunately requires high voltages and is sensitive to variations in fluid composition and channel wall coatings. Pressure-driven flow is much less sensitive to such variations but is characterized by a parabolic velocity profile, leading to hydrodynamic dispersion effects. The pumping method of choice is therefore dependent on the application.

In my work only pressure-driven flow has been used. Consequently, this chapter will focus on issues related to this kind of flow. As described above, microfluidics can be used for a variety of tasks, utilizing different aspects of the physics of the microscale. In my work I have used microfluidics as a tool for accomplishing environmental changes of single cells, by establishing a concentration gradient in a microfluidic device. Thus, the focus of this chapter will be on explaining various phenomena relevant for this specific application of microfluidics.

3.1 Fabrication of microfluidic devices

Common approaches for fabricating microfluidic devices, in particular for biological applications, are the techniques of soft lithography [60, 65, 66]. The main fabrication steps are outlined in figure 3.1 and will be described in more detail below.

The fabrication process starts with the design of the channel system in a CAD program. This design is transferred to a photomask that is transparent where the channels are supposed to be and opaque elsewhere (if a negative photoresist is being used to produce the master, see below). This photomask can either be a high-resolution chromium mask fabricated

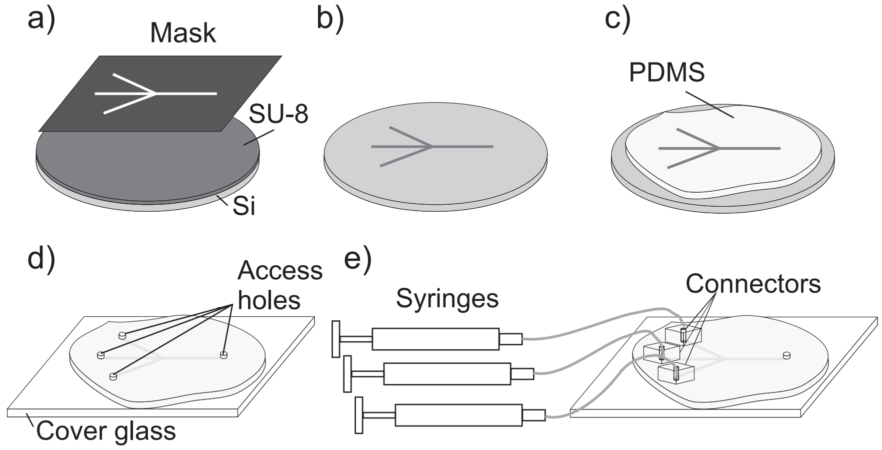

Figure 3.1: Fabrication of a microfluidic device using soft lithography. A silicon wafer is spincoated with a photoresist, SU-8. The resist is exposed through a mask containing the desired channel design (a). The wafer is baked and developed, to form a master where small ridges of photoresist corresponds to the channel pattern (b). PDMS is poured onto the master and heat cured to form a negative replica of the channel pattern (c). In the next step the PDMS is peeled off the wafer, inlet and outlet holes are made, and the PDMS slab is bonded to a coverslip (d). Connectors, also fabricated in PDMS, are attached and the final device is connected via teflon tubing to syringes with liquid media (e). Flows in the microfluidic device can then be established with, e.g., a syringe pump.

with, e.g., e-beam lithography, or, for applications not requiring as high resolution, a transparency printed with a high-resolution printer.

The pattern of the photomask is transferred to the master through contact photolithography. First a photoresist, i.e., a light sensitive polymer, is spin-coated on a silicon wafer to a thickness that will yield the desired height of the final microfluidic channel. A commonly used photoresist for soft lithography is SU-8, which is an epoxy-based negative photoresist, where the term negative means that the exposed parts of the resist will remain after development. SU-8 can provide high aspect ratio structures even in thick films, thus making it possible to make nearly vertical walls even when the height of the microfluidic system is relatively large. This photoresist layer is then subjected to a so called pre-bake (or soft-bake) on a hot plate, where solvents are evaporated and the film is densified. Following the soft bake the resist-coated wafer is put in contact with the photomask and exposed to collimated near UV light (the i-line of mercury arc lamps at $\lambda = 365$ nm is recommended). SU-8 is cross-linked in two steps: during the UV exposure small amounts of a strong acid is generated, which initiate the thermally driven cross-linking during another baking step, referred to as the post exposure bake. The photoresist must then be developed, preferably under shaking, in order to remove all unexposed parts. After development the master is rinsed with isopropyl alcohol and gently blow dried with nitrogen. An additional hard bake can be performed to further cross-link the SU-8 structure. The final master thus consists of a two-dimensional network of photoresist ridges defining the desired channel pattern.

The master can now be used for making negative replicas of the channel pattern in the PDMS material. PDMS consists of repeating -OSi(CH_3)$_2$- units and is often supplied as a two-part kit consisting of a base and a curing agent. These parts are typically mixed in a 10:1 weight ratio, degassed and poured over the master. The PDMS is then cured for approximately one hour in 95°C in an oven. The cast PDMS is peeled of the master, which is ready to be used again in order to produce another PDMS replica. The piece of PDMS containing the channel pattern is bonded to a coverslip to form a closed channel, where three walls are made of PDMS and the bottom is made of glass. Sealing the PDMS onto a coverslip by putting the two surfaces in contact will form a reversible bond which might, however, be too weak to withstand the pressures from the fluid pumping. Reversible sealing occurs because PDMS is flexible and can conform to flat surfaces, via van der Waals forces. To form an irreversible bond that can withstand higher pressures, both the cast PDMS and the coverslip are exposed to an air plasma, creating polar groups (Si-OH) on the surface that condense with appropriate groups on the other surface to form a covalent bond (-Si-O-Si-) when put in contact. The polar groups formed under plasma treatment also make the walls hydrophilic, facilitating the filling of channels with liquids and reducing the problem of air bubbles being trapped in the system. The use of a coverslip to seal the microfluidic device is convenient, since it enables direct optical access to the channel volume. Thus microfluidic devices can preferably be combined with both high resolution imaging and optical tweezers (both requiring high NA microscope objectives).

There are numerous ways of interfacing the microfluidic device with external pumps in order to establish a flow. The devices can either be made thick (a few millimeters) in the casting process, with holes for connecting tubing being either drilled afterwards or molded together with the channel. If the channels are made thinner (~ 1 mm) there is a need for a connector. Simple connectors can be fabricated as small cubes in PDMS with holes for the tubing, that are subsequently attached to the PDMS channel with plasma treatment. Before they are attached, holes in the thin PDMS device must be punched or drilled. Photos of microfluidic devices made with these two different approaches for connecting the system to a fluid pump can

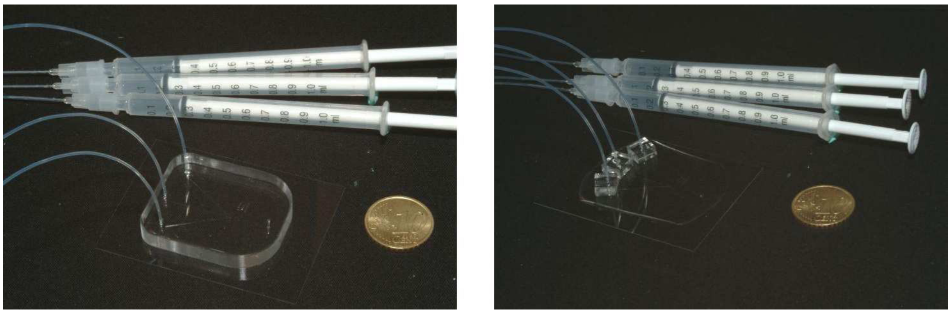

Figure 3.2: Photos of microfluidic devices attached to syringes. For comparison of the size, a 1 cent euro coin is shown next to the microfluidic devices. Left: 4 mm thick PDMS device with holes through the PDMS for connecting tubing, right: 1 mm thin PDMS device with PDMS cubes as connectors.

be seen in figure 3.2. Both are connected via teflon tubing to syringes containing the media to be pumped in the channels.

PDMS has a number of properties that are useful for biological applications [65]. In addition to the possibilities of replicating micron-sized features and the bonding properties, it is inexpensive compared to traditionally microfabricated structures in silicon and glass. PDMS is also transparent in the visible range down to 280 nm, thus being easily combined with fluorescence imaging. It is also nontoxic to cells, impermeable to water but permeable to gases - allowing cells to be cultured within the devices. Finally the surface chemistry can be modified.

3.2 Pressure driven laminar flow

In pressure driven flow the volumetric flow rate, Q, is given by $Q = \Delta P/R$, where ΔP is the pressure drop along the channel and R is the fluidic resistance of the channel. The pressure drop can be established either by applying vacuum at the outlet and having the inlet open, or by applying positive pressure at the inlet, e.g., with a syringe pump. An advantage of using a syringe pump for driving the flow is that the system becomes less sensitive to defects in the micro-fabricated channel. Partially occluded channels, e.g., by a small dust particle or trapped clusters of cells, increases the fluidic resistance and therefore affects the flow rate at a given pressure. With a syringe pump, however, the same volume is always forced through the obstruction.

The fluidic resistance of a rectangular microfluidic channel of width w, height h, length L and with a pumping medium of viscosity η is given by

$$R = \frac{12\eta L}{wh^3}\left[1 - \frac{h}{w}\left(\frac{192}{\pi^5}\sum_{n=1,3,5}^{\infty}\frac{1}{n^5}\tanh\left(\frac{n\pi w}{2h}\right)\right)\right]^{-1}, \tag{3.1}$$

or

$$R = \frac{12\eta L}{wh^3} \tag{3.2}$$

for channels with a high aspect ratio ($h \ll w$) [67]. Thus, for long channels with a small cross section a large pressure drop is required to establish a certain volumetric flow rate. For example, in a 50 μm wide and 25 μm high channel that is 1 cm long, a pressure drop of 290 Pa is required to create a water flow of 75 nl/min (corresponding to an average flow velocity of 1.0 mm/s). The fluidic resistance is an important parameter in the design of microfluidic systems. Splitting a 25 μm high channel into two equally long channels, 25 μm and 50 μm wide, respectively, one might intuitively think that two thirds of the flow would go into the wide channel and one third into the narrower one, which would be the case for high aspect ratio systems. However, from equation 3.1, it turns out that the narrow channel has a fluidic resistance that is more than 3 times larger than the other channel, resulting in more than 2/3 of the flow going through the wide channel.

The basic equation describing pressure driven fluid flow in microfluidic devices is the Navier-Stokes equation

$$\rho\left(\frac{\partial \mathbf{u}}{\partial t} + \mathbf{u}\cdot\nabla\mathbf{u}\right) = -\nabla p + \eta\nabla^2\mathbf{u} + \mathbf{f}, \tag{3.3}$$

where ρ is the density of the fluid, η is the viscosity, $\mathbf{u}$ is the velocity (with components in the x, y and z directions), p is the pressure and $\mathbf{f}$ represents body force densities (such as gravity, ρg). This equation is essentially Newton's law for a fluid, with the inertial acceleration terms on the left hand side describing the rate of change of momentum (per unit volume) of a fluid particle moving with the flow. $\rho\partial\mathbf{u}/\partial t$ describes the momentum change per unit volume due to variations in the velocity field over time while $\rho\mathbf{u}\cdot\nabla\mathbf{u}$ describes the momentum change induced by spatial variations in the velocity field. On the right side are the forces per unit volume acting on the fluid particle, where viscous forces are represented by the term $\eta\nabla^2\mathbf{u}$ and pressure forces by $-\nabla p$. The term "body force" comes from the fact that the force acts on the volume of a fluid particle rather than over its surface, as stresses between fluid particles do. The Navier-Stokes equation in combination with mass conservation

$$\frac{\partial \rho}{\partial t} + \nabla \cdot (\rho \mathbf{u}) = 0, \tag{3.4}$$

constitutes a set of partial differential equations that can be used to describe the flow in a microfluidic system. The density can usually be treated as a constant (in time and space), reducing 3.4 to $\nabla \cdot \mathbf{u} = 0$. When using these equations it is assumed that the fluid is incompressible, i.e., pressure differences are not producing any significant density changes. We also only consider Newtonian liquids, i.e., the viscosity is independent of the velocity.

For flows where the viscous forces are dominating over inertial forces the left side of the Navier-Stokes equation can be neglected, leaving Stokes equation

$$\eta \nabla^2 \mathbf{u} = \nabla p, \tag{3.5}$$

if also neglecting body forces. This equation contains no time derivatives, meaning that all motion is symmetric in time [68]. The flow pattern will therefore be completely reversed if the pressure and forces exerted on the fluid changes sign. Thus, the flow from right to left past an obstacle is the exact reverse of that from left to right. Another characteristic of this kind of flow is that viscous interactions extend over large distances. Thus an obstacle affects the flow profile over large distances, compared to the size of the obstacle.

Solving equation 3.5 for an infinitely long rectangular channel with a constant pressure gradient driving the flow (i.e., $\partial p/\partial x = -G$, with $G > 0$), and using the no-slip boundary condition, i.e., the fluid velocity is zero at the walls, we arrive at the following expression for the flow [69]

$$\begin{aligned} u(y,z) \;=\; & \left(\frac{Gh^2}{8\eta}\right) \frac{32}{\pi^2} \sum_{n=0}^{\infty} \frac{(-1)^n}{(2n+1)^3} \cdot \left[1 - \frac{\cosh\left[(2n+1)\pi y/h\right]}{\cosh\left[(2n+1)\pi w/2h\right]}\right] \\ & \cdot \cos\left[(2n+1)\pi z/h\right]. \end{aligned} \tag{3.6}$$

This expression is plotted in figure 3.3 for different aspect ratios. Figure 3.3 a) shows the resulting flow profiles in the width direction (y) in the center of the channel (i.e., at half the channel height, $z = 0$), while figure 3.3 b) shows the flow profiles in the height direction (z), also in the center of the channel (at half the width, corresponding to $y = 0$). From these graphs it can be concluded that for channels with a square cross section, the flow profiles are close to parabolic in both directions, while for higher aspect ratios, the flow profile is parabolic-like only in the shorter dimension, and more plug-flow like in the longer one.

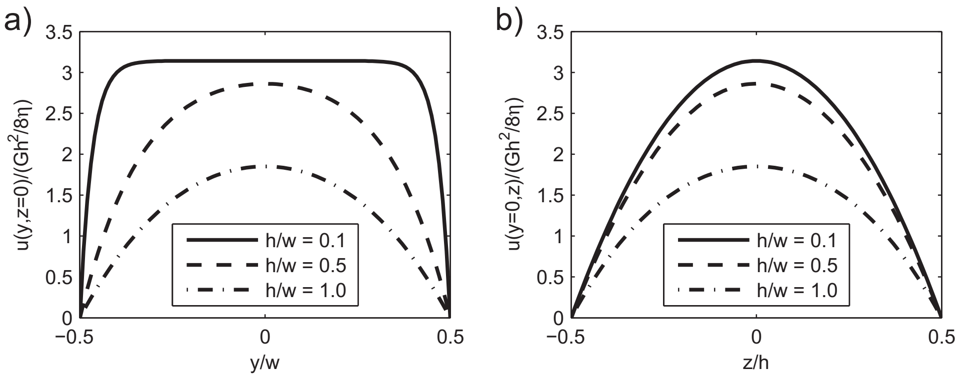

Figure 3.3: Flow profiles for various aspect ratios (h/w): a) at half the channel height, h, and b) at half the channel width, w.

The non-uniform flow-profile, mainly in the shorter dimension, introduces shear on cells positioned within a microfluidic device. Shear stress is experienced by any object when a tangential force is applied to its surface. The shear stress (τ) is given by

$$\tau = -\eta \frac{\partial u}{\partial x}, \tag{3.7}$$

in one dimension, where η is the fluid viscosity, u is the fluid velocity and x is the spatial coordinate. Comparing two microfluidic systems with the same maximum velocity in the center, an object on the bottom of a small channel will experience a larger shear stress than in a larger channel due to the steeper velocity gradient. The maximum amount of shear that a cell can tolerate will depend on the cell line, as summarized by Walker *et al.* [70].

3.2.1 Reynolds number

In fluid dynamics there are numerous dimensionless parameters that define various regimes of fluid behavior. One of the most well known parameters is the Reynolds number

$$\mathrm{Re} = \frac{\rho U L}{\eta}, \tag{3.8}$$

where ρ and η are the density and viscosity of the fluid, respectively, and U and L are the typical velocity and length scales of the device. Flows are generally considered laminar for $\mathrm{Re} < 2300$. Above this number there are signs of turbulence, and at high Re the flow is turbulent [67]. For a channel with a circular cross section, the diameter is usually chosen as the typical length scale. For a channel with a rectangular cross section, the typical length scale can be estimated by the hydraulic diameter, defined as $D_h = 4A/P$, where A is the cross-sectional area and P the wetted perimeter. For the previous example with a 50 μm × 25 μm channel with an average flow of $U = 1$ mm/s and water as the pumping liquid, the Reynolds number is approximately 0.03, thus orders of magnitude below the transition from laminar to turbulent flow. In microfluidics the Reynolds number is generally found to be below 1, i.e in the region of pure laminar flow.

The Reynolds number also describes the relative importance of inertial and viscous forces. Viscous forces dominates at low Re while inertial forces dominates at high Re. Consider a channel with a fluid flow with speed U that makes a 90° turn. During the turn, a fluid element experiences a centrifugal force density proportional to $\rho U^2/L$. Gradients in viscous stress give rise to viscous force densities, and scales as $\eta U/L^2$. The ratio of inertial force densities to viscous force densities thus equals the Reynolds number. Alternatively, the Navier-Stokes equation can be rewritten in dimensionless form, i.e., each variable is normalized to its typical value, resulting in terms of order unity. In the dimensionless equation the inertial term is exactly Re times larger than the viscous term.

3.3 Diffusion

Due to the well defined flow pattern in laminar flows, the only mechanism for two parallel flows to mix is by molecular diffusion, i.e., Brownian motion, characterized by a diffusion coefficient, D. The diffusion coefficient is inversely proportional to the size of the diffusing particle or molecule

$$D = \frac{k_B T}{6\pi\eta a}, \tag{3.9}$$

where k_B is Boltzmann's constant, T is the absolute temperature, η is the viscosity of the medium, and a is the radius of the particle. The denominator is often referred to as the Stokes drag coefficient. The distance a molecule diffuses in time t can be estimated from $x = \sqrt{2Dt}$. Thus, diffusion becomes the dominant transport mechanism only at long time scales and/or short distances. For example, it takes around 3 h for a small protein to diffuse 1 mm in water, but only 1 s to diffuse 10 μm [69]. This has implications when culturing cells in a microenvironment. In a macroscale culture system, convection through, e.g., stirring is the main mode of transportation, making sure that cells are supplied with necessary metabolites. In the microscale, where diffusion dominates, the distributions of metabolites and waste products are less homogenous. This can be an advantage, since molecules secreted from the cell does not travel very far and the cell can maintain its secreted microenvironment more easily, opening up for new types of experiments [70].

Diffusion of particles from a region of higher concentration to a region of lower concentration is generally described by Fick's first law of diffusion

$$\mathbf{J} = -D\nabla c, \tag{3.10}$$

where $\mathbf{J}$ is the flux of particles and c is the concentration. By combining Fick's law with the continuity equation and including the convective term we arrive at the following equation describing convection and diffusion

$$\frac{\partial c}{\partial t} = -\nabla \cdot \left(-D\nabla c + c\mathbf{u}\right). \tag{3.11}$$

Here we have neglected any reaction terms, which would add to the right side of the equation. It should be noted that the viscosity of a solution (and hence the diffusion coefficient) is often concentration dependent.

3.3.1 Péclet number

In a similar way as the Reynolds number describes the relative importance of inertial to viscous forces, the Péclet number describes the relative importance of convection to diffusion,

$$\mathrm{Pe} = \frac{UL}{D}. \tag{3.12}$$

This term appears in the dimensionless version of equation 3.11, where the convective term is Pe times larger than the diffusive term. For large Péclet numbers the flow is the dominating transport mechanism, while at low Péclet numbers, i.e., slower velocities or shorter distances, diffusion dominates. In other words, stirring is a useful strategy for mixing only if $\mathrm{Pe} > 1$ [68]; the time for transport by stirring is L/U, while the time for transport by diffusion is proportional to L^2/D. Thus, stirring is preferred for mixing if the time for transport by diffusion is larger than the time for transport by stirring, i.e., $L^2/D > L/U$; or rearranged $\mathrm{Pe} = LU/D > 1$.

In microfluidic applications there is no typical range of values of the Péclet number, as for the Reynolds number. The value is depending on the desired function of the microfluidic device, e.g., mixing, separation *etc.* The Péclet number can be interpreted as the number of channel widths needed for complete mixing after merging two flows in a T junction [71]. The time needed for the molecules to diffuse one channel width is proportional to $\tau_D \sim w^2/D$. During this time the molecules have travelled a distance $x \sim U\tau_D = Uw^2/D$ due to the flow. Thus, the number of channel widths required for complete mixing is of the order $x/w = Uw/D$, or the Péclet number if $L \sim w$. As an example, consider two 50 μm wide channels merging into a 100 μm wide channel, with a flow speed of 100 μm/s, where the fluid is water and one of the inlet channels in addition is containing sorbitol ($D = 0.67 \cdot 10^-5$ cm^2/s). It then takes about 15 channel widths for complete mixing of the two fluids to occur.

3.4 The T mixer & simulations

Much of the experimental work presented in chapters 6.2-6.3 is based upon the principles of a microfluidic device often referred to as the T mixer or T sensor. This device has two channels that merge into one, in the form of a T or Y. Due to the laminar flow, the two flows will only mix because of diffusion, forming a concentration gradient in the mixing zone. This simple geometry forms the basis for several separation or mixing designs [72].

A simple estimate of the mixing of two different media in a T mixer can be obtained by considering the spreading in one dimension of a concentration profile that is initially described by a Heaviside step function, in which the concentration is $c = 0$ for $y \leq 0$ and c_0 for $y \geq 0$. The substance has a diffusion coefficient D. The concentration profile is given by

$$c(y,t) = \frac{1}{2}c_0\left[1 - erf\left(-\frac{y}{2\sqrt{Dt}}\right)\right], \tag{3.13}$$

where $c(y,t)$ is the concentration of the diffusing substance as a function of the transverse coordinate y, and t is the time the two regions has spent together [73]. The error function (erf) is defined as

$$erf(z) = \frac{2}{\sqrt{\pi}}\int_0^z \exp{(-v^2)}dv. \tag{3.14}$$

To use the expression for the T/Y geometry, t can be estimated from the average flow speed (U) and the distance downstream of the junction (x) through $t = x/U$. This expression is plotted in figure 3.4 for a number of different substances used in the experiments within this thesis. Figure 3.4 illustrates the large impact the diffusion coefficient has on how quickly the concentration front spreads.

The microfluidic designs used in this thesis are different versions of the Y channel, either a pure Y channel or a device containing an extra inlet

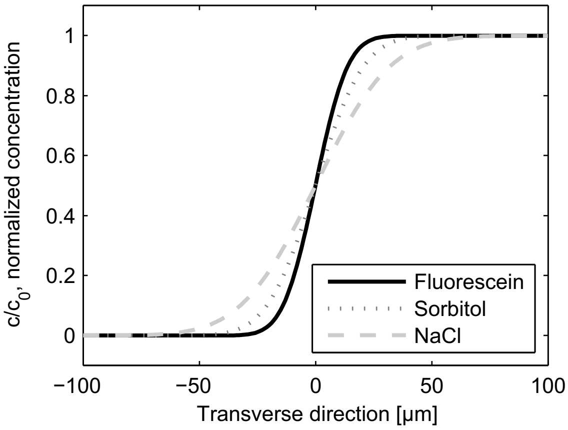

Figure 3.4: Normalized concentration profiles 50 μm downstream of a Y junction at an average flow speed of $U = 250$ μm/s for three different diffusing substances, using equation 3.13. Solid black: fluorescein ($D = 0.3 \cdot 10^{-5}$ cm^2/s), dotted dark gray: sorbitol ($D = 0.67 \cdot 10^{-5}$ cm^2/s) and dashed light gray: NaCl ($D = 1.6 \cdot 10^{-5}$ cm^2/s).

for the introduction of cells. The flow behavior and the concentration distributions within the different designs has been modelled using the Navier-Stokes equations, mass conservation and the convection-diffusion equation to better understand the environment within the devices. This becomes particularly important when simple estimates such as those based on equation 3.13 is not possible, for example when the flow velocities in the inlet channels are not equal or when one of the liquids is more viscous than the other. The simulations presented in this thesis are time independent, body forces are neglected, and contains appropriate boundary conditions. Details regarding the simulations are presented in **PAPER II**. The simulations were performed using COMSOL Multiphysics, which is a software solving partial differential equations based on the finite element method (FEM).

A simulation of the microfluidic device used in **PAPER I**, with fluorescein as the diffusing substance, is shown in figure 3.5. In figure 3.5 a) the concentration distribution is shown as well as arrows indicating the local flow velocity, while figure 3.5 b) shows the concentration profile 10 μm downstream of the junction. The experimentally measured concentration profile seems to be in good agreement with the simulated concentration profile. The red curve is the concentration at the bottom while the green curve is in the center of the device. Also included in the figure is the analytical expression in equation 3.13. As expected, the analytical expression lies between the bottom and the center, since it is based on the average flow speed.

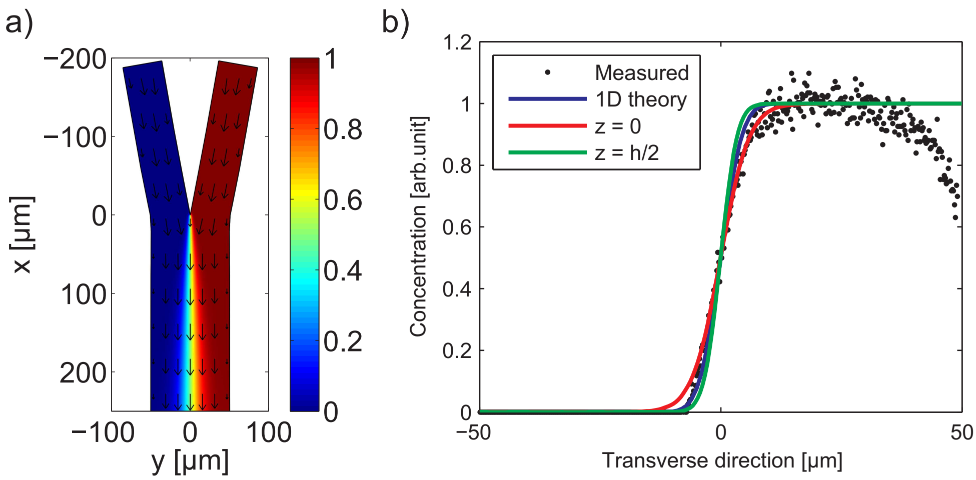

Figure 3.5: a) Simulation of the concentration of fluorescein in a Y shaped microfluidic device. The device is 27 μm high and have two 50 μm wide inlet channels merging into a 100 μm wide channel. The flow speed is 40 nl/min in both inlet channels, and the concentration of fluorescein is set to 0 for the left inlet and to 1 for the right inlet. The concentration distribution is shown at half the channel height, while the arrows indicate the flow direction and relative magnitude of the flow velocity. b) A graph showing the concentration profiles 10 μm downstream of the junction, where the black dots are experimentally measured intensity values, the blue curve is the 1D expression from equation 3.13 and the red and green curves are the simulated concentration profiles at the bottom and half the channel height, respectively.

In figure 3.6 the velocity profiles at half the channel height for a number of downstream distances are shown. Initially the velocity is lower in the center of the channel, since the flow pattern is affected by the no-slip condition on the walls of the two merging channels. The effect of the junction disappears downstream, and the expected plug-like profile is reached.

The fact that the concentration gradient broadens more quickly close to the bottom or the top of the device is a consequence of the parabolic velocity profile. Due to the no-slip condition, the fluid close to the walls is moving very slowly and therefore, at a certain downstream distance, the two flows have had more time to mix. The result is a less steep concentration gradient compared to in the center of the device, where the flow speed is the highest. This effect is sometimes referred to as the “butterfly” effect, and can be seen more clearly in figure 3.7. It has been shown that close to the top and bottom of the channel, the width of the mixing zone in a T-channel initially grows as $x^{1/3}$ rather than $x^{1/2}$ due to the diffusion in the height

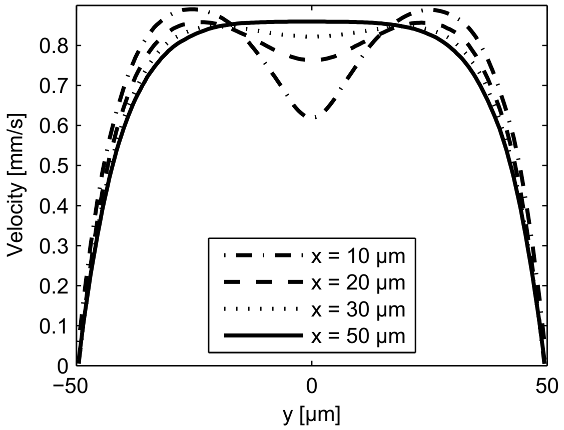

Figure 3.6: Flow velocity profiles at different distances downstream of the junction in the device shown in figure 3.5.

direction [74]. However, for distances far downstream of the junction, the mixing reverts to growing as $x^{1/2}$ at all heights [75].

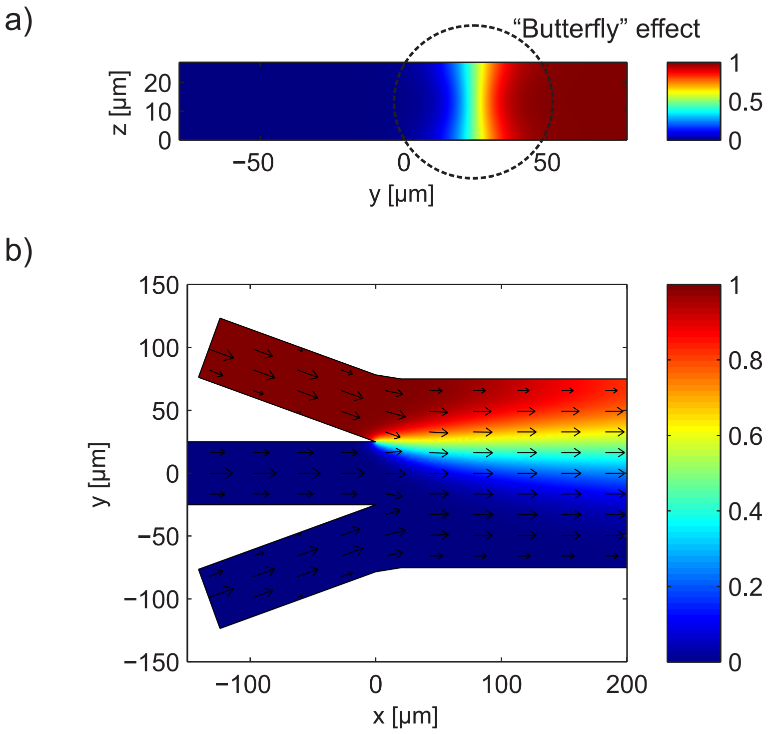

Figure 3.7: a) Simulation of the faster broadening of the concentration gradient close to the top and bottom of the device (the "butterfly" effect). The simulation is made for NaCl as the diffusing substance and the cross section shown is transverse to the flow direction 10 μm downstream of the junction (the junction is located at $x = 0$ μm, $y = +25$ μm). b) xy view of the same microfluidic system at half the channel height ($h = 27$ μm). 1 M NaCl is added to the uppermost inlet, the media in the other inlets are pure water; all three inlet channels are 50 μm wide and have inlet flow rates of 40 nl/min. Arrows represent the local flow velocities.

Chapter 4

Optical tweezers

Optical tweezers are a tool that can be used for trapping and manipulation of small transparent objects, such as cells and bacteria. This is possible since light carries momentum and thus can exert forces, or radiation pressure, on matter. The transfer of momentum from light to matter is also part of the reason why the tail of a comet always points away from the sun. Johannes Kepler attributed this to the radiation from the sun already in the 17^{th} century. However, it was not until the advent of the laser that it became possible to exert sufficiently large forces to displace microscopic or nanoscale objects in the laboratory. Arthur Ashkin did pioneering work in the 1970's regarding the effects of radiation pressure, and in 1986 he experimentally demonstrated stable trapping of 25 nm - 10 μm dielectric particles, using a single strongly focused laser beam (the single-beam gradient force optical trap), usually referred to as "optical tweezers" [76]. A year later Ashkin also demonstrated trapping of viruses, bacteria and eukaryotic cells, as well as the manipulation of organelles within cells [34, 35]. By using infrared laser light for trapping, absorption and optical damage could be reduced, allowing cells to reproduce within the optical trap. Numerous studies have characterized photodamage and cell viability in optical tweezers [38, 77–80].

Apart from the laser providing the light for optical trapping, a key component in the optical setup is a powerful lens, able to strongly focus the light to enable stable three dimensional trapping. This is possible with a high numerical aperture microscope objective. Thus, optical trapping can preferably be performed with the same microscope objective as is used for imaging of the sample. Optical tweezers have been combined with most modern optical imaging techniques, such as epi-fluorescence, confocal and multiphoton microscopy [81, 82]. Optical tweezers can therefore successfully be introduced to microscopy based single cell studies.

One specific application of optical tweezers is optical force measurements (OFM). By measuring the displacement of a bead or cell from its equilibrium position in the trap, forces in the pN range can be measured. Because of their spherical shape, polystyrene or silica beads are often trapped and used as probes in OFM in order to measure forces in biological systems. Beads can also be used as handles when it is not possible to trap the biological objects themselves, e.g., biological macromolecules such as DNA or RNA, or when the sample is absorbing the light [83].

Optical tweezers are indeed well suited for manipulating single cells. However, sometimes it is desirable to manipulate several cells simultaneously, e.g., for parallel collection of data on single cells, for statistical relevance. This was made possible with the introduction of spatial light modulators (SLMs) in the optical setup, forming so called holographic optical tweezers (HOTs) [44, 84]. By updating a phase hologram displayed on the SLM it is possible to move several trapped cells individually in three dimensions in realtime. A possible application of HOTs could be for OFM, where forces could ideally be measured in several positions simultaneously [85–88]. The technique of holographic optical tweezers is still under development, and the reports regarding the use of HOTs for biological applications have so far been quite few, e.g., [88–92].

Optical tweezers are used in all single cell experiments presented in this thesis. The basics regarding the mechanisms for optical trapping are therefore described in this chapter together with practical issues related to the construction of a well working optical tweezers setup. Part of my work has been concerning how holographic optical tweezers can be used to increase the throughput in single cell experiments. Thus, the fundamentals of holographic optical beam steering is also presented. Some of my work has strived towards the use of HOTs for OFM. In the end of this chapter some aspects on this specific use of HOTs are discussed together with related experimental results.

4.1 Single beam gradient force optical trap - optical tweezers

Traditionally there are two main theories that explain the trapping mechanisms in optical tweezers [93]. When the trapped object is much smaller than the wavelength of the trapping laser beam, i.e., $a \ll \lambda$, trapping can be explained by treating the object as an induced point dipole effected by an electromagnetic field. The time-averaged trapping force arises from the

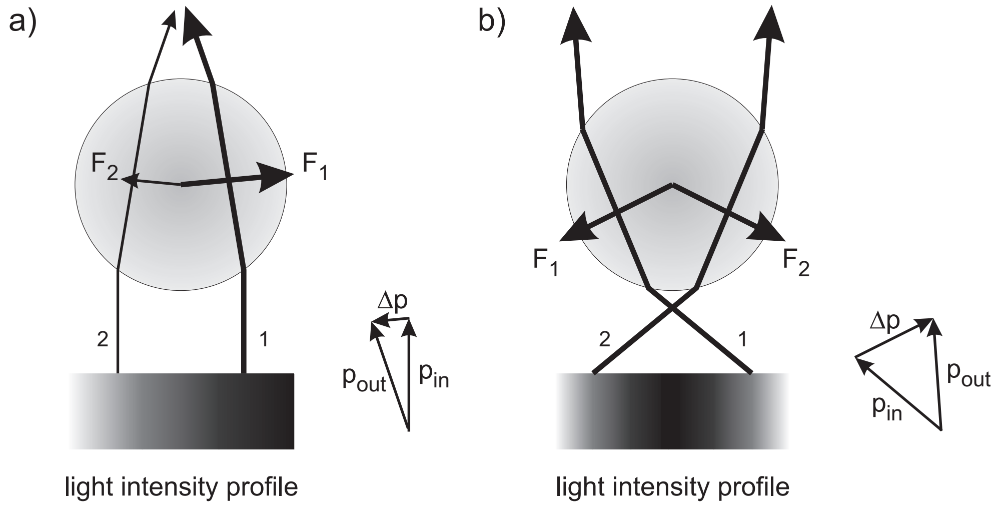

Figure 4.1: a) Illustration of the gradient force in the ray optics regime. A parallel beam of light with an intensity gradient increasing from left to right is incident on a transparent bead. The momentum of the photons is changed when the rays are refracted. The difference between the incoming and outgoing momentum, Δp, is the momentum gained by the photon (here illustrated for ray 1). By momentum conservation, the bead must then change it's momentum by the same amount but in the opposite direction. The result is a force, F_1, acting on the bead. b) In a stable optical trap the light is strongly focused. The resulting forces from ray 1 and 2 now points backwards, towards the laser focus, making stable 3D trapping possible.

interaction of the induced dipole with the gradient of the field. This theory, using wave optics, is referred to as the Rayleigh approximation. In the other extreme, i.e when $a \gg \lambda$, the conditions for Mie scattering are fulfilled, and the optical forces can be described using ray optics. This theory uses Snell's law of refraction and Fresnel's equations for reflection and transmission, and is outlined in more detail below. When the trapped object has a size comparable to the wavelength, which is often the case for biological objects, neither of the two theories is strictly valid to describe the optical trapping forces. Instead, more complete electromagnetic theories must be used.

An illustration of the trapping forces in the ray-optics regime is shown in figure 4.1. In figure 4.1a) a laser beam of increasing intensity from left to right is incident on a transparent sphere with a refractive index higher than the surrounding medium. The beam can be considered as a collection of rays, but for simplicity only two rays are shown, indicated by 1 and 2, where the ray from the more intense part of the beam, 1, is represented by a thicker line. Neglecting surface reflection and absorption, the rays are purely refracted in the surface of the sphere according to Snell's law. The refraction results in a different direction of the ray when leaving the bead, compared to the initial direction. Since photons carry momentum, the momentum of the ray has therefore changed, as illustrated for ray 1 in the vector diagram, by the amount Δp. According to Newton's third law, the sphere must therefore have gained an equal amount of momentum but of the opposite sign. The force on the sphere is thus given by the rate of momentum change, which is directly proportional to the light intensity. Thus, the ray denoted by 1 exerts a larger force, F_1, than the weaker ray 2 exerting the force F_2. The resulting net force will therefore be mainly directed towards the right in figure 4.1a), i.e., in the direction of the spatial intensity gradient (there is also a small component of the resulting force pointing in the direction of the incoming rays). The resulting force is usually divided into a scattering force, pointing in the direction of the incoming ray, and a gradient force acting in the perpendicular direction, i.e in the direction of the spatial intensity gradient. It is the gradient force that can be used for trapping, while the scattering force has the effect of pushing the particle in the direction of the ray. In the case illustrated in figure 4.1a), the net force still has a component in the direction of light propagation (both F_1 and F_2 have small components in the direction of the incoming rays), and stable trapping in three dimensions cannot occur. To achieve stable trapping, the light must be focused strongly, producing a three dimensional intensity gradient, as in figure 4.1b). In the illustrated case the intensity distribution is radial, which is the case for Gaussian laser beams. Tracing two rays through the bead, the resulting forces points backward towards the laser focus, i.e., the forces in the axial direction resulting from the intensity gradient in the axial direction are larger than the forces trying to push the bead away. The consequence is that if the sphere is displaced from the equilibrium position near the laser focus, the optical forces will counteract the movement and push it back towards the equilibrium position. Thus, it is possible to trap objects in three dimensions by using a single strongly focused laser beam.

Analytical expressions for the scattering force and gradient force, respectively, exerted on a non-absorbing dielectric sphere by a ray of light were derived by Ashkin in 1992 [94], and are presented in the following. A ray of light in a medium with index of refraction n_1 carries a momentum per second of $n_1 P/c$, where P is the power of the ray and c is the speed of light. This ray enters the sphere at an angle of incidence θ, as illustrated in figure 4.2. The ray is partly reflected in the surface, described by the reflection coefficient R, and partly transmitted with transmission coefficient T. These coefficients are given by the Fresnel equations and are dependent

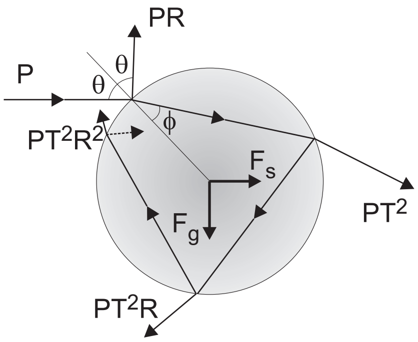

Figure 4.2: Geometry used for the calculation of the forces exerted by a single ray of power P incident on a sphere with an angle of incidence θ. The ray is partly reflected in the first surface, giving rise to the term PR, and partly transmitted, resulting in an infinite number of refracted rays of power PT^2R^n, where R and T are the reflection and transmission coefficients, respectively.

on the refractive indices of both the sphere and the surrounding medium, the polarization of the light and the angle of incidence. The angle of the refracted ray within the sphere, ϕ, is obtained from Snell's law. The total force that the ray exerts on the sphere is the sum of the forces exerted by the reflected ray of power PR and the infinite number of refracted rays of successively decreasing power PT^2, PT^2R, PT^2R^2, ... *etc.* The net force acting through the center of the sphere, can be divided into a scattering force in the direction of the incident ray, F_s, and a gradient force in the perpendicular direction, F_g. These are given by

$$F_s = \frac{n_1 P}{c}\left[1 + R\cos 2\theta - \frac{T^2\left[\cos(2\theta - 2\phi) + R\cos 2\theta\right]}{1 + R^2 + 2R\cos 2\phi}\right] \tag{4.1}$$

$$F_g = \frac{n_1 P}{c}\left[R\sin 2\theta - \frac{T^2\left[\sin(2\theta - 2\phi) + R\sin 2\theta\right]}{1 + R^2 + 2R\cos 2\phi}\right]. \tag{4.2}$$

The total force that a focused beam exerts on a bead will depend on the angular distributions of the rays, which in turn depends on the laser beam profile, the design and the numerical aperture of the microscope objective. The total force is given by integrating the expressions for a single ray over the entire incoming beam. From such calculations it is possible to conclude that incident rays with a large angle contribute to a greater extent to the trapping force than rays with a smaller angle. Stable three dimensional trapping requires that the gradient force in the beam propagation direction is larger than the scattering force. Due to the scattering force, the axial equilibrium position of a trapped particle will be located slightly behind the focal point (i.e., down-beam of the focal point).

A common way to quantify the contributions of the two forces in an optical trap is through the dimensionless quality factor, Q, referred to as the normalized force

$$F = Q\frac{n_1 P}{c}. \tag{4.3}$$

Q can obtain a maximum value of 2 for a ray reflected perpendicularly in a perfectly reflecting mirror, while Q is equal to 1 if all light is absorbed.

4.1.1 Basic optical tweezers setup

The basic optical and optomechanical elements needed for an optical tweezers setup are a laser, beam expansion optics, steering optics, a high NA objective, a holder for the sample and some means of observing the trapped objects. Conventional optical tweezers use a Gaussian TEM_{00} mode laser beam with good pointing stability and low power fluctuations. The optical tweezers are preferably configured around an inverted optical microscope, which can then also be used to image the sample. In addition, the microscope can be used to provide focus functions and means to control movements of the microscope table. The use of an inverted microscope keeps the laser beam path close to the optical table, which is good both for safety reasons and for mechanical stability. An inverted microscope also facilitates the introduction of the laser beam into the optical path of the microscope before the objective. The laser beam can be introduced via a dichroic mirror that reflects the wavelength of the trapping laser light but transmits the wavelengths used for imaging the sample.

Several microscope designs allow the laser beam to be introduced via a dichroic mirror positioned at a 45° angle between the microscope objective and the filter cube cassette. This configuration allows the filter cubes for imaging to be changed without affecting the optical trapping, which is important when imaging multiple fluorescent probes with a monochrome camera. For trapping of biological samples, infrared laser light should be used to minimize optical damage. This is convenient also for the design of the dichroic mirror, which can be constructed to transmit light in the entire visible wavelength range used for imaging. An alternative approach would be to use the same dichroic mirror for the reflection of both the fluorescence excitation wavelengths and the wavelength of the trapping laser beam. Multi-band dichroic mirrors and filters must then be used in the filter cube to allow multicolor imaging, since the filter cube cannot be changed without releasing the trapped object.

The strong focussing of the laser light needed for stable three dimensional trapping can be achieved using a microscope objective with a high

NA. Thus, immersion objectives are normally used to obtain a NA above 1. The external optics are usually arranged so that the plane where objects are trapped coincides with the imaging plane. This allows the same microscope objective to be used simultaneously for both optical trapping and imaging. The fact that the optical trapping plane coincides with the imaging plane also improves the quality of the trap, since microscope objectives are designed to minimize aberrations near the image plane. For infinity corrected objectives this implies that the laser beam should be collimated when entering the objective. Optimum trapping performance is obtained when the laser beam is expanded so that the $1/e^2$ intensity overfills the objective back aperture by around 10%, depending on the exact experimental conditions [95].

The optical trap can be moved within the sample using a number of different approaches. For xy movement of a single trap the easiest method is to move the microscope table. This is also the only way to move the trap over large distances (larger than the field of view). The trap is in this case kept at a fixed position, on the optical axis, relative to the objective. The direction of the laser beam must be changed to move the trap within the field of view. This can be achieved by moving one of the lenses external to the microscope, or by changing the direction of the laser beam using a gimbal mounted galvanometric or piezoelectric scanning mirror, an acousto-optic modulator (AOM) or a spatial light modulator (see below). The two last approaches can also be used to split the laser light into several optical traps, which can be steered individually in two dimensions (AOM) or three dimensions (SLM). The trap can be moved in the axial (z) direction relative to the coverslip, by moving the microscope objective or the sample up and down. In both cases the trapped object remains in the image plane of the objective, while the object is moved with respect to the surrounding medium. The optical trap can also be moved relative to the image plane by changing the divergence of the laser beam. This can be realized by moving one of the external lenses in the axial direction, or by using an SLM.

An example of an optical setup that can be used to realize optical trapping is shown in figure 4.3. This configuration ensures a constant degree of overfilling of the objective, thus maintaining the laser power in the optical trap constant, during movement of the optical trap in the x, y and z directions, as outlined by Fällman *et al.* [96].

In this setup the laser beam is first expanded by an afocal telescope containing lenses L_1 and L_2. The laser light is then reflected in a gimbal mounted mirror (GMM) that is imaged onto the back aperture of the microscope objective by a second afocal telescope (lenses L_3 and L_4) in a 4-f configuration. The total transverse magnification of the two telescopes,

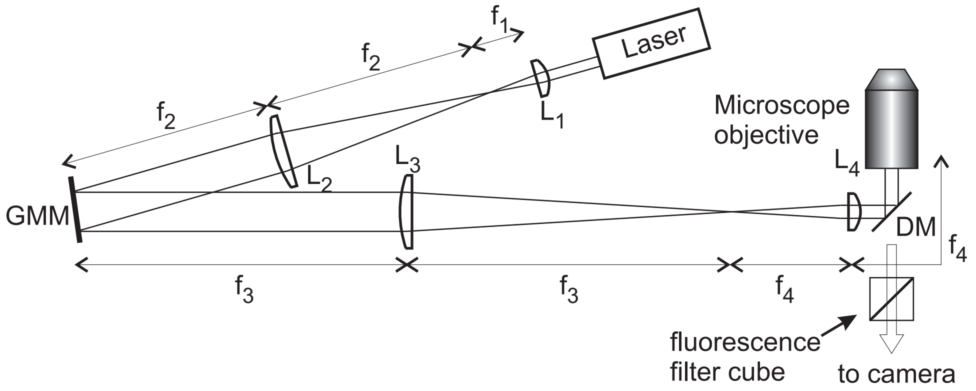

Figure 4.3: A typical optical tweezers setup. The first telescope (lenses L_1 and L_2) serves to expand the laser beam and provides movement of the optical trap in the axial direction through movement of lens L_1 along the optical axis. The second telescope (L_3 and L_4) images the gimbal mounted mirror (GMM) onto the back aperture of the microscope objective, via the dichroic mirror (DM). Tilting of the GMM translates into xy movement of the trap.

$f_2/f_1 \cdot f_4/f_3$, should be chosen such that the appropriate degree of overfilling of the objective back aperture is obtained. A gimbal mount allows the mirror to be tilted around its center position without any translation of the mirror. Thus, if the laser beam is centered on the mirror and the mirror is imaged onto the back aperture of the microscope objective, tilting the mirror only results in a change of the angle of the laser beam entering the microscope objective, without affecting the degree of overfilling. In other words, the laser beam will pivot around the back aperture of the microscope objective.

Tilting the GMM thus results in an xy movement of the optical trap. If the laser beam forms an angle α with the optical axis when leaving the GMM, it will enter the microscope objective with an angle β according to

$$\tan\beta = \frac{f_3}{f_4}\tan\alpha. \tag{4.4}$$

Since the angles needed for steering of the optical tweezers are usually small, the angle of the laser beam entering the objective is thus a factor of f_3/f_4 larger than the angle formed with the optical axis at the GMM. The tilting of the laser beam when entering the objective is converted to a transverse translation, r, in the trapping plane according to

$$r = f_{MO}\tan\beta, \tag{4.5}$$

where f_{MO} is the effective focal length of the microscope objective. For a microscope objective with $f_{MO} = 2.0$ mm, an angle of $\beta = 5.0$ mrad is thus required to move the optical trap 10 μm.

A movement of the trap in the axial direction, that simultaneously keeps the degree of overfilling of the objective, can be achieved by moving lens L_1 along the optical axis. This requires that the lens L_2 is placed at focal length distance from the GMM. Translating L_1 a distance Δd_{12} corresponds to a movement of the optical trap in the axial direction, Δz, by:

$$\Delta z = \left(\frac{f_{MO}}{f_4}\right)^2 \left(\frac{f_3}{f_2}\right)^2 \Delta d_{12}. \tag{4.6}$$

An alternative way of achieving movement in the axial direction is by moving lens L_3 in the axial direction, which results in movement of the optical trap according to

$$\Delta z = \left(\frac{f_{MO}}{f_4}\right)^2 \Delta d_{34}, \tag{4.7}$$

where Δd_{34} is the distance that L_3 is moved. This keeps the degree of overfilling at the back aperture if the optical trap is not simultaneously moved in the x or y direction through tilting of the GMM. However, even when combined with xy movements the change in degree of overfilling of the back aperture is small, since only the position of the beam at the back aperture, not the size, is affected by the tilting of the GMM when L_3 has been moved.

4.1.2 Optical force measurements

Close to the focus an optically trapped particle in a Gaussian beam behaves like a particle in a harmonic potential, where the position of minimum energy is in the center of the optical trap. For small displacements from this center, the trapped object will experience a restoring force proportional to the displacement, thus acting like a Hookean spring:

$$F = -\kappa\,\Delta x, \tag{4.8}$$

where F is the restoring force due to a displacement Δx, and κ is the stiffness of the optical trap. Thus, if the stiffness of the optical trap is known and the displacement of the object can be measured, forces down to the femto-Newton regime can be achieved [36]. Usually homogenous beads are used as handles to measure these forces.

The position of the bead in the optical trap can be monitored using a position sensitive detector (PSD) that measures the deflection of the trapping laser or a second probe laser passed through the bead, or using a camera with subsequent particle tracking [97]. Generally, a PSD provides better resolution, both spatially and temporally, compared to a camera. However, PSDs are usually limited to measure the position of a single bead, while a camera in principle allows to monitor the position of several beads simultaneously.

One method for determining the stiffness of the optical trap is to look at the Lorentian power spectrum of the Brownian motion of an optically trapped particle,

$$S_{xx}(f) = \frac{k_B T}{\pi^2 \gamma (f_0^2 + f^2)}, \tag{4.9}$$

where the corner (or roll-off) frequency, f_0, is given by

$$f_0 = \kappa (2\pi\gamma)^{-1}. \tag{4.10}$$

By fitting the expression to experimental data, the optical trap stiffness κ can be calculated if the hydrodynamic drag, γ, is known. For a sphere of radius a far from any surface, γ is given by the Stokes drag coefficient $\gamma = 6\pi\eta a$. Close to a surface the drag is modified with a correction term, the so called Faxen's correction [93].

Typically, the corner frequency for a trapped micron-sized particle is of the order of a few hundred to a few thousand Hertz (depending linearly on the laser power). The detector system must have a bandwidth able to record the power spectrum well beyond the corner frequency, preferably by more than one order of magnitude, in order to measure this correctly [93]. Thus, using the power spectrum for calibration of the stiffness of the optical trap, limits experiments using a camera for position detection to experiments with optical traps of relatively low stiffness, since cameras have comparatively low frame rates. The amount of illumination light available also sets an upper limit to the frame rate possible to use.

4.2 Holographic optical tweezers

In order to create several optical traps holographic optical tweezers (HOTs) can be used, which is based on the principles of diffractive optics. A diffractive element placed in a conjugate plane to the back focal plane of the microscope objective produces an intensity distribution in the specimen plane that is the Fourier transform of the pattern imposed by the element. This relationship is used in several algorithms to calculate the hologram needed to produce a desired trapping pattern. Static optical trapping patterns can be obtained using, e.g., a computer-generated phase mask etched into a glass substrate. In order to move optically trapped objects relative to each other, an optical device on which holograms can be changed dynamically is needed. This can be realized by incorporating an SLM in the optical setup forming the optical tweezers. To displace the optically trapped objects, a sequence of holograms are updated on the SLM, where each hologram moves the optical traps a short distance compared to the positions produced by the previous hologram. This allows multiple optically trapped objects to be moved in three dimensions. In addition, an SLM can produce more exotic trapping beams, such as Laguerre-Gaussian or Bessel beams [93].

The performance of dynamic holographic optical tweezers is currently limited by the optical characteristics and the update rate of the SLM, and the time required to calculate the hologram. For instance, the number and size of the pixels in the SLM restrict the complexity and the range of motion of generated optical traps, while the pixelation and discrete phase steps of the SLM result in diffractive losses.

4.2.1 The spatial light modulator

An SLM is a device that modulates the phase and/or the amplitude of light that is reflected in or transmitted through the device. For optical trapping a constant power in the individual traps is often desired, as for the case of OFM, and the amount of available laser power is often limited. Thus it is advantageous to use an SLM that only modulates the phase of the incoming light but does not affect the amplitude.

To obtain a good diffraction efficiency, a close to continuous modulation of the phase between 0 and 2π is desired. This can be achieved with an SLM based on a parallel aligned nematic liquid crystal [98]. This configuration also allows the polarization state of the light being modulated by the device to remain unaffected. The SLM is divided into a number of pixels, where the phase of the light leaving each pixel can be controlled individually, by controlling the effective refractive index, and thus the optical path length, of the pixel, see figure 4.4. The liquid crystal is encapsulated between two glass plates that contain electrodes for controlling the voltage over the liquid crystal. Such a parallel aligned nematic liquid crystal cell is illustrated in figure 4.4b), where the liquid crystal molecules are assumed to have positive optical and dielectric anisotropy. At zero electric field the liquid crystal molecules are aligned parallel to the glass substrates, see figure 4.4b) (top). Light polarized along the director will then experience

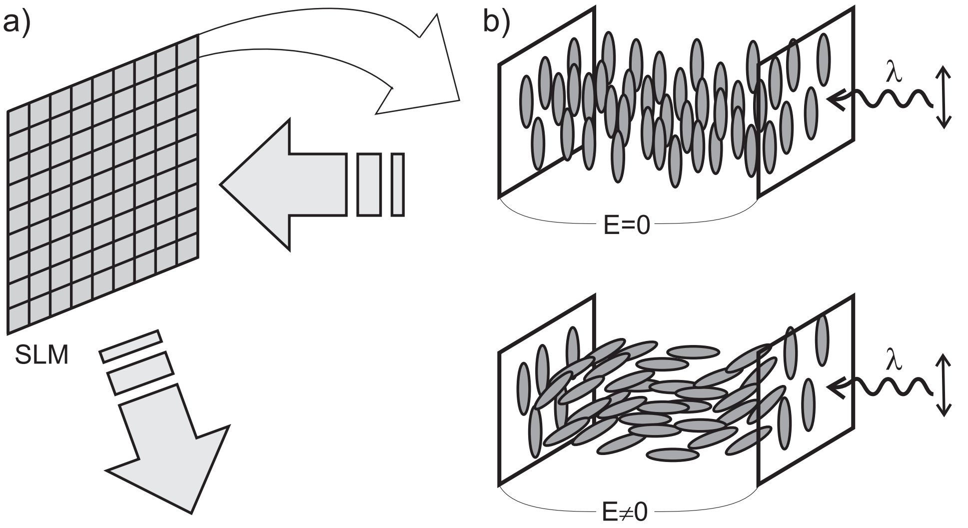

Figure 4.4: a) The SLM consist of a number of pixels, where the refractive index can be controlled individually for each pixel, thus modulating the phase of the light leaving each pixel. b) The principle of phase modulation in a parallel aligned nematic liquid crystal pixel. Top: when no electric field is applied the molecules tend to align parallel to the glass substrates. Bottom: when an electric field is applied the molecules align with the field and the effective refractive index of the pixel is changed.

a refractive index equal to the extraordinary refractive index. When an electric field is applied, the molecules will start to tilt in the direction of the field, see figure 4.4b) (bottom). The incoming light will therefore see a different effective refractive index, that approaches the ordinary refractive index for large electric fields when effectively all molecules are aligned in the direction of the field. Thus, when continuously increasing the electric field the phase of the linearly polarized light passing through the pixel is changed in an analogue manner.

To control the electric field over the liquid crystal, the device can be electrically or optically addressed. Many commercial SLMs work in reflective mode, such that the light is passed through the liquid crystal before and after being reflected in a mirror. Optically addressed SLM:s often have a better surface flatness, resulting in less introduced geometrical aberrations by the SLM. These aberrations can, however, be compensated for by adding a suitable phase hologram to the hologram representing the optical traps displayed on the SLM [99, 100]. The work related to HOT performed in this thesis is based on parallel aligned nematic liquid crystal SLMs as described above. There are also other types of SLMs, such as ferroelectric SLMs, that are used in HOTs [101]. These are much faster, but on the other hand suffer from the limitation of only being able to provide two phase levels.

4.2.2 HOT setup

The optical setup presented in figure 4.3 is suitable also for holographic optical tweezers, if the GMM is replaced by an SLM, and if the laser is linearly polarized with a polarization direction aligned to the orientation of the liquid crystal in the SLM. The face of the SLM is thus positioned in a plane conjugate to the microscope back aperture. The magnification of the two telescopes must also take the size of the phase modulating area of the SLM into account. The transverse magnification of the second telescope (L_3 and L_4) should thus be chosen such that the SLM size, d_{SLM}, is reduced to the size of the microscope objective back aperture, d_{MO}, according to

$$d_{MO} = \frac{f_4}{f_3}\, d_{SLM}. \tag{4.11}$$

The magnification of the first telescope (L_1 and L_2) follows from the requirement that the total magnification of the two telescopes should assure that the laser beam has a suitable degree of overfilling of the back aperture when entering the microscope objective.

In practice, SLMs only diffract a portion of the incident light into the specified spots. Some light may not be diffracted at all, and typically forms an unwanted trap in the middle of the field of view. This optical trap is referred to as the zeroth order optical trap. Different experimental approaches have been demonstrated to reduce the problem of the zeroth order optical trap as well as other undesired traps, so called, ghost traps [102, 103].

4.2.3 Beam steering using diffractive optics

In diffractive optics, diffraction is used to control the shape of wavefronts. A device capable of shaping the wavefront in this manner is referred to as a diffractive optical element (DOE). These can modulate the amplitude and/or the phase of the light. For optical tweezers applications it is generally desired to modulate only the phase.

A basic task for a DOE to perform is to change the direction of a laser beam. This is achieved using a blazed grating, which is the diffractive equivalent of a refractive prism, see figures 4.5a) and b). The blazed grating can be thought of as a prism sliced into pieces with a thickness corresponding to an optical path length of one wavelength, where all rectangular sections

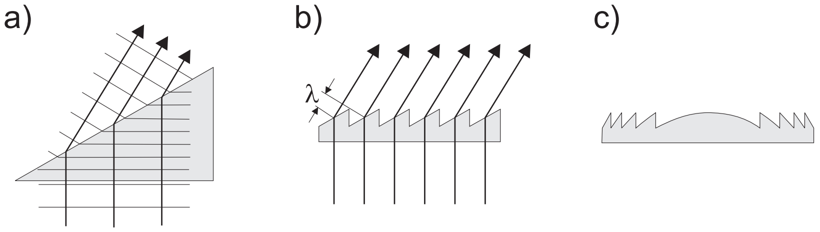

Figure 4.5: a) Refractive prism, b) Blazed grating, c) Fresnel lens.

(that do not contribute to a relative change in the optical path length) are removed. Thus the slopes are the same for the pieces in the blazed grating as for the prism. However, the wavefront will not be continuous, but instead consist of a set of pieces of different wavefronts from the incident wave. The result of the blazed grating is that all incoming light with a wavelength that coincides with the design wavelength is directed into the first diffraction order.

Another basic diffractive component is the Fresnel lens, see figure 4.5c). In a similar manner as for the blazed grating, each the DOE is divided into parts where each part of the device induces an optical path length difference of one wavelength (corresponding to a phase shift of 2π). A problem with the diffractive versions of optical elements is that they work well only for the design wavelength. The phase profiles that can be induced by a DOE are of course not limited to blazed gratings and Fresnel lenses. In fact, DOEs can create wavefronts not possible using conventional refractive optics. This opens for new optical functions, such as splitting a laser beam into several beams and focusing them in different optical planes. For optical trapping this enables the trapping of several particles in different axial planes simultaneously.

The diffractive devices presented in figure 4.5 modulate the optical path length, and thus the relative phase of the light passing the different parts, by controlling the thickness of the DOE. An SLM instead controls the optical path length by changing the refractive index of each pixel, while the thickness of the device is constant. The net result in both cases is that the relative phase is controlled for each piece of the wavefront. The blazed grating in figure 4.5b) has a continuous slope on each element, resulting in a “sawtooth” like wavefront. However, since a real SLM has a finite number of pixels, the smooth slope of each element (grating period) is approximated by a staircase, that reflects the pixelation of the device. In addition, the number of available phase levels is also finite, which is referred to as quantization of phase levels. Consequently, the wavefront leaving the SLM will

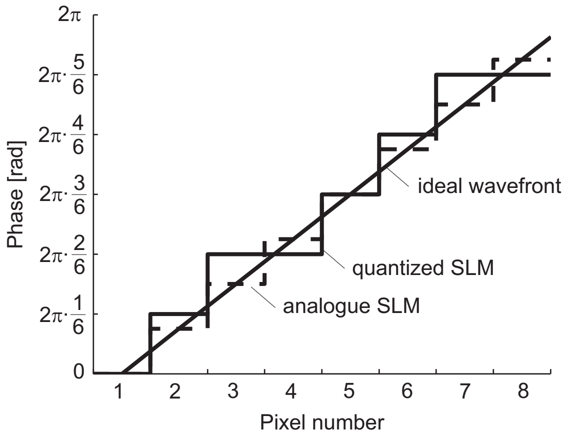

Figure 4.6: Ideal phase modulation and approximate phase modulation due to the pixelation of the SLM and the finite number of phase levels (quantization). Both the approximated phase modulation for an analogue SLM (infinite number of phase levels) and for a quantized SLM with a limited number of phase levels (here 6 levels) are shown.

deviate from the ideal wedge shape (or more generally "sawtooth" shape), as illustrated in figure 4.6.

The finite numbers of pixels and phase levels will result in a reduced diffraction efficiency, η, defined as the ratio between the optical power directed to the desired positions and the total power leaving the SLM. Most commercial SLMs based on nematic liquid crystals have a number of phase levels large enough not to be a limiting factor on the diffraction efficiency. However, it is indeed a limitation for ferroelectric SLMs with only two phase levels. The diffraction efficiency for an SLM with 256 phase levels is shown in figure 4.7. The diffraction efficiency of the first order for a blazed grating is plotted as a function of the normalized steering angle, α/α_{max}, where α_{max} refers to the maximum achievable deflection of the first order beam (see below). Also shown in the figure are a few approximations to the profile of an ideal blazed grating by four gratings with different number of phase levels, and the resulting first order diffraction efficiencies. The diffraction efficiency also depends on the fill-factor of the SLM, i.e., the ratio of pixel width to pixel pitch, where the diffraction efficiency decreases for larger dead space between neighboring pixels [87].

The deflection angle, α_m, at normal incidence is given by the grating equation

$$\sin\alpha_m = \frac{m\lambda}{\Lambda p}, \tag{4.12}$$

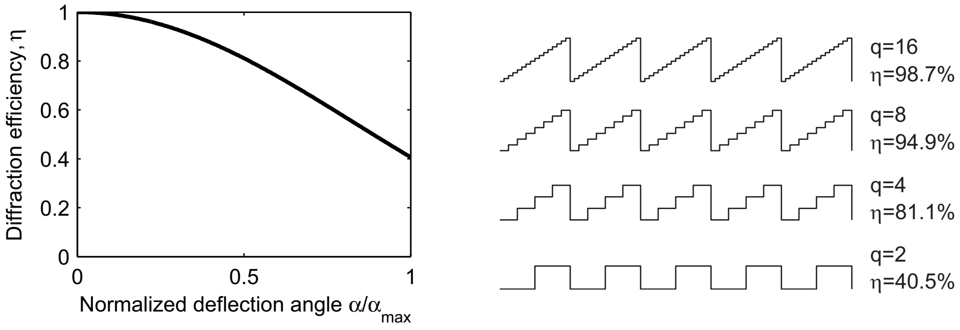

Figure 4.7: Left: First order diffraction efficiency, η, as a function of normalized steering angle for an SLM with $M = 256$ phase levels. At the maximum deflection angle the blazed grating becomes binary, resulting in a $\eta = 40.5\%$ (the same amount is by symmetry diffracted into the -1 order). Right: A few approximations to the profile of an ideal blazed grating by four gratings with different number of phase levels, and the corresponding first order diffraction efficiency.

where m is the number of the diffraction order, λ is the wavelength, Λ is the period of the grating in terms of number of pixels, and p is the pixel pitch. The maximum deflection for the first order diffracted beam is obtained when the period of the grating is two pixels, i.e., a binary grating,

$$\alpha_{max} = \sin^{-1}\left(\frac{\lambda}{2p}\right). \tag{4.13}$$

As an example, the Hamamatsu X8267-15 SLM (used in many of my experiments) has $N = 768$ pixels over a distance of $d_{SLM} = 20$ mm (i.e., $p = 26$ μm), resulting in a maximum deflection of $\alpha_{max} = 20.5$ mrad at $\lambda = 1070$ nm. In our HOT setup, $f_3 = 375$ mm, $f_4 = 100$ mm and $f_{MO} = 2.0$ mm, the maximum lateral displacement is $r = 154$ μm according to equations 4.4 and 4.5. Thus the trapped object can be moved without problem within the entire field of view of the camera, which is typically around 80 μm using the 100× objective.

Fourier optics

For applications of holographic optical tweezers it is important to calculate the phase hologram to be displayed on the SLM. To accomplish this we must know the propagation of light through the optical system. In the following discussion it is assumed that we are dealing with scalar electric fields, i.e., that the electric field has the same polarization everywhere.

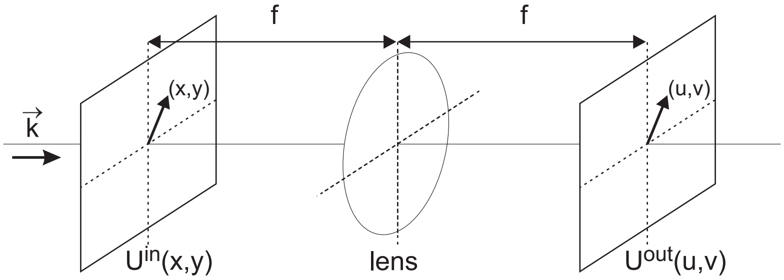

Figure 4.8: Monochromatic light with wave vector $\vec{k}$ incident on the input plane (e.g., the back focal plane of the microscope objective). A lens, e.g., a microscope objective, of focal length f projects the Fourier transform of the field in the input plane, $U^{in}(x,y)$, onto the front focal plane, resulting in field $U^{out}(u,v)$.

A monochromatic scalar electric field propagating in the $+z$ direction can be described by

$$\begin{aligned} E(\rho,t) &= E_0(\rho)\cos(-\omega t+\varphi(\rho)) && (4.14)\\ &= E_0(\rho)\mathrm{Re}\left[e^{i(-\omega t+\varphi(\rho))}\right] && (4.15)\end{aligned}$$

where $\rho = x\hat{x} + y\hat{y} + z\hat{z}$ is the spatial coordinate, ω the angular frequency and t the time. It is often convenient to use the complex analytical form for $E(\rho,t)$

$$U(\rho) = E_0(\rho)e^{i\varphi(\rho)} \tag{4.16}$$

where the electric field is obtained by

$$E(\rho,t) = \mathrm{Re}\left[U(\rho)e^{-i\omega t}\right] \tag{4.17}$$

A planar array of optical traps can be described by the intensity distribution $I^{out}(u,v)$ of laser light in the front focal plane of the microscope objective. The intensity distribution is proportional to the square of the absolute value of electric field, $|U^{out}(u,v)|^2$. $U^{out}(u,v)$ is determined by the electric field in the back focal plane of the objective, $U^{in}(x,y)$, as illustrated in figure 4.8.

Thus, we describe the field in the back focal plane of the objective with

$$U^{in}(x,y) = E_0^{in}(x,y)e^{i\varphi^{in}(x,y)} \tag{4.18}$$

and similarly,

$$U^{out}(u,v) = E_0^{out}(u,v)e^{i\varphi^{out}(u,v)} \tag{4.19}$$

is the electric field in the front focal plane of the objective. The field in the back focal plane and the field in the front focal plane are related according to

$$\begin{aligned} U^{out}(u,v) &= \frac{k}{2\pi f} e^{i\theta(u,v)} \iint U^{in}(x,y) e^{-i\frac{k}{f}(ux+vy)}\, \mathrm{d}x\, \mathrm{d}y \\ &\equiv \mathcal{F}\left\{U^{in}(x,y)\right\} \end{aligned} \tag{4.20}$$

where f is the focal length of the objective, $k = 2\pi/\lambda$ is the wave number of the incident light and $\mathcal{F}$ is the Fourier transform [104]. For the last equality we have neglected the constants and additional phase factor ($e^{i\theta(u,v)}$) depending on the lens' geometry, which are of little interest for calculation of the intensity distribution in the trapping plane. Thus, the field in the back focal plane of the lens is obtained directly as the Fourier transform of the field in the front focal plane of the lens. Similarly,

$$\begin{aligned} U^{in}(x,y) &= \frac{k}{2\pi f} \iint e^{-i\theta(u,v)} U^{out}(u,v) e^{i\frac{k}{f}(ux+vy)}\, \mathrm{d}x\, \mathrm{d}y \\ &\equiv \mathcal{F}^{-1}\left\{U^{out}(u,v)\right\}, \end{aligned} \tag{4.21}$$

where again the constants and phase factor are neglected for the last equality. Thus, there is a Fourier transform relationship between the electric field in the back focal plane of the microscope objective (which is conjugate to the SLM) and the electric field in the front focal plane of the objective where the optical trapping takes place.

4.2.4 Algorithms

There are several different algorithms available for calculating the phase holograms to be displayed on the SLM, corresponding to specific patterns of traps. My work has mainly been limited to the use of simple superpositions of blazed gratings and Fresnel lenses as well as algorithms based on the Gerchberg-Saxton algorithm. These are therefore the ones described in more detail below.

Gratings & Lenses

The phase gradient needed in order to steer a single trap in two dimensions in a setup like that illustrated in figure 4.3 is, assuming the small angle approximation to be valid, given by

$$\varphi_j^{prism}(x,y) = \frac{2\pi}{\lambda f_{MO}} \frac{f_4}{f_3} \left(x u_j + y v_j\right), \tag{4.22}$$

where x and y refer to the spatial coordinates in the SLM plane, and u_j and v_j are the spatial coordinates for the j^{th} trap in the trapping plane. The phase shift needed to introduce an axial shift of an optical trap is given by

$$\varphi_j^{lens}(x,y) = -\frac{2\pi}{2\lambda f_{MO}^2}\frac{f_4^2}{f_3^2}\left(x^2+y^2\right)w_j, \tag{4.23}$$

where w_j is the desired shift of the j^{th} trap (from the focal plane of the microscope objective) in the axial direction. The desired phase front for the j^{th} trap thus becomes

$$\varphi_j(x,y) = \varphi_j^{prism}(x,y) + \varphi_j^{lens}(x,y) \tag{4.24}$$

To create several optical traps the complex sum of the desired phase shifts for each of the trap positions must be calculated

$$\varphi(x,y) = arg\left(\sum_j e^{i\varphi_j(x,y)}\right). \tag{4.25}$$

Finally, when addressing the SLM all the phase values must be taken *modulo* 2π, since the SLM can only provide phase shifts between 0 and 2π.

The “gratings and lenses” approach is simple and computationally fast. However, it becomes increasingly slower the more traps that are added. It has also been shown that it often produces traps of uneven intensity between the traps and a large number of ghost traps [105]. Ghost traps can result, e.g., from higher-order diffraction peaks produced by a phase grating. For symmetric trapping patterns these ghost traps often coincides with the position of a desired optical trap, which enhances the problem of uneven distribution of laser power between the traps. A slight spatial disordering of the periodic trapping patterns, if allowed, can fortunately significantly reduce the intensity variations between the different traps without extra calculation costs [105]. However, this results in a lower diffraction efficiency.

To reduce the problem of ghost traps and decrease the unintended intensity variations between the traps an iterative algorithm is often better for calculating the desired phase holograms.

Modified Gerchberg-Saxton type algorithms

By defining the desired intensity distribution in the trapping plane, it might seem straightforward to calculate the field required in the SLM plane from equations 4.20 and 4.21. However, due to the pure phase modulation of the SLM the amplitude of the electric field in the SLM plane cannot be controlled. The amplitude in the SLM plane is instead given by the incident field, i.e., the electric field of the laser beam. Iterative algorithms using the Fourier transform relationship, such as modified versions of the Gerchberg-Saxton algorithm, can be used to calculate the phase needed to create the desired trapping pattern. This is convenient, since the fast Fourier transform (FFT) and inverse fast Fourier transform (IFFT) then can be used for the calculation.

The Gerchberg-Saxton algorithm is based on the idea that there is full phase freedom in both the SLM plane and the optical trapping plane, while the amplitude is predetermined in both planes. The amplitude in the SLM plane is determined by the intensity profile of the laser beam, while the amplitude in the Fourier plane, i.e., the plane containing the optical traps, is determined by the desired traps.

In the first iteration step the phase of the electric field in the SLM plane is randomly chosen and the amplitude of the field is set to unity or to represent the Gaussian intensity profile of the laser beam. This field is then propagated to the optical trapping plane using the FFT. Here the amplitude of the field is modified to correspond to the desired amplitude profile, while the phase of the field is left unchanged. In the next step, this updated field is propagated back to the SLM plane with the IFFT. One iteration is completed by again keeping the phase and replacing the amplitude of the field with the correct amplitude, i.e., unity or the Gaussian profile of the laser beam. This procedure is repeated until an amplitude close enough to the desired one, i.e., the amplitude of the electric field representing the desired optical traps, is reached in the trapping plane upon propagation from the SLM plane. There are a number of different approaches to update the amplitude in the trapping plane. Generally, the amplitude is not set directly to the desired amplitude, but rather as a weighted version between the desired amplitude and the current amplitude, leading to faster convergence [106, 107].

The algorithm just described only provides two-dimensional trapping, but it can be extended to three dimensions. For example, after propagation to the Fourier plane (the front focal plane of the objective), the electric field can be propagated to the desired trapping plane where the amplitude is updated for the optical traps residing in that plane. This is done for all axial planes where optical traps are desired. As the amplitudes of all traps have been updated the field is propagated back from the Fourier plane to the SLM plane.

A limitation with the FFT-based algorithms is that the beam positioning is limited to a grid with a lattice spacing that reflects the sampling interval in the SLM plane, usually chosen as the pixel pitch. This restricts the positioning of the optical traps to integer multiples of $\delta_f = \lambda f_{MO}/d_{MO}$, assuming that the size of the SLM is correctly matched to the size of the back aperture of the microscope objective [108]. Displacing the trap by δ_f corresponds to "squeezing" in one extra grating period across the spatial extent of the SLM (i.e., adding a 2π phase retardation over the extent of the SLM). Thus, for an SLM with N pixels in one dimension, the trap can be steered between $-\delta_f N/2$ and $+\delta_f N/2$ in steps of magnitude δ_f. For example, with $\lambda = 1070$ nm, $f_{MO} = 2.0$ mm and $d_{MO} = 5.2$ mm (typical values for the setup in our lab) the positional resolution using an FFT-based algorithm is $\delta_f = 0.42$ μm.

4.2.5 HOTs in a flow

A practical problem when working with a nematic liquid crystal SLM is the slow update rate. This presents a problem when moving trapped objects, i.e., when updating the hologram displayed on the SLM to a hologram representing a trapping pattern slightly different from the previous pattern. This limits the speed with which a trapped particle can be moved within the sample for any type of liquid crystal based SLM. Perhaps even more of a problem is that the update typically results in light temporarily being diverted away from the trapping region during the time that the liquid crystal rearranges to the new configuration. Consequently, the trap stiffness is decreased during this time. If a particle is optically trapped in a flow, such as within a microfluidic system, or if the particle is tethered to, e.g., a membrane during a force measurement situation, the longer it takes to update the SLM, the larger is the risk that the particle is lost. The effect of the decrease in trap stiffness is problematic for a nematic liquid crystal SLM due to its slow update rate. The decrease in trapping intensity during the SLM update and its effect on a trapped particle was investigated in the work presented in **PAPER IV**, and is summarized below.

For the Hamamatsu X8267 SLM, the time required to update the hologram is on the order of 200 ms. A measurement of the intensity in a region containing both the initial trap position and the trap position after a displacement of 0.3 μm is shown in figure 4.9. As seen in the figure, the total intensity in the region drops during the update of the hologram. In addition, we found that the amount of light diverted away from the trapping region depended on how far the trap was moved, or more generally, the average change in phase per pixel between the two holograms. For step sizes up to roughly 2 grating periods across the SLM the dip in intensity increased, while for larger steps, where we could also show that the average phase shift per pixel was approximately constant, the amount of light diverted

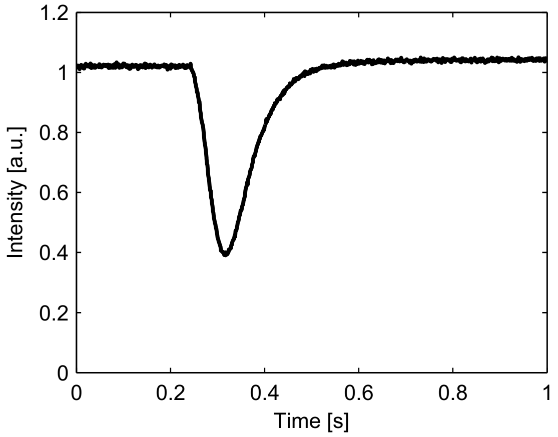

Figure 4.9: Intensity dip while the SLM is updating the new hologram.

away was held constant. In the experiments we moved a single optical trap within the field of view of the microscope using blazed gratings, where the center pixel of the SLM was kept at a constant phase value.

When an external force, such as the Stokes drag force from a flow, acts upon the trapped particle, it will move in the direction of the applied force during the temporary weakening of the trap. This displacement was measured for a number of varying parameters, while stepping the particle transverse to the flow direction. For small steps, the displacement followed the increasing depth of the intensity dip, and for intermediate step sizes the displacement was found to be constant, consistent with the constant average phase shift per pixel. There is also an upper limit to the size of the step that can be taken without risking to lose the particle, which depends upon the range of the optical trap. It was found that the largest step that could be taken before the trapped particle became increasingly displaced in the direction of the applied force, was a step corresponding to the radius of the trapped particle. This is a consequence of the restoring force of the optical trap falling off quickly outside one particle radius [94]. Above this step size the trapped particle run the risk of being lost during the SLM update.

The conclusion is thus that in applications where a quick movement of the trap is desired and a decrease in trap stiffness is tolerated, the trap can preferably be moved with steps equal to the bead/cell radius. However, in applications where it is crucial to keep a constant trap stiffness, the trap should be moved in as small steps as allowed by the HOT setup.

4.2.6 Towards holographic optical force measurements

A desirable application for holographic optical tweezers is within optical force measurements. An advantage of using holographic optical tweezers compared to a single optical trap is that forces can be measured in several positions simultaneously. When using holographic optical tweezers for quantitative force measurements, parameters such as trap stiffness and its position dependence, range of trap steering, minimum step size and trap stability are of key importance [87]. Another limiting factor is the method for detecting the trapped beads' positions. Position sensitive detectors used for measuring the position of a single bead provide high resolution and high bandwidth. However, this method is hard to extend to the trapping of multiple beads, since it is difficult to discriminate and separate the scattered light from each of the individual trapped particles [36].

A consequence of the decreasing diffraction efficiency for large deflection angles (c.f. figure 4.7) is that the trap stiffness will depend on the position of the trap within the field of view. A measurement of the trap stiffness as a function of the bead position is given in figure 4.10. The trap stiffness was extracted from the power spectrum of a trapped bead, where the bead position was monitored using a high speed camera and image processing. In the measurement presented in figure 4.10, the optical traps were created using green laser light and a microscope objective with comparatively short effective focal length. Thus the diffraction efficiency falls off quickly within the field of view. A longer wavelength of the trapping laser light and a longer effective focal length microscope objective with smaller back aperture on the other hand provides a larger trapping range according to equations 4.4, 4.5 and 4.13. For such a setup, van der Horst *et al.* found the trap stiffness to be relatively constant over large displacements [87]. This is an advantage, since it removes the need to calibrate the trap stiffness separately for each desired trap position used in a dynamic measurement. On the other hand, the larger range also increases the minimum step size that can be taken (c.f. section 4.2.4). Even though the overall positional dependence of the trap stiffness seems fairly smooth, there might be finer variations that need to be taken into account for holographic optical force measurements. For example, if the number of phase levels are limited, the diffraction efficiency is dramatically increased for phase gratings where the desired phase levels happens to coincide with the existing phase levels [109].

In the above example the power spectrum of the trapped bead was used to determine the trap stiffness. An alternative approach is to calibrate the traps against the Stokes drag force, $F_d = 6\pi\eta a v$, where v is the flow rate

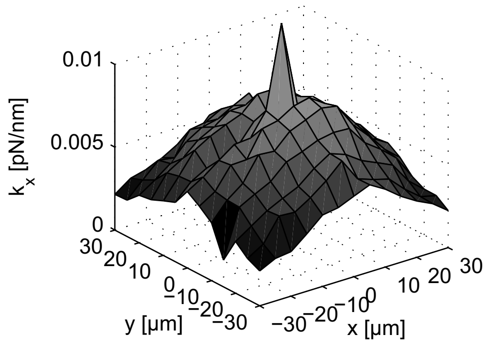

Figure 4.10: Trap stiffness in the x direction as a function of position. A silica bead 2 μm in diameter is moved using HOT within the field of view, and the position is monitored with a high-speed camera. The high trap stiffness in origo is the result of the zeroth order trap not being removed.

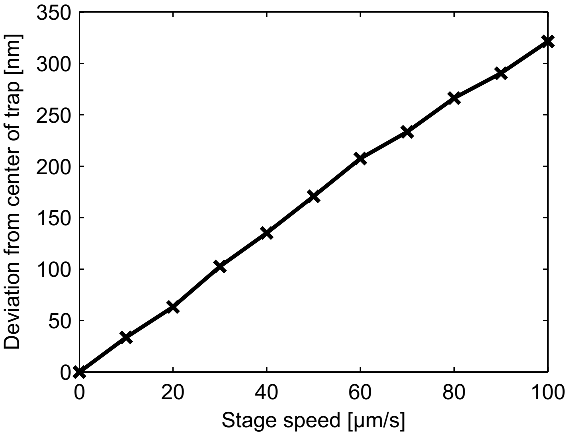

Figure 4.11: Displacement of a silica bead 2 μm in diameter from the center of the trap as a function of the applied flow rate/stage speed.

[86, 88]. For small displacements around the trap center, the restoring force increases linearly. Thus, by measuring the bead position as a function of flow rate the trap stiffness can be determined. The “flow” can for instance be created by moving a piezoelectric microscope stage. Such a measurement is presented in figure 4.11.

Another issue relevant for dynamic holographic optical force measurements is the step size possible to take when moving the trapped beads. In addition to the practical limitations due to the slow update rate of the SLM discussed in section 4.2.6, there are limitations related to both the algorithm used to calculate the holograms as well as the number of pixels (N) and number of phase levels (M). FFT based algorithms are limited to steps of size $\delta_f = \lambda f_{MO}/d_{MO}$, as discussed in section 4.2.4. By avoiding the FFT it is possible to increase the spatial resolution. Schmitz *et al.* demonstrated that the minimum step size using a single blazed grating is of the order of δ_f/k_{max} where $k_{max} = NM/2$. However, this is just a rough estimate. In particular, it can be shown that some diffraction angles are particulary difficult to steer to, e.g., angles around half the maximum deflection [110]. Preliminary results on how this phenomenon affects the positional accuracy in an holographic optical tweezers setup is demonstrated in figure 4.12. The errors or deviations from the intended trap positions in using equation 4.22 show a very non-intuitive behavior. These errors can be reduced by introducing a global phase offset, which needs to be optimized for each trap position [110]. Nevertheless, the positional resolution seems to be in the sub-nanometer range, which is below the resolution of the position detection possible using high-speed cameras [108].

Even though there are many technical issues to deal with before holographic optical force measurements can become standard procedure the technique is highly promising. The possibility to trap multiple beads simultaneously in three dimensions opens up for measurements of forces in several positions simultaneously [91], or to perform experiments on several cells in parallel, thus speeding up data collection. In addition, multiple optical traps allow to stretch biological structures or soft biomaterials in more than one direction [87]. Also, with holographic optical tweezers it is easy to steer unequal amounts of laser power into the different optical traps. This enables to control the force exerted by each trapped bead individually. For example, it would be possible to exert gradients of forces on cells [111].

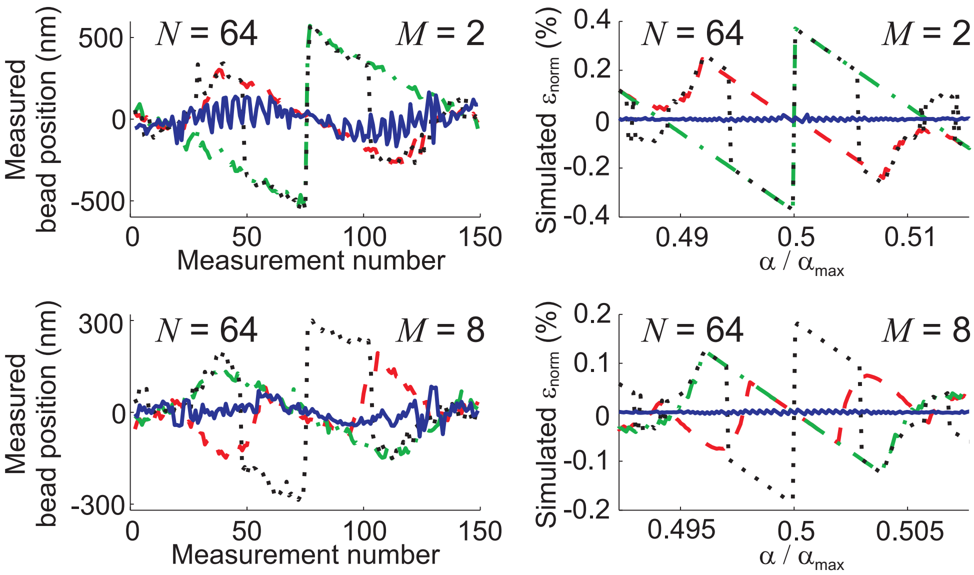

Figure 4.12: Measured deviation of the position of a 2.6 μm silica bead from the intended position using a high speed camera (left) and simulation of the normalized steering error (right) for steering in one dimension with number of pixels $N = 64$ and number of phase levels $M = 2$ (top) and $M = 8$ (bottom). In the experiments 4×4 SLM pixels where binned together to form larger effective pixels. Thus, 256×256 real SLM pixels were used in the experiment. Red dashed line: standard blazed grating going through $\varphi = 0$ at the leftmost pixel of the SLM; green dashed-dotted: standard blazed grating going through $\varphi = 0$ at the center pixel of the SLM; black dotted: blazed grating with the worst possible phase offset and blue solid: blazed grating with the optimal choice of phase offset for each individual trap position.

Chapter 5

The biological model system

All species are descended from a common ancestor and their fundamental properties have been conserved through evolution. Therefore, the study of one organism can contribute to the understanding of other organisms, ultimately allowing us to understand humans and human disease. However, some organisms are easier to study than others in a laboratory environment. The research community has therefore focused the efforts on a few species on different levels of complexity. Important model organisms that the biological community have chosen to focus on are [112, 113]:

Escherichia coli is a bacterium normally living in the gastrointestinal tract of humans and other vertebrates. Much of our knowledge on the fundamental mechanisms of life, such as DNA transcription and RNA translation, has come from studies of *E. coli*.

Saccharomyces cerevisiae is more commonly known as baker's yeast or brewer's yeast. This small single-celled fungus is the model organism representing a simple eucaryotic cell. Studies of yeast thus contribute to a better understanding of many of the basic mechanisms in eukaryotic cells, such as cell division.

Arabidopsis thaliana or wall cress, is the organism that has come to represent flowering plants. Genes found in this simple weed has counterparts in agricultural species. The insights gained from studies of *A. thaliana* are applicable to several crop plants as well as other plant species on Earth.

Caenorhabditis elegans is a nematode worm usually found in soil and was the first multicellular organism whose complete genome was sequenced. Its development from a fertilized egg cell into an adult worm is known in great detail. The worm has differentiated tissues including a nervous system. Approximately 70% of the human proteins have some counterpart in the worm, thus making the worm a useful model for many of the processes occurring in human bodies.

Drosphila melanogaster is a small fruit fly and is a favorite among developmental biologists and geneticists. Studies on *D. melanogaster* have contributed to the understanding of the genetics and development of multicellular animals. For example, studies of this fruit fly provided the definite proof that genes are carried on chromosomes [112]. Surprisingly many genes are similar to those in humans, and *D. melanogaster* has therefore come to serve as a model for human development and disease.

Mus musculus is a mouse and has since long been used as the organism representing mammals. Almost every human gene has an ortholog in the mouse, with similar DNA sequence and function. Inbred laboratory strains of *M. musculus* have been developed in order to conduct genetic experiments in genotypically uniform animals.

In my work I have been studying *S. cerevisiae*, being a robust and easily cultivated organism well suited for single cell studies. This organism and a specific signalling pathway that is relevant for my experiments are described in more detail below.

5.1 *Saccharomyces cerevisiae*

S. cerevisiae occurs naturally on plant material, like drying fruits. The yeast has a several thousands years long history of being used in the production of food and beverages. In the late 17th century Antonie van Leeuwenhoek studied wine sediments in his simple microscope. Although he most probably saw yeast cells, what he saw was believed to be nonliving catalysts. However, through studies of yeast in fermenting crushed grapes by Pasteur in the 19th century, it became clear that yeast was actually a living microorganism. Today yeast have important industrial applications, but advances in the understanding of the cellular physiology and the fact that it is easy to handle have led to its use also as a eukaryotic model organism.

Yeast share a number of properties with other eukaryotic cells, such as having a nucleus, containing the DNA packaged in chromosomes, and specific organelles like mitochondria, peroxisomes, endoplasmic reticulum

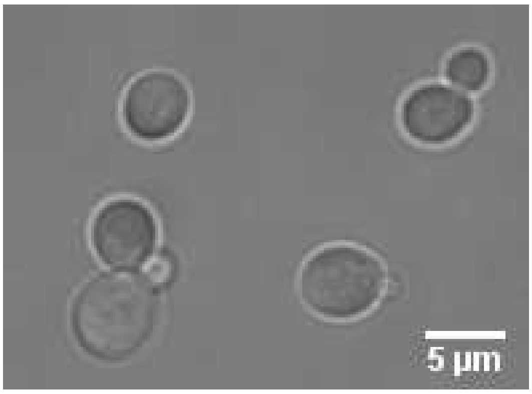

Figure 5.1: A brightfield image of baker's yeast, *S. cerevisiae*. The cells in the image are in various stages of the cell cycle.

and a Golgi complex. Several eukaryotic cell processes, such as chromosome replication, transcription and translation, cell division and intracellular signalling, can therefore be studied in yeast, despite being a simple unicellular organism. From an experimental point of view, yeast is convenient to work with since it is nonpathogenic, nonmotile, easy to cultivate in large populations and has a short generation time (about 90 minutes). It is also amenable to genetic and biochemical manipulation. The main disadvantage is its small cell size, which is a challenge in relation to light microscopy. A yeast cell is around 5-10 μm in size, which is only about one order of magnitude larger than the diffraction limit of light, see figure 5.1.

The genome of *S. cerevisiae* was the first eukaryotic genome to be fully sequenced [114]. This sequence is since 1996 available through a public database, the Saccharomyces Genome Database (www.yeastgenome.org), together with a wealth of information regarding the organism. The genome sequence has 12,068 kilobases defining roughly 6000 genes on 16 linear chromosomes. The *S. cerevisiae* genome is unusually compact with very short intergenic regions, even compared to other yeast species. The genes in yeast have few introns and the genetic redundancy is low, which facilitates the analysis of gene function [115]. Despite the large evolutionary distance between yeast and humans, many fundamental genetic and biochemical processes have been conserved between the two. In 1997, more than 30% of the protein encoding genes of yeast were predicted to have mammalian orthologs [116]. This number is probably an underestimate, since no mammalian genome was completely known at the time. Proteins from higher organisms may be expressed in yeast and perform tasks comparable to their yeast orthologs. For instance, it has been shown that yeast viability can be

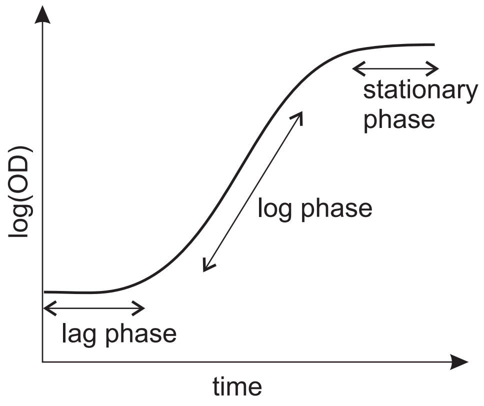

Figure 5.2: Illustration of yeast growth over time. In the lag phase the cells adjust to the new environment. Once they have adapted they reach exponential growth, which manifests itself as a straight line on a logarithmic scale of the optical density (OD). When all nutrients are consumed and waste products have accumulated, the growth rate declines and the cells go into a stationary phase.

restored by expression of mammalian proteins [117]. Information regarding human genes can thus be obtained by studying the yeast orthologs or by inserting the genes of interest into the yeast genome.

Yeast cells can be grown in liquid or solid media, that provide the energy and nutrients needed. The cells can also survive for long periods of time in frozen glycerol stocks. A common liquid medium for growing yeast cells is yeast peptone dextrose (YPD), which is a rich medium. However, this medium is highly autofluorescent, so for fluorescence imaging applications a synthetic minimal medium, such as yeast nitrogen base (YNB), might be a better choice. When inoculating a new yeast culture, the cells first need to adjust to the new environment. This phase is called the lag phase. As the cells have adapted to the medium they reach a stage where they grow and double at their maximum rate. Since they double at a constant rate, this stage is referred to as the logarithmic or the exponential phase. When all nutrients are consumed and waste products have accumulated, the growth rate declines and the cells go into a stationary phase. Experiments should preferably be conducted on cells residing in the logarithmic phase. A growth curve typically looks like that in figure 5.2.

Another advantage is that *S. cerevisiae* exist both as haploids and diploids, i.e., it can have one or two sets of chromosomes, thus enabling genetic selection and screening for rare mutations, either dominant or recessive [118]. In nature yeasts are diploid, but haploid strains can be maintained as stable cell cultures in a laboratory environment. Both haploid

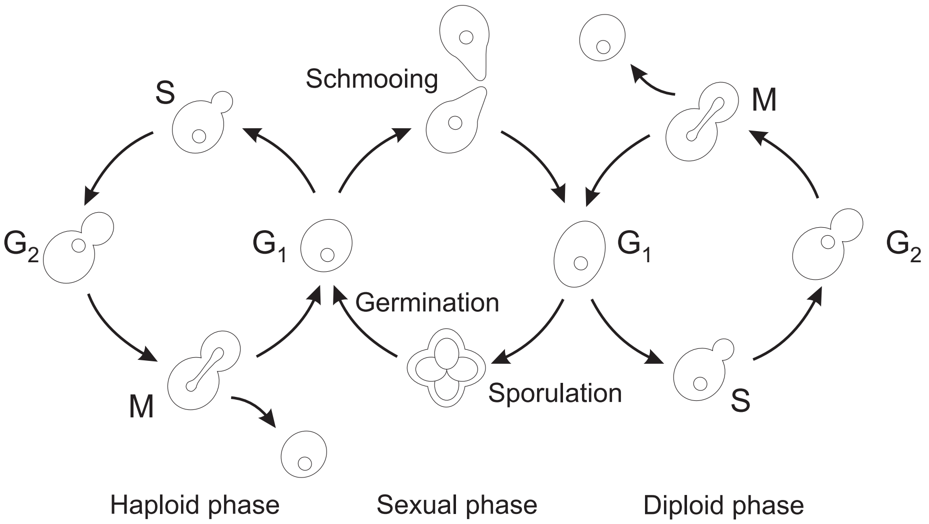

Figure 5.3: Illustration of the life cycle of budding yeast, *S. cerevisiae*. Adapted from [115].

and diploid yeast can reproduce vegetatively by budding, meaning that a mother cell buds to form a genetically identical daughter cell, see figure 5.3. Sexual reproduction takes place when two haploid cells of opposite mating type (**a** and α) are fused to form a diploid cell. Before this happens, the two haploid cells change shape which is called ”shmooing”. Under starvation the diploid cell can also undergo meiosis to form four haploid spores held together in an ascus sac. When given sufficient nutrients, the spores germinate and reproduce as haploid cells (two of mating type **a** and two of mating type α). As other eukaryotes, yeast cells age, which means that a mother cell can only give rise to a limited number of daughter cells.

During the budding cycle the morphology of the yeast cell changes, as illustrated in figure 5.3. In the G_1 phase, the cell is round and has no bud. In the S phase, a small bud starts to form, and the chromosomes are duplicated, forming pairs of sister chromatids. In the G2 phase, the bud grows and the nucleus is found in the bud neck between the mother and the daughter cell along the spindle pole axis. During mitosis (M) the sister chromatids are divided between the mother and the bud. Finally, the mother and the daughter cells are separated by cytokinesis. Eventually the daughter cell will grow to the size of the mother cell. Both cells are then ready to divide again. A scar on the cell surface of the mother cell as well as on the daughter cell will be left after cell division. The scar on the mother is referred to as the bud scar, while the scar on the daughter cell is referred to as the birth scar, see figure 5.4. Examples of yeast cells in various stages

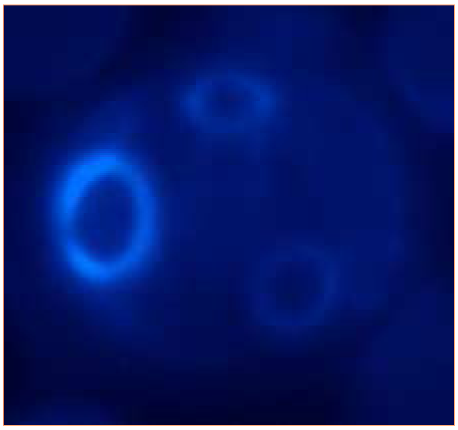

Figure 5.4: Fluorescence image of the birth and bud scars on a yeast cell. Courtesy of Hugo Aguilaniu.

of the cell cycle can be seen in figure 5.1, where dividing cells with different sizes of the bud are visible.

A further advantage of using *S. cerevisiae* in genetic research is that it can express heterologous genes either from an episomal plasmid or from chromosomal integration. Also, it is relatively simple to insert, delete or mutate almost any genomic sequence due to the presence of an efficient homologous recombination pathway. Of particular interest for the experiments presented within this thesis is the ability to incorporate reporter genes into the genome. Reporter genes are DNA sequences that encode proteins, such as fluorescent proteins, that can provide varying signals depending on the level of gene expression. The reporter gene sequence can either be fused to the gene of interest or inserted downstream from the promoter region, thus replacing the gene of interest.

Several proteins encoded in the genome are part of various cell signalling pathways governing cell behavior. A pathway describes how different proteins affects each other, often in a cascade, where each protein activates the next, in order to induce a certain response from the cell. Many signalling pathways are conserved between yeast and human, and therefore information regarding signalling pathways found in yeast is important for understanding the corresponding pathways in human.

The fusion of reporter genes to genes encoding relevant proteins in a signalling pathway allows one to follow, e.g., the spatial localization of the reporter gene product during environmental perturbations, as the external stimulus activates a receptor triggering a signalling cascade. Through the signalling pathway, the information regarding the external environment is translated into a cellular response, needed because of the changing conditions.

In this thesis, much of the work has been concerning three specific signalling pathways responding to changes in osmolarity of the extracellular medium, oxidative stress and the presence/absence of glucose as a carbon source. In these pathways the relevant kinase, transcription factor or repressor is tagged with GFP, and the translocation of these - Hog1, Yap1 and Mig1, respectively - in and out of the nucleus upon environmental changes are monitored. In addition, Msn2, a transcription factor of several genes in the response to a number of stress conditions, has been monitored for all types of environmental changes as a control. For the work performed in this thesis the high osmolarity glycerol (HOG) pathway has been most important, therefore this pathway is described in more detail in the next section.

5.1.1 The HOG signal transduction pathway

A fundamental question in cell and developmental biology is how cells sense and respond to their environment. They have to sense and distinguish different external stimuli, but also to turn the resulting signal into an appropriate response, in order to try to counteract or adapt to the changing environment.

The HOG pathway is an example of a family of signal transduction pathways referred to as mitogen activated protein (MAP) kinase pathways. MAP kinase pathways are well conserved from yeast to humans. Therefore, knowledge gained from studies on yeast should be applicable to MAP kinase signalling in all eukaryotes. These pathways are activated by external stimuli like the presence of growth factors or other stress conditions, and result in a cellular response. The extracellular signal is mediated by proteins in a cascade. Kinases are enzymes which catalyze binding of inorganic phosphate groups, e.g., from ATP, to target molecules. The core of a MAPK pathway consists of a MAP kinase, which acts on various target species, mostly transcription factors or cytosolic proteins. The MAPK becomes active due to phosphorylation by an upstream component - a kinase of the MAPK, therefore called MAPK kinase (MAPKK). The MAPKK in turn is activated by its respective upstream kinase - the MAPKK kinase (MAPKKK).

The HOG pathway is concerned with the water balance of the yeast cell. When the osmolarity of the extracellular medium is increased, water will flow out of the cell due to osmosis, causing the cell to shrink. When this happens, the HOG pathway is activated in order to counteract the external stress condition. As a result, the cell accumulates compatible solutes to balance the cellular osmotic pressure in order to regain its volume. For *S. cerevisiae* glycerol is a compatible solute. There are only four known mechanisms for the cell to increase its glycerol content: glycerol uptake from the environment via a membrane protein called Stl1, closure of the glycerol export channel Fps1, the production of glycerol, and Pfk2 activity, which stimulates glycolysis. The glycerol production is a direct result of the activation of the HOG pathway.

Normally the yeast cell has an intracellular osmotic pressure that is higher than the extracellular osmotic pressure. The difference between the two is compensated by a hydrostatic pressure, referred to as turgor pressure. This turgor pressure decreases if the cell is subjected to a medium with a higher osmolarity. More specifically, it has been suggested that the change in turgor pressure is proportional to the relative volume change of the cell [119]. It has also been proposed that the decrease in turgor pressure could be the signal that activates the HOG pathway [120]. To test this the turgor pressure and the HOG pathway activation should be measured experimentally.

The HOG pathway can be activated through two independent branches, named after the respective membrane proteins, Sln1 and Sho1. A simplified schematic of the HOG pathway is presented in figure 5.5. The Sln1 branch seems to be operating over a broader range of osmolarities than the Sho1 branch [121]. The two branches meet at the MAPKK Pbs2 that acts on the MAPK Hog1. In unstressed cells Hog1 proteins are evenly distributed throughout the cell, and are shown to cycle between cytoplasmic and nuclear compartments [122]. However, when Hog1 becomes phosphorylated by Pbs2 it accumulates in the nucleus [122], where it affects the expression of several genes, by controlling the activity of several transcriptional activators and repressors. One of the genes that are transcribed is *GPD1*, encoding the enzyme Gpd1 that catalyzes glycerol production.

The period and the amplitude of the HOG pathway activation (reflected by Hog1 phosphorylation) needs to be precisely controlled, since hyperactivation of the pathway may have detrimental effects for the whole cell, including cell death. Thus, the level of activated Hog1 needs to be precisely controlled. This control is based on the functioning of phosphatases - enzymes specialized in removing phosphate groups. Deactivation of the HOG pathway is performed mostly by the Hog1-specific phosphatase Ptp2 (predominantly found in the nucleus) and, to a lesser extent, by Ptp3 (cytoplasmic). However, there are also other phosphatases acting on Hog1 [123]. The existence of several phosphatases acting on the same MAP kinase, differing in their localization and specificity, allows precise temporal

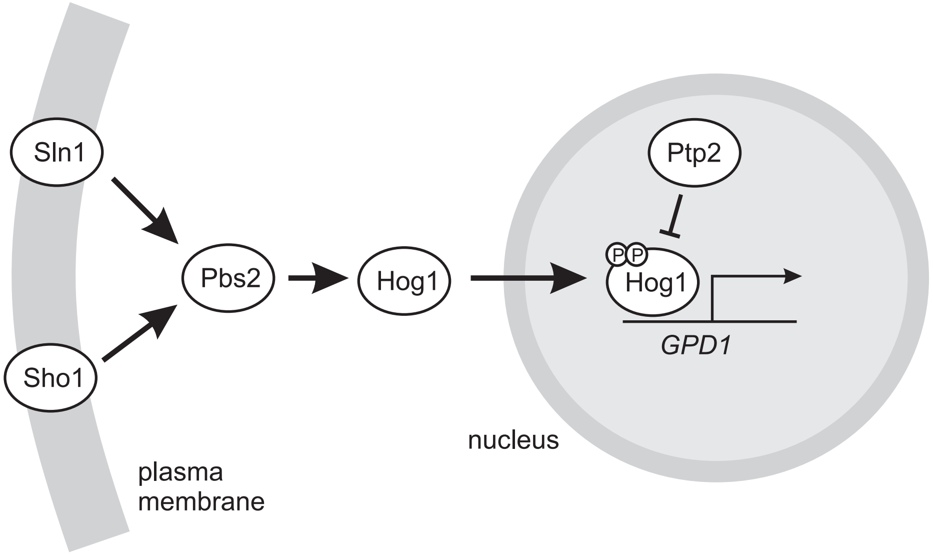

Figure 5.5: A simplified schematic of the HOG pathway. The Sln1 and Sho1 transmembrane proteins are activated upon increased osmolarity in the medium surrounding the cell. The two branches merge at the stage of Pbs2 that phosphorylates Hog1, which localizes to the nucleus, where it controls the activity of several transcription factors. Ptp2 dephosporylates Hog1, possibly facilitating the exportation of Hog1 out of the nucleus.

and spatial modulation of the kinase activity. It has been argued that the deactivation of the HOG pathway is mediated by glycerol accumulation, cell reswelling and increase in turgor pressure [124]. The Hog1 protein returns to the cytoplasm once the cell is adapted to the new environmental conditions or if the cell is returned to an iso-osmotic environment.

Even though the overall organization of the HOG pathway is well known, several questions are still unanswered [121]. What cellular mechanisms are used to detect changes in osmolarity? Why are there two independent branches in the HOG signalling pathway? How is the pathway activity downregulated? In addition, the transduction kinetics and *in vivo* reaction rates have only been roughly estimated [29]. Better experiments on a single cell level could hopefully help to answer some of these questions.

Chapter 6

Experiments & results

The goal behind most of my experiments carried out during my time as a PhD student has been to follow and quantify the behavior of single cells subjected to environmental changes. In this thesis two different experimental approaches are demonstrated, both combining optical tweezers and microfluidics in a fluorescence microscope. In the first approach a stationary concentration gradient is established and the optically trapped cells are moved across this gradient in order to achieve the environmental change. In the second approach the cells are instead positioned on the bottom of the microfluidic device, and the environmental change is accomplished by changing the relative flow rates in the inlets. In both approaches a combination of bright field and fluorescence microscopy is used to monitor the cellular response. Both systems also use high magnification and high NA microscope objectives to achieve a high spatial resolution, and depending on the types of images acquired a temporal resolution of sub-second time scales can be reached. Both designs allow precise and reversible environmental changes to be performed. After the addition of a certain stress substance it is therefore possible to repeatedly remove and add the substance. This is a feature that is hard to achieve with traditional techniques used in cell biology.

These two approaches are presented in this chapter together with examples of experimental results related to the study of cell signalling pathways in *S. cerevisiae* (sections 6.2 and 6.3). As pointed out in chapter 1, while the single cell information is highly interesting, it is still important to study a statistically relevant number of cells. To increase the throughput, holographic optical tweezers were introduced to the experimental setup used in the first approach for changing the environment, in order to study several cells simultaneously. However, this introduced a new problem, since cells

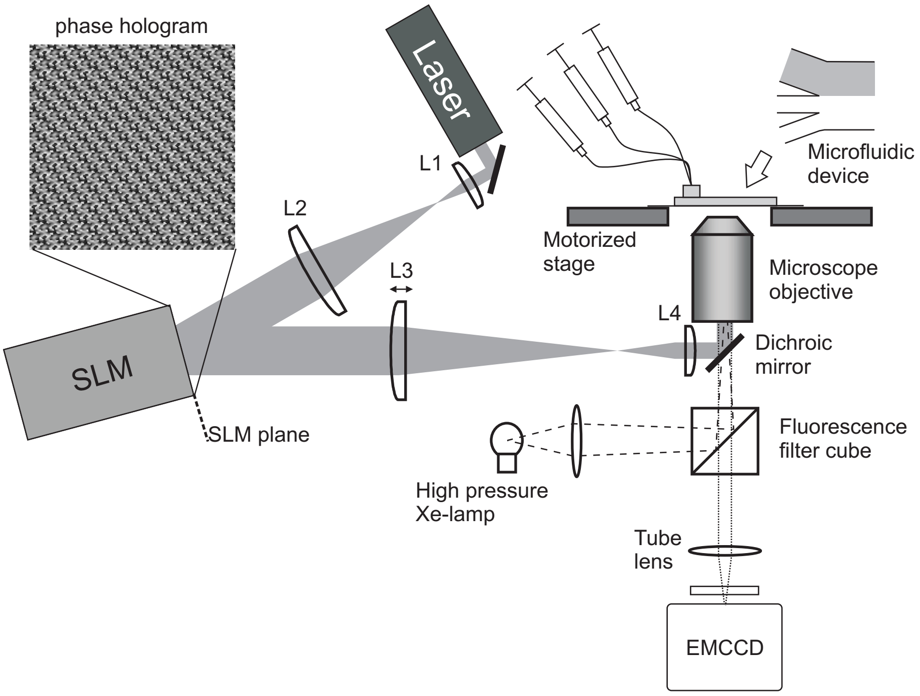

Figure 6.1: A schematic of the experimental setup used to perform the experiments presented in this chapter. The holographic optical tweezers are formed by expanding the laser beam to match the size of the SLM, then reduced and imaged onto the back aperture of the microscope objective via the dichroic mirror. The fluorescence imaging is performed with a Xe lamp as light source, appropriate filter cubes, and an EMCCD enabling imaging over long periods of time of weakly fluorescent samples. The cells are optically trapped within the microfluidic system, positioned on the motorized microscope stage. The flows in the microfluidic device are controlled by two independent syringe pumps.

align differently in the optical traps due to differences in size, shape and composition. In section 6.4 a solution on how to bring the interesting parts of the cells into a single image plane, using HOTs, is presented.

6.1 Experimental setup

During the last few years the experimental setup has undergone several changes. The setup as it looks today is schematically depicted in figure 6.1. The details regarding the setups used for specific projects are described in the corresponding papers. Also, appendix A summarizes the appended papers with a more technical focus than is provided in this chapter.

The setup is built around a Leica DMI6000B inverted epi-fluorescence microscope. The microscope has a motorized microscope stage and a motorized z focus. It has room for up to six different fluorescence filter cubes, and the fluorescence light is provided by a Xe lamp, fiber coupled to the microscope body. To image weak fluorescence from cells over long periods of time a 14 bit EMCCD camera is used.

The laser beam forming the holographic optical tweezers is introduced via a dichroic mirror situated between the microscope objective turret and the fluorescence filter cube cassette. The laser can supply 5 W of laser power, where the beam is linearly polarized and has a wavelength of 1070 nm, i.e., in the near infrared part of the spectrum. The design of the optical setup forming the holographic optical tweezers follows the principles outlined in sections 4.1.1 and 4.2.2, where a first telescope ($L1$ and $L2$) expands the laser beam to fill the SLM area, and the second telescope ($L3$ and $L4$) images the SLM onto the plane of the back aperture or back focal plane of the microscope objective. For our microscope objective, a 100× objective with a NA of 1.3, these two planes coincide. The SLM is an optically addressed parallel aligned nematic liquid crystal spatial light modulator. When only a single optical trap is needed, the SLM is not turned on and just acts as a mirror. To provide axial control of the trap when the SLM is not used, lens $L3$ is mounted on a motorized translation stage.

The pumps used to establish flows in the microfluidic systems are two syringe pumps capable of holding four syringes each, able to provide volumetric flow rates down to 1 nl/min. For the experiments presented in section 6.3, where the relative flow rates in the inlet channels of the microfluidic device are changed to establish an environmental change, the pumps are controlled from OpenLab, the same software as controls the microscope. OpenLab has an extension, called OpenLab Automator, that allows the user to program the image acquisition procedure in detail and to control any external equipment, such as the microfluidic pumps or the motorized translator on which lens $L3$ is mounted, via the serial ports of the computer. The hologram calculation, addressing of the SLM, camera and relevant parts of the microscope are controlled from LabVIEW for the experiments where HOTs are used.

6.2 Environmental changes - stationary flows & moving cells

The first version of this experimental platform (**PAPER I**) combined a single optical tweezers and a Y-shaped microfluidic system, like that simulated in figure 3.5. In one of the inlet channels the cells were introduced together with the medium in which they were cultured, and in the other inlet the medium containing the stress to which we wanted to expose the cells to was introduced. When these two channels were combined, a concentration gradient was formed due to the diffusive mixing of the two laminar flows. The steepness of this gradient depended on the diffusion coefficient of the stress substance, the flow rates and the distance downstream of the junction. In **PAPER I** the width of the concentration gradient was estimated from the analytical expression given by equation 3.13. In order to change the environment of a single cell, a cell in the flow was trapped with the optical tweezers and subsequently moved, using the programmed motorized microscope stage, in the transverse direction of the flow. The distance that the cell was moved was large enough to assure that the entire gradient region was passed, i.e, so that the concentration of the stress substance was zero at the starting position and that the desired concentration of the stress medium was reached in the end position.

Using this system we demonstrated that we could monitor the size of an optically trapped yeast cell, while moving the cell back and forth between the growth medium and a medium in addition containing 1 M of NaCl. The environmental change was accomplished in less than 0.2 s, thus enabling the study of fast processes, such as osmoregulation, happening in the cell upon environmental perturbations. When the yeast cell is exposed to a medium of higher osmolarity (e.g., a NaCl containing medium) the cell shrinks due to osmosis. As the cell is moved back to the initial medium the cell size increases again due to the inflow of water. The dynamics of the cell volume under osmotic stress is important for the understanding of the HOG pathway described in chapter 5. The size of the yeast cell was estimated from brightfield microscope images acquired at a frame rate of about 10 Hz. An example of a yeast cell subjected to an osmotic shock with this setup is shown in figure 6.2. Here the detected cell boundary, using image analysis, is marked with the red contour. The area contained within the boundary was then extrapolated to a volume assuming the cell to be a sphere.

In addition, we showed that we could follow intracellular processes *in vivo*, by monitoring the spatial distribution of GFP-tagged proteins upon

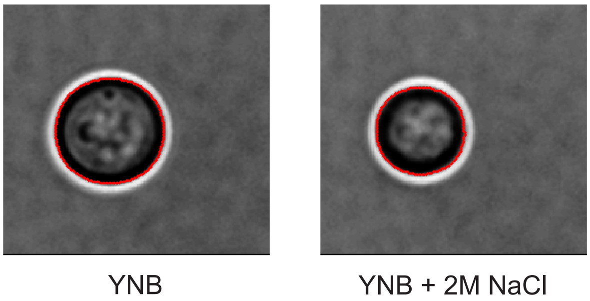

Figure 6.2: A yeast cell subjected to 2M NaCl, at start and after 11 s of stress. The red contour represents the detected cell area from the image analysis.

stress. In this case we monitored how the transcription factor Yap1-GFP was localized to the nucleus upon oxidative stress, and also how it was translocated out of the nucleus when the cell was moved back to pure growth medium. Just as it is important for the cell to activate appropriate signalling pathways to defend itself against stress, it is also important to down regulate the response when it is not needed anymore.

A disadvantage with the design of the microfluidic device described above was that the cells were introduced together with the pure growth medium, representing no stress. In reversible stress experiments, the trapped cell was therefore moved back to this flow, where other cells suspended in the medium could interfere with the measurement. In the worst case this resulted in that the trapped cell under investigation was lost. To avoid this problem, an extra inlet was added to the microfluidic device, as illustrated in figure 6.3. With this design, there is an extra channel, containing pure growth medium (YNB), between the cell channel and the stress channel. Thus, the cell flow is used only to collect the cell to be used in the experiment, which in turn is performed by moving the cell between the two other flow streams. The concentration distribution within such a device was modelled in **PAPER II**, where we demonstrated the use of the experimental approach for another signalling pathway in yeast, dealing with glucose starvation. Here, it was shown how the repressor Mig1-GFP was translocated into the nucleus when glucose became available.

The same design of the microfluidic device was also used for studies on the HOG pathway, by again exposing the cells to a medium with higher osmolarity (**PAPER III**). In figure 6.4 a budding yeast cell is trapped, where the Hog1-GFP protein becomes localized to the nucleus upon NaCl stress. Introduction of HOTs to the setup enabled simultaneous trapping of multiple cells, which speeded up data collection. Figure 6.5 shows bright field images and fluorescence images of four yeast cells, before stress, and after

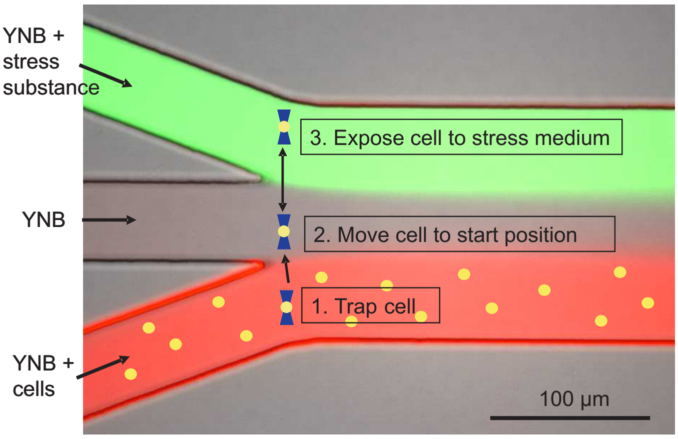

Figure 6.3: Principle of how to change the environment of a single optically trapped cell. A cell is trapped in the bottom channel (1), then moved to the middle channel (2), from where the experiment is started. The environment is changed by moving the cell between the two upper channels, where the upper channel typically contain a stress substance (3). In the microscope image of the microfluidic device fluorescein is added to the medium in the upper channel and rhodamine to the medium in the lower channel for visualization purposes.

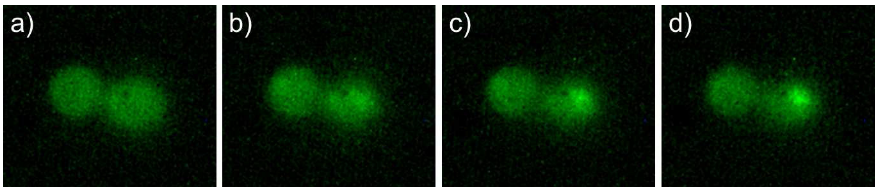

Figure 6.4: An optically trapped yeast cell exposed to an environment of 0.5 M NaCl. Image a) is taken just before the movement to the flow containing salt. Images b), c) and d) are taken after 1, 2 and 3 minutes of stress, respectively, and show the localization of Hog1-GFP to the nucleus.

40 s of 1 M NaCl stress. Again the shrinkage of the yeast cells upon osmotic stress can be seen. For this experiment, the cells had been stained with CalcoFluor White, a blue dye that binds to chitin, which is present in the cell wall, particularly abundant in the bud neck and bud scars. In a still standing medium, the largest array of yeast cells that I have trapped, contained over 100 cells.

From these two last figures a problem related to the subsequent quan-

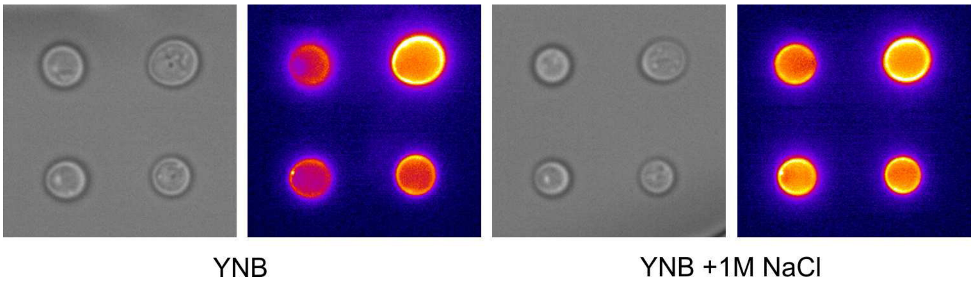

Figure 6.5: Four yeast cells trapped with HOT. Before (left two images) and after 40 s of 1M NaCl stress. The cell wall has been stained with CalcoFluor White, which is shown in the fluorescence images.

tification of the images can be noted; only one of the cells has the nucleus in the imaged plane in figure 6.4 and the four yeast cells in figure 6.5 are not all perfectly in focus. For example, the yeast cell up to the left is more out of focus than the other three. This is a consequence of the cells being trapped in a planar array of optical traps. The cellular organelle of interest can be made to coincide with the image plane using different approaches. One solution is to acquire an axial stack of images, where, if the spacing between the images in the stack is appropriately chosen, each cell or organelle will be in focus in one of the images in the stack. For trapped cells, such stacking can be obtained by translating the cells through the image plane, e.g., by changing the divergence of the laser beam by moving lens L3 in the setup presented in figure 6.1 or by adding a lens function to the hologram displayed on the SLM. For cells positioned on a surface where a high spatial resolution is desired (as in section 6.3), axial stacking is used to collect all the interesting information, such as nuclear localization of proteins. This is a consequence of a high spatial resolution requiring a microscope objective with a high NA, and consequently shorter depth-of-focus. Alternatively, if the cells are trapped with HOT, the 3D manipulation possibilities of HOT can be used to force the feature of interest (e.g., the nucleus) of each cell into a single image plane. This procedure also have the advantage of reducing the problem of photobleaching, as demonstrated in section 6.4.

6.3 Environmental changes - moving flows & stationary cells

A parallel approach for achieving environmental changes of several cells simultaneously is presented in **PAPER VI** and in this section. **PAPER VI**

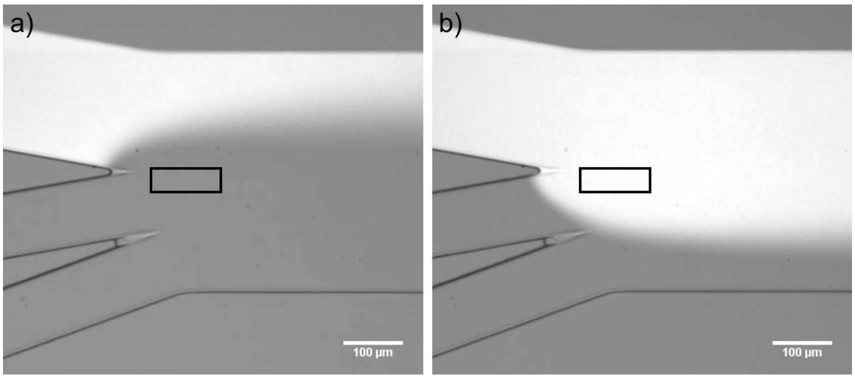

Figure 6.6: Fluorescence images overlayed on bright field images, illustrating the experiment principle. a) In flow configuration 1, representing no stress, the cells are positioned within the measurement area (black rectangle). The flow rates are (from top to bottom) 40, 80 and 80 nl/min, respectively, for the three inlet channels. b) Changing the flow rates to flow configuration 2 (480, 40 and 40 nl/min, respectively) accomplishes the environmental change within the measurement area.

demonstrates the system for the glucose signalling pathway, while the results presented in this section are related to studies of the HOG pathway. In addition, the system was used to acquire data for **PAPER VII**, where the volume change upon osmotic stress was related to the loss of turgor pressure and HOG pathway activation.

The microfluidic device used for these experiments contain three inlet channels, as illustrated in the microscope images in figure 6.6, where fluorescein has been added to the medium in the upper channel to represent the stress substance (flows are from left to right). Again cells are introduced in the lower channel, and a neutral medium is introduced in the middle channel. Initially the flow rates are higher in the two lower channels, whose inlets are connected to two syringes controlled by the same pump, and lower in the upper channel which is connected to a second pump. In this configuration representing no stress (in the following referred to as flow configuration 1) the cells are positioned in a measurement region, indicated by the black rectangle, using the optical tweezers (see below). Once the cells are positioned the experiment is started, in which bright field and/or fluorescence images are acquired in the desired axial planes at the desired time intervals. At the start of the experiment the environment is changed, which is accomplished by increasing the flow rate in the upper channel and decreasing it in the two lower channels (referred to as flow configuration 2).

To quantify the speed of the environmental change fluorescence images

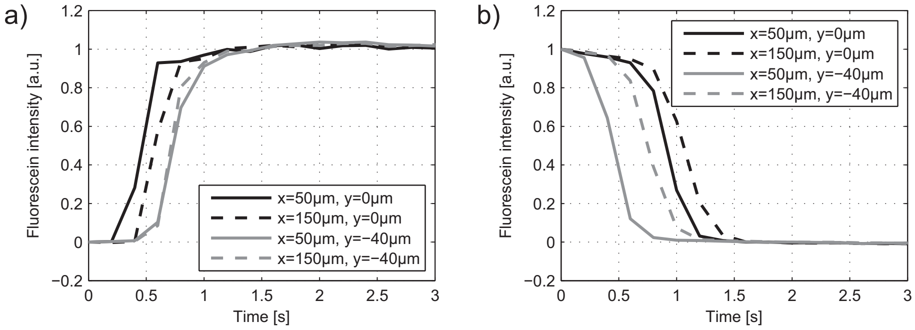

Figure 6.7: Environmental switching a) from flow configuration 1 to 2, b) from flow configuration 2 to 1. The four curves represents the edges of the measurement region.

were recorded after the pump settings were changed from flow configuration 1 to 2, figure 6.7a), and back, figure 6.7b). In four corner positions of a rectangle, much larger than the measurement region used in the cell experiments, the fluorescein concentrations were extracted from the sequence of microscope images. As seen in figure 6.7 the environmental change is accomplished in less than 2 s both for addition and removal of stress (image acquisition was started directly after the pump settings were changed). The coordinate system is set with origo at the junction where the two upper channels meet, where x points in the downstream direction and y points in the direction transverse to the flow, with $+y$ pointing towards the stress channel (upward in the images in figure 6.6). $z = 0$ corresponds to the bottom of the device.

Again, to further understand the concentration distribution within the device, it was modelled as described in chapter 3. This becomes even more important for this design, since the one dimensional analytical expression in equation 3.13 cannot be used, because the flow rates are different in the two channels merging at the junction. In addition, the cells are positioned at the bottom of the device where the mixing of the two media is largest, since the flow rates are low due to the no-slip boundary condition. Shown in figure 6.8a) are a few concentration profiles, at the bottom of the device, extracted from such a simulation, two curves (representing the two flow configurations) for each downstream distance. Here the stress medium is another osmoticum, sorbitol. As can be concluded from the figure, there is a measurement window (y coordinates for a number of downstream distances), where the concentration is 0 in flow configuration 1 and the intended concentration in flow configuration 2. From the simulations

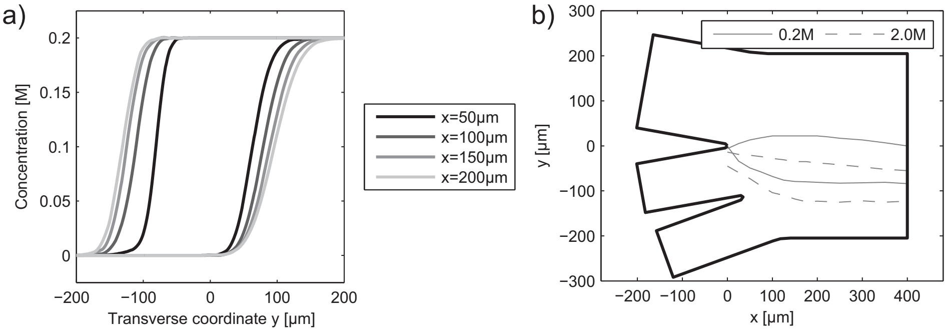

Figure 6.8: Simulation of sorbitol concentrations within the microfluidic device. a) Concentration profiles downstream of the junction when 0.2 M sorbitol has been added to the medium in the upper channel. The concentration profiles are at the bottom of the device ($z = 0$). b) The influence of the viscosity on the position of the measurement area within the microfluidic device. The lines indicate the measurement areas for two different sorbitol concentrations, 0.2 M and 2.0 M, respectively. For each concentration the upper line represent the position at no stress (flow configuration 1) where the concentration is 0.5% of the final intended concentration, while the lower line represents the position of 99.5% of the stress concentration (flow configuration 2).

the "edges" of the possible measurement region were found for a number of downstream distances by looking at the positions where the concentration profiles in flow configuration 1 reached 0.5% of the magnitude of the intended concentration change. Correspondingly, the opposite edges were found by looking at the coordinates where the concentration dropped to 99.5% of the desired concentration in flow configuration 2. The position of the measurement region is dependent on the sorbitol concentration, since the higher the concentration is, the more viscous is the sorbitol containing medium. This is illustrated for two concentrations, one low (0.2 M) and one high concentration (2 M) in figure 6.8b), where the theoretical measurement areas are shown. Here, the initial concentration is at most 0.5% of the intended final concentration and the concentration when stress is added is at least 99.5% of the intended concentration. At a downstream distance of $x = 100$ μm the y positions of the edges of the measurement region are plotted in more detail as a function of the concentration of sorbitol in the upper channel in figure 6.9, illustrating the concentration dependence of the measurement area position.

The cells were positioned within the measurement region using optical tweezers in combination with the motorized microscope stage and motorized microscope objective holder. The positioning was automated with a script,

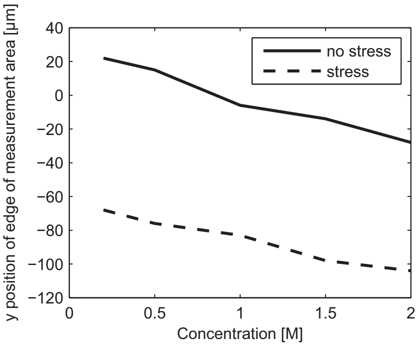

Figure 6.9: Concentration dependence of the position of the measurement area in the y direction at $x = 100$ μm for a few different sorbitol concentrations. In flow configuration 1 (no stress) all y coordinates below the ones indicated by the solid line have a concentration at most 0.5% of the intended final concentration, while in flow configuration 2, all y coordinates above the dashed line have at least 99.5% of the desired concentration. Thus the cells should be positioned between these two lines.

where the user specifies the (x, y) coordinates of upper left corner of the measurement region as well as the desired number of cells in the x and y directions and the spacing between the cells in the two directions. To define the coordinate system origo needs to be specified by the user by focusing the optical trap on the bottom of the microfluidic device at the point where the two upper channels meet. In addition, the user must choose a position within the device for the collection of cells. The automated procedure allows for repeatability of experiments, since for identical experiments the cells can always be positioned at the same coordinates relative to the junction. The program for positioning the cells allows the user to approve of the trapped cell before it is positioned in the measurement region. This makes it possible to discard cells that do not look healthy or clusters of cells that would anyway be hard to analyze in the subsequent image analysis. In addition, it allows the user to perform the experiments only on a specific category of cells, e.g., budding or non-budding cells, if desired. With this procedure the cell is typically kept for $2-3$ s in the optical trap, which was shown to be well below harmful laser exposure in **PAPER VI**. The use of the optical tweezers for positioning of cells has the advantage that the density of cells in the measurement region is easily controlled, which is beneficial from an image analysis point of view. In addition, the number of cells in each experiment can be kept nearly constant. The device is treated with a solution of Concanavalin A for one hour before the experiment to allow

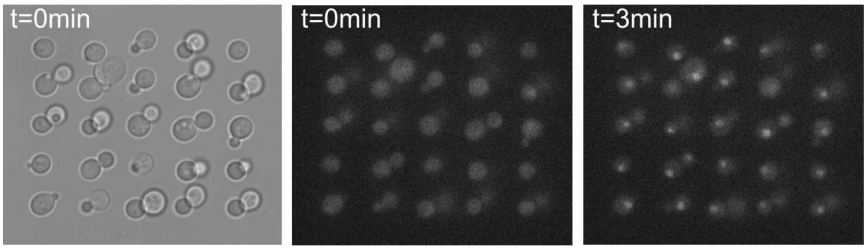

Figure 6.10: Experiment on Msn2-GFP expressing yeast cells. Initially (time $t = 0$ min) the cells are not stressed, which is indicated by the absence of Msn2-GFP accumulation. However, upon stress (0.25 M) Msn2-GFP localizes to the nuclei (image shown at $t = 3$ min). Also note the regular array of cells, which is possible thanks ot the automated positioning of cells in the measurement region using the optical tweezers and the motorized microscope stage.

the cells to attach to the bottom surface of the microfluidic device (a cover glass).

The system was tested on yeast cells expressing Msn2-GFP, see figure 6.10, to verify that the cells are not stressed at the start of the experiment. Msn2 is a transcription factor for several stress-responding genes, and localizes to the nucleus as soon as the cell is stressed. The cells showed no localization of Msn2-GFP at the start of the experiment, indicating that the positioning procedure does not induce any significant stress response, as well as indicating that the concentration distribution in the device is as intended, i.e., no stress is present in the measurement region at the start of the experiment. However, upon addition of sorbitol (in this case 0.25 M) the Msn2-GFP localized to the nuclei of the cells, indicating that the environmental change worked as intended.

In figure 6.10 a nuclear localization of proteins is not visible in all cells. This is a typical result of the nuclei being distributed over a number of axial coordinates due to the spatial extent of the yeast cells and the short depth of focus of the microscope objective. This necessitates the acquisition of axial stacks of images at each point in time. An example of the distribution of nuclei over several image planes is illustrated in figure 6.11. This histogram is based on one time point in an experiment where yeast cells expressing Hog1-GFP were repeatedly exposed to a medium containing 0.8 M sorbitol. The sorbitol medium was added at time $t = 0$ min and removed at $t = 5$ min. Then it was added again at $t = 10$ min. In total the medium was switched back and forth three times. Stacks of images of cells positioned in an array as in figure 6.10 were acquired every 30 s during 30 min. Images of a budding cell extracted from this sequence is shown in figure 6.12. As

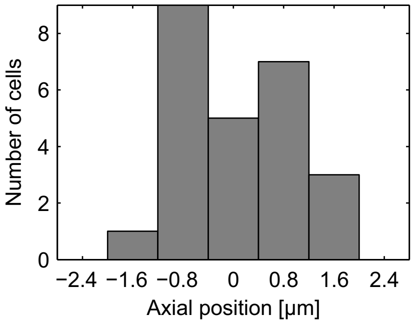

Figure 6.11: A histogram showing the distribution of nuclei from 25 different cells over several planes in an axial stack of fluorescence images.

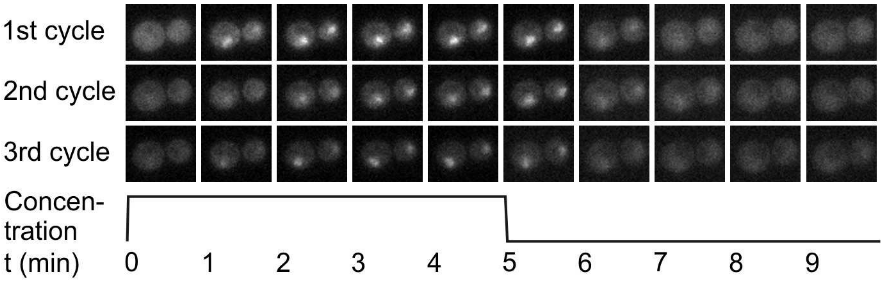

Figure 6.12: The same budding cell exposed to 3 cycles of 0.8 M sorbitol stress. Sorbitol is added at $t = 0$ min and removed at $t = 5$ min, and then added again at $t = 10$ min, starting a new stress cycle.

can be seen in this figure, the Hog1-GFP becomes localized to the nuclei when the osmolarity of the surrounding medium is increased, and when the stress is removed the Hog1-GFP returns to the cytosol.

A simple measure of the degree of nuclearization of Hog1 proteins is the average GFP intensity within the nucleus as a function of time, which is shown in figure 6.13a). However, simply using the average nuclear intensity is problematic for several reasons: Firstly, during long imaging time series the signal is photobleached, which can be seen as a decrease of intensity for consecutive stress cycles. Secondly, it does not allow cells with different expression levels to be directly compared. Instead, using a ratiometric quantity can compensate for these problems to a large extent and we chose to use the ratio between the average nuclear intensity and the average cytosolic intensity

$$R = \frac{\text{average intensity in nucleus}}{\text{average intensity in cytosol}}, \tag{6.1}$$

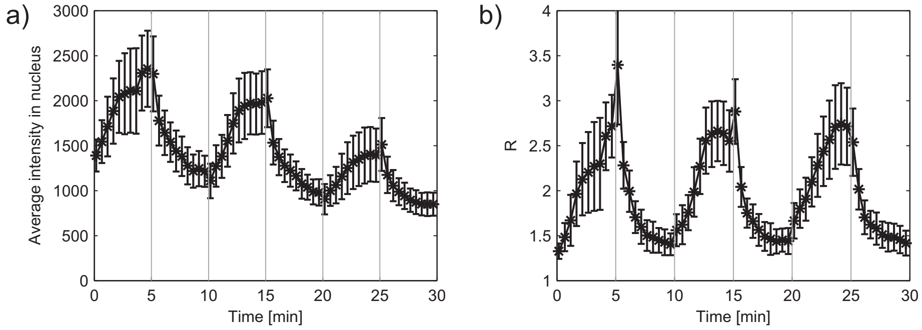

Figure 6.13: Hog1-GFP yeast cells stressed with 0.8 M sorbitol. Images of a budding cell from this experiment are shown in figure 6.13. a) Average GFP intensity in the nuclei as a function of time. The intensity for each cell is chosen from the axial plane containing maximum average intensity within a circular region 8 pixels in diameter (roughly corresponding to the expected size of the nucleus). The value represent the mean and standard deviation of the cells found in the image. b) The same data, but here the nuclear intensities are normalized to the median GFP intensities within the cells.

where the autofluorescent background has been subtracted from the average intensities. It should be noted that even this measure might be problematic for the specific case of osmotic stress, because of the shrinkage of the cell, which increases the density of fluorescent molecules and hence the intensities in the image. However, this is not considered further within this thesis. For the analysis the images needs to be segmented correctly to determine the areas corresponding to the cytosol and the nucleus, respectively. In addition, the analysis program should be able to separate a budding cell into two. As a first step I divided the image into square ROIs containing one (potentially budding) cell each. From each ROI and time point the measurements were performed in the axial plane where the average intensity found within a disc-shaped region, roughly corresponding to the expected size of the nucleus, was maximized. This average nuclear intensity is plotted in figure 6.13a), where the value given at each time point is the average of all cells (ROIs) and the error bars represent the standard deviation. The median intensity of the thresholded image of the cell was used to estimate the cytosolic intensity. The resulting R is shown in figure 6.13b), again represented by the mean and standard deviation of all cells (ROIs). The cells show a large heterogeneity in the response, i.e they respond with very different magnitudes, which can be seen from the large standard deviations in relation to the mean values. On the other hand, it seems like the kinetics and magnitude of the response is similar for the different stress cycles.

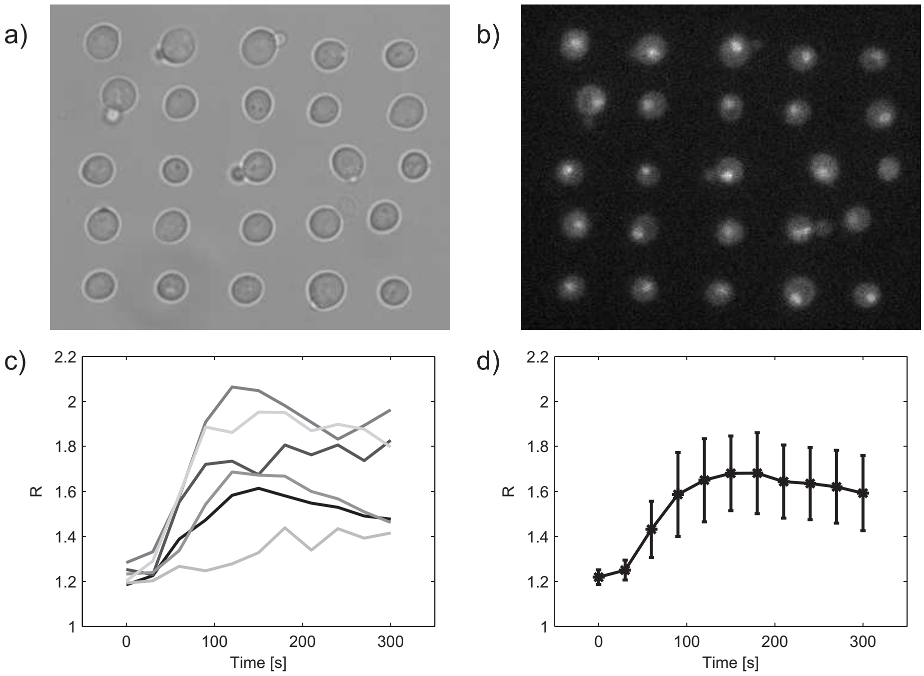

Figure 6.14: Yeast cells expressing Hog1-GFP subjected to an environmental change of 0.2 M NaCl at time $t = 0$ min (starting from YNB). a) Bright field image at $t = 0$ min, b) GFP image $t = 3$ min. c) Nuclearization, R, of Hog1-GFP as a function of time for a few cells selected from the images. d) Average R with error bars representing the standard deviation for all cells found in the images.

In a related experiment Hog1-GFP cells were exposed to a range of concentrations of NaCl. NaCl diffuses relatively fast, thus broadening the concentration gradients within the microfluidic device. For reversible stress experiments this could present a problem with the above microfluidic design, since the possible measurement region becomes narrower, unless the flow rates are increased. However, for the specific research questions behind this project one change of environmental condition was sufficient. Thus, the measurement area was chosen to make sure that the cells were not stressed at the start of the experiment (where the Hog-GFP signal could serve as a control), and instead the pump controlling the flow in the two lower channels was turned off at time $t = 0$ while the flow in the stress channel was increased to more than twice the flow rate used in the above experiments where sorbitol was used as a stress agent. An example from these experiments is shown in figure 6.14. Figure 6.14a) is a bright field image of the yeast cells at time $t = 0$. This image also indicates the possibility of choosing a specific cell type for the experiments. Here non-budding cells or cells only having a small bud were selected for the experiment. A GFP image taken from the axial stack at $t = 3$ min is shown in figure 6.14b). Here the nuclearization of Hog1-GFP upon stress is visible. To quantify the degree of nuclear localization a similar analysis was performed as the one in figure 6.13b). As an example a few single cell traces are shown in figure 6.14c), while the averages and standard deviations of the response of all cells are shown over time in figure 6.14d).

The same analysis was performed for all data sets corresponding to the different concentrations used, where the mean response is plotted in figure 6.15. As can be concluded from the analysis of the fluorescence images, the response is very different for the different concentrations. For low stresses (e.g., 0.05 M and 0.1 M) the response (i.e., the nuclear localization of Hog1-GFP) is low and starts to be down regulated already within the measured time frame of 5 min, as seen by the decreasing R. For concentrations up to about 0.3 M the magnitude of the response seems to increase, while the response has roughly the same magnitude for concentrations in the range 0.3 M - 0.6 M. For higher concentrations the magnitude of the response is decreased within the measured time interval. The measured R values at $t = 3$ min are plotted as a function of concentration in figure 6.16a), summarizing these findings. In addition, we could also note that the cell-to-cell variation, i.e., noise, in the response seemed to increase with increasing stress concentration, at least for stress concentrations above 0.6 M NaCl, as illustrated in figure 6.16b). Here, the standard deviation of the response at $t = 3$ min is normalized to the magnitude of the response, defined as the response at $t = 3$ min minus the response at $t = 0$ min. The seemingly large cell-to-cell variation at 0.05 M is a consequence of the cells hardly responding at all at this low concentration, c.f. figure 6.15.

From brightfield images taken during these experiments we could also estimate the volume of the yeast cells, by measuring the area and extrapolating this area to a volume assuming the cell to be a sphere. The relative volume after stress, defined as the volume after 90 s of NaCl stress divided by the volume before the stress, is shown in figure 6.17. On average 18 cells were segmented correctly per concentration by the analysis program used, CellID [125]. The mean relative volume is shown in the plot, where error bars represent the standard deviation between cells. This data was used to estimate parameters on membrane elasticity and turgor pressure via a mathematical model of the yeast cell shrinking in **PAPER VII**. In addition, for stresses up to 0.6 M NaCl the loss of turgor pressure could be directly linked to HOG pathway activation, c.f. figure 6.16a).

A difficulty with the image analysis presented above was to define the intensity in the nucleus when the cells were not stressed, since it is hard

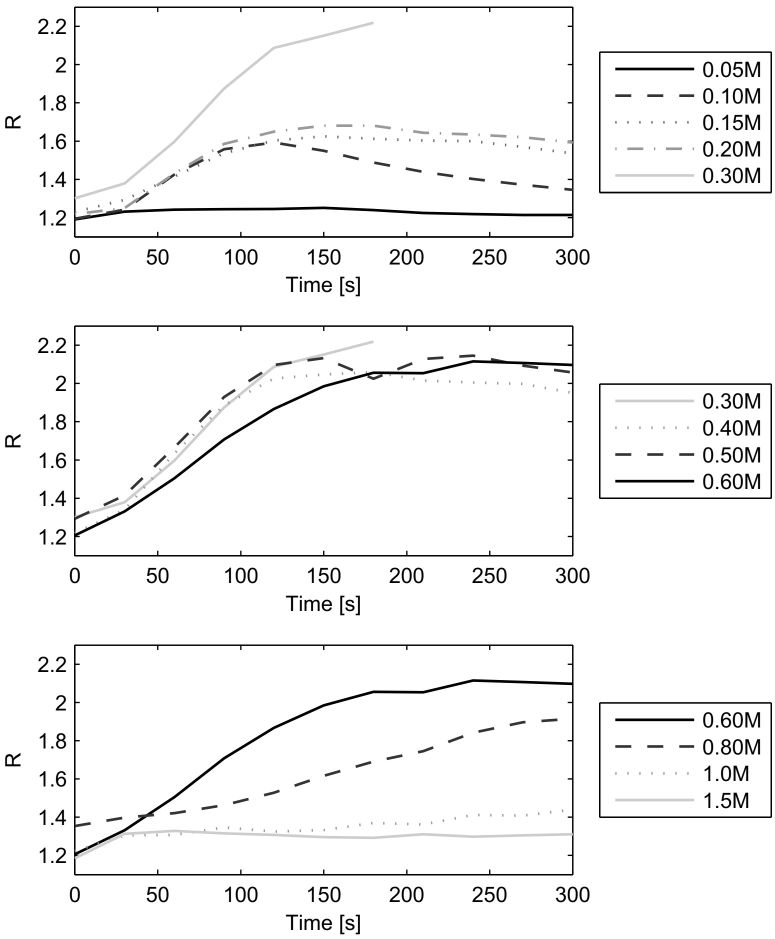

Figure 6.15: Nuclearization, R, of Hog1-GFP in yeast cells subjected to osmotic shocks of different concentrations of NaCl at time $t = 0$ s. The data is divided into several graphs for clarity.

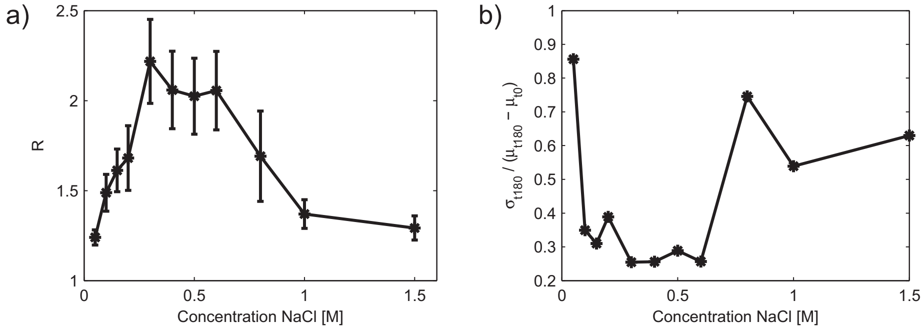

Figure 6.16: a) Degree of nuclearization after 3 min of NaCl stress. b) The cell-to-cell variation after 3 min (180 s) of NaCl stress seems to increase with increasing stress concentration. The variation is defined as the standard deviation divided by the difference between the magnitude of the response after 3 min minus the magnitude of the response at time zero.

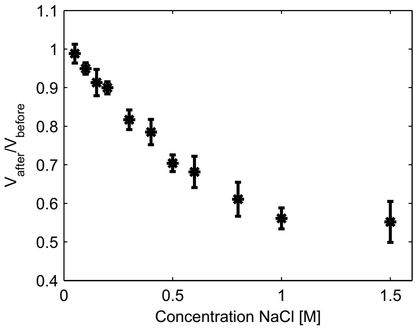

Figure 6.17: Estimated relative volume of yeast cells subjected to osmotic shocks of NaCl. The presented values and error bars represent the mean and standard deviations of the cells for a certain concentration.

to determine where the nucleus is when no nuclearization of proteins is present. In the analysis, the nuclear intensity was defined to be the highest intensity found within a region corresponding to size of the nucleus, regardless of whether the cells were stressed or not. To simplify the analysis of the GFP localization, we have recently tagged a protein localized to the nucleus, Nrd1, with mCherry that fluoresce in the red part of the spectrum. An image of this strain, expressing both Hog1-GFP and Nrd1-mCherry, is shown in figure 6.18.

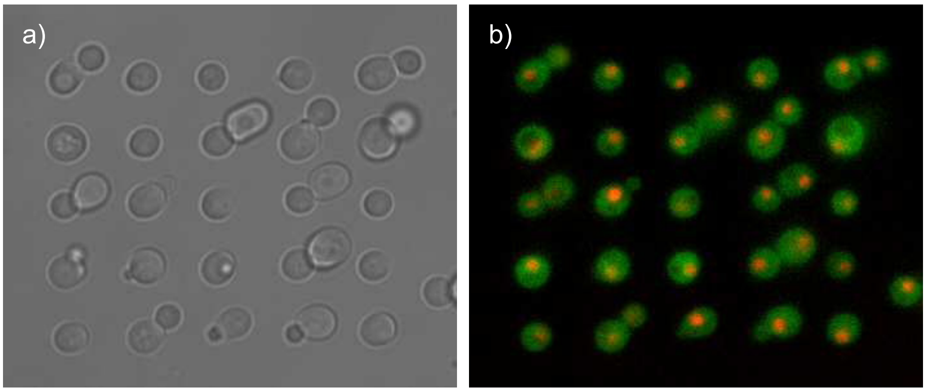

Figure 6.18: To help determine where the nuclei are when the cells are not stressed, i.e. at the start of the experiment, a complementary fluorescent protein can be used to stain the nuclei. a) Brightfield image and b) fluorescence image where the Hog1-GFP image (green) and Nrd1-mCherry image (red) are overlaid.

6.4 Holographic Optical Tweezers

In the experiments described in section 6.2 holographic optical tweezers were introduced to enable several cells to be studied in parallel. However, cells will align differently in the traps due to differences in size, shape, composition *etc.* As a result, cells optically trapped in a 2D array will not be in focus in a single image plane simultaneously. Although a cell is present in the image, the different appearances between cells might be problematic for the correct quantification of the size of the cells, and for smaller organelles like the nucleus it might present even more of a problem. In the worst case the nucleus will be completely out-of-focus, and an existing nuclear localization of proteins will not be visible in the image. However, also when the nucleus is imaged slightly out-of-focus and a nuclear localization can be seen it can present a problem, since not the full response is measured. As discussed previously, one solution to this problem is to acquire an axial stack of images, where the spacing between the images in the stack is fine enough to assure that the correct response is measured. However, for cells trapped with holographic optical tweezers, the 3D manipulation possibilities can be used to bring the nuclei of all cells into a single image plane. A procedure linking image analysis to hologram calculation in order to automate the focusing of nuclei or cells was demonstrated in **PAPER V**.

In this paper yeast cells expressing Hog1-GFP, stressed with 1M sorbitol, were trapped in an HOTs array. This array was translated through the image plane of the microscope objective by altering the divergence of the

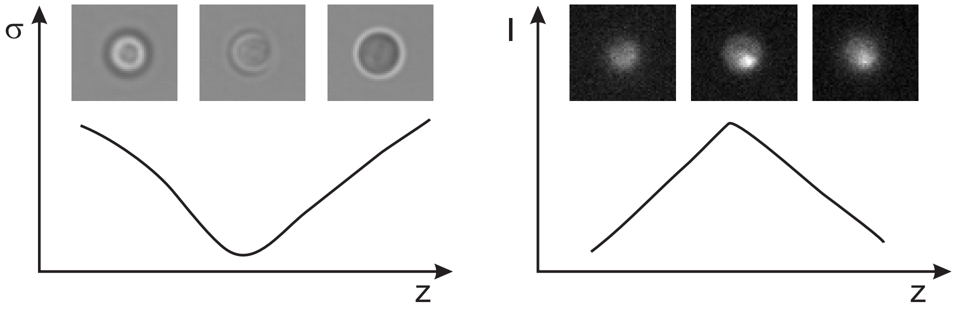

Figure 6.19: Image analysis can be used to define the focus plane for a cell in an axial stack of images. a) A brightfield image of a cell that is in focus has minimum standard deviation, σ. b) The fluorescence image of a cell with nuclear localization of GFP-tagged proteins has a maximum intensity, I, within a region of the size of the nucleus in the in-focus image.

laser beam via a sequence of holograms displayed on the SLM, in order to acquire an axial stack of images. For each cell the images in the stack were analyzed to find the correct focus plane for that cell. The corresponding axial coordinates for all cells were then returned to the hologram generation program, which calculated and displayed a new hologram representing an optical trapping pattern where the axial position of each cell had been individually optimized to get the feature of interest into focus. Two different optimization schemes were implemented: one to optimize the position of the cell based on brightfield images, and the other one based on fluorescence images where the nuclei were brought into focus. The axial coordinate of the optical trap where a cell was in focus was determined as the coordinate representing the brightfield image with minimum standard deviation of the pixel intensities. Similarly, a nucleus was determined to be in focus in the image with maximum pixel intensities within a disc-shaped region corresponding to the approximate size of the nucleus. This is illustrated in figure 6.19.

The result of such an optimization of the axial positions of cells having a nuclear localization of GFP-tagged proteins is shown in figure 6.20. In figure 6.20a) the single image plane having the largest number of nuclei in focus is shown, which is the plane to use if only a two-dimensional array of optical traps can be used. However, figure 6.20b) shows an image taken after the axial coordinates of the individual traps have been optimized, allowing all nuclei to be simultaneously in focus in the same image.

In these experiments the signal of interest, i.e., Hog1-GFP localized to the nuclei in stressed cells, was used to optimize the axial positions of the individual yeast cells. However, the cells do not always have a nuclear

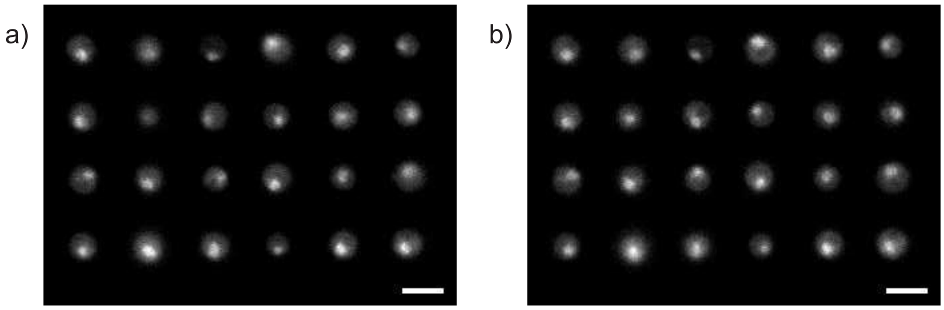

Figure 6.20: Yeast cells having a nuclear localization of GFP proteins trapped in a HOTs array. a) The image that has the largest number of nuclei in focus from an axial stack of images. For each image in the stack all optical traps were in a single plane. As seen, not all cells have their nucleus in focus. b) By individually adjusting the axial position of each optically trapped cell, which is possible using HOTs, the nuclei of all cells can be brought into a single image plane. Scale bar 5 μm.

localization of proteins at the start of the experiment, as in the experiments presented in section 6.2. The axial optimization of the optical traps could instead be performed using a second fluorescent protein, tagged to a nuclear protein, with a different spectral window, e.g., mCherry. This would also have the benefit of minimizing any extra exposure of the fluorescence signal of interest (in this case GFP) which could lead to photobleaching. However, a practical limitation for implementing this optimization procedure for cells trapped with holographic optical tweezers in a flow is the slow update rate of nematic liquid crystal based SLMs. The effects of the hologram update on particles trapped in a flow were investigated in **PAPER IV**. In a high flow, the temporary weakening of the optical traps while the hologram is changed could in the worst case lead to that the trapped cells are lost. To avoid this, faster SLMs or algorithms capable of minimizing the weakening of the traps are needed.

Taking the quantification of nuclearization of proteins as an example, the optimization of the optical trapping pattern has the benefit that all information of interest can be obtained from a single image. Thus, at each point in time, only a single image needs to be acquired rather than an entire axial stack. This has the advantage that photobleaching of fluorescent proteins becomes less of a problem, as illustrated in figure 6.21. In total this procedure allows more relevant images, i.e., images containing useful information, to be taken, either increasing the time resolution or making it possible to study the cells over even longer periods of time.

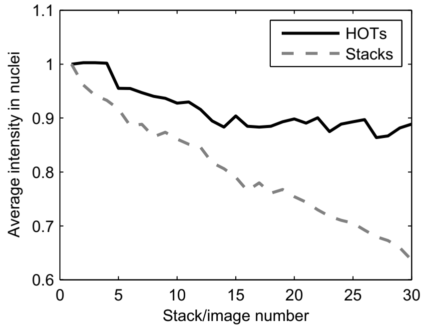

Figure 6.21: A comparison of the average nuclear intensities measured from microscope images, like the ones in figure 6.20, over time if taking only one optimized image (solid black) or if acquiring entire axial stacks of images (dashed gray) at each time point (13 images were acquired per stack). The nuclear intensities are normalized to one for the first frame. Photobleaching is strongly reduced when only one image, containing all relevant information, needs to be taken at each time point.

Chapter 7

Conclusions

I have demonstrated how optical tweezers, microfluidics and fluorescence microscopy can be combined in order to collect data on the behavior of single cells subjected to environmental changes. Two main approaches for achieving the environmental changes were presented, one where the cells are moved relative a stationary flow, and one where the cells are stationary and the flows are changed. Both approaches allow reversible environmental changes to be performed and the cellular response can be followed with a combination of brightfield and fluorescence microscopy with high spatial resolution. The approach with stationary flows achieves environmental changes faster than the approach using dynamic flows. However, dynamic flows facilitates the study of several cells in parallel. Thus, the first approach is better suited for experiments requiring a fast environmental change and for studies of fast processes in the cells, while the second approach is preferred in studies over longer periods of time where the temporal resolution is not that crucial and where statistically relevant data are more relevant. The experimental approaches were verified through studies of different signalling pathways in yeast, where the main focus has been the HOG pathway, which deals with hyperosmotic conditions. The cellular response has been followed either via brightfield images, where information on the volume changes of cells are extracted, or through fluorescence images where the spatio-temporal distributions of fluorescent proteins inside the cells are followed in real time.

The approach where the flows are stationary and the cells are moved with the optical tweezers is highly precise, allowing the environment to be changed in less than 0.2 s. The cells are completely surrounded by media, which could potentially be important, for instance, when the temporal shrinking of yeast cells is investigated. Another advantage is that once an experiment is completed the trapped cells can be released, and a new experiment can be started immediately. Alternatively, with an extension to the current microfluidic design, the cells could be brought to another part of the chip for further experiments or analysis. A possible approach to increase the throughput was demonstrated through the use of a spatial light modulator, where several cells could be trapped in a holographic optical tweezers array and exposed to environmental changes simultaneously. The three dimensional manipulation possibilities offered with the holographic optical tweezers was also demonstrated to allow the temporal resolution to be increased, or to enable studies over longer periods of time due to the reduced photobleaching. This can be achieved by forcing the nuclei of all trapped cells to coincide with a single imaging plane, thus removing the need to acquire axial stacks of images to capture all relevant information at each point in time.

The other experimental approach, where cells are positioned in a measurement region on the bottom of the microfluidic device, using the optical tweezers, is more similar to other microfluidic approaches presented recently, e.g., [28, 29]. However, the incorporation of optical tweezers to such a microfluidic device removes the need to rely on random sedimentation for positioning of cells within the measurement region. The positioning using optical tweezers assures repeatability of experiments since cells can always be positioned at the same coordinates within the device fore identical experiments. In addition, the number of cells and the cell density within the measurement region can easily be controlled. This simplifies the subsequent image analysis and is advantageous for statistical purposes, since the number of cells in the images can be maximized without running the risk of cells being positioned so close that the image segmentation becomes difficult. If desired, the experiments can also be performed on a specific type of cells, selected from the population. Another advantage with this design is that the time point when the environment is changed is well defined and can be synchronized with the image acquisition. The environmental change is achieved in less than 2 s.

The work with both the experimental approach using the holographic optical tweezers array and the approach where cells are positioned on a surface strive towards making the collection of data more high throughput. However, there is naturally a trade-off between the throughput and the amount of detail that can be acquired. Capturing images with high spatial resolution, where single cells are to be followed over long periods of time with high temporal resolution, necessarily implies that the throughput will be lower.

The holographic optical tweezers array were introduced to the microfluidic approach using stationary flows, as a means to increase the throughput. As shown in the thesis, the 3D manipulation possible with holographic optical tweezers can be used to optimize the axial positions of the trapped cells relative to the image plane, allowing the time resolution to be improved compared with a situation where axial stacks of images are required to capture the information of interest. However, as also shown in the thesis, the slow update rate of nematic liquid crystal SLMs can present a problem when holographic optical tweezers are combined with a microfluidic device. This is due to the reduced stiffness of the optical traps while the hologram displayed on the SLM is updated. The issue of maintaining a constant stiffness of the optical trap is also relevant in holographic optical force measurements. This application is highly promising, since it allows forces in a biological system to be probed in many positions simultaneously. Also related to the application of holographic optical force measurement is the question of how small steps that can be achieved with holographic optical tweezers, which was also discussed in this thesis.

Quantitative experimental data regarding how single cells respond to environmental changes is highly requested, for instance, within the field of systems biology. When such data are combined with mathematical models it is possible to quantitatively predict the behavior of biological systems, which is desired in the aim of understanding the enormous complexity of biological networks. In this thesis I have demonstrated that optical tweezers, microfluidics and fluorescence microscopy can successfully be combined to acquire quantitative information with high spatial and temporal resolution of single cells exposed to environmental changes.

Chapter 8

Outlook

My work has enabled data on a single cell level upon environmental changes to be acquired. The data is recorded through images using fluorescence and brightfield microscopy. The next step, when such images can routinely be collected, is to quantify the images in a robust and reliable manner. There are many challenges related to the correct quantification of images like those acquired in this thesis. To start with, the cells must be properly segmented to separate the nucleus from the cytosol. This is perhaps most easily made using brightfield images. A budding cell should be dealt with as two separate cells if the bud has a nucleus. Further, the photobleaching render the quantification of proteins more difficult. Another issue is focus drift or other changes of the image focus, such as those resulting from size changes of cells due to the environmental change. A first step towards simplifying the image analysis of the nuclearization of proteins has been the introduction of a second fluorescent protein, mCherry, tagged to a nuclear protein. This allows the position of the nucleus to be defined before the environmental changes begin and hence when the GFP-tagged protein is not localized to the nucleus. Ideally, the image analysis should be performed simultaneously with the image acquisition, thus allowing cells with deviating behavior to be identified directly and possibly also extracted from the system for further analysis. The image analysis is indeed a non-trivial task and is often mentioned as the bottleneck that prevents microscopy from being a high-throughput tool [126].

Another possibility with both experimental approaches is that the extension of the design to allow several mutants or strains to be introduced to the experimental system is relatively straightforward. With an efficient and controllable method to load the HOTs array, different mutants can be studied simultaneously under identical environmental conditions. Since optical tweezers are used to actively position cells within the measurement region, the study of several mutants simultaneously is also possible with the second, surface based, approach. In both cases the only requirement is that the different mutants should be introduced to the microfluidic system such that they have no possibility of being mixed up, which could potentially be solved using separate inlets for each strain. Without an active positioning of cells, such as in systems relying on random sedimentation of cells, the study of several mutants side by side in a single experiment would be hard to achieve.

The experimental development has now come to the stage where the techniques can be used to help answer research questions within cell biology. Thus the experimental approaches developed in my work can now be used to collect more data allowing the kinetics of a variety of cellular signalling pathways to be elucidated. When combined with mathematical modelling within the field of systems biology, quantitative data offer the potential to provide a better understanding of basic cellular properties and behavior. A first step in this direction was presented in the thesis, where quantitative data on the behavior of cells subjected to osmotic stress was combined with mathematical modelling in order to estimate numerical values of biophysical properties. The HOG pathway is just one example of signalling pathways with many unanswered questions that could benefit from studies on a single cell level. In parallel, the continued development of the experimental approaches should aim to make the system more high throughput. However, there is necessarily a trade-off between the throughput and the temporal and spatial resolution of the acquired data.

The experimental approaches presented in this thesis are demonstrated on *S. cerevisiae*. However, they are not limited to yeast cells. In principle, the experimental approach should be applicable to all cells that allow to be trapped with the optical tweezers and to be suspended in a flow. For the second approach, there is also the requirement that the cells should be viable when positioned on a coated surface. In addition, there should be an optical read-out of the cellular response to the changing environmental conditions. Potential applications could be toxicology studies or drug screening applications using different types of mammalian cells.

Chapter 9

Acknowledgements

There are many people that I wish to thank who have helped me to complete this thesis. Although I do not mention you all by name, you are not forgotten - thank you all!

First of all I wish to thank my supervisor Mattias Goksör for your endless support and sincere interest in my work throughout my entire Ph.D. You were a great support even before you took over the responsibility for supervising me. Thank you for always encouraging me to push my limits. Thanks also for creating such a nice working environment, I really like going to work!

Also a big thank you to my first supervisor, and later my examiner, Dag Hanstorp for giving me the opportunity to work on this project and introducing me to scientific research. Thanks for always being so positive and seeing opportunities rather than problems.

Without the help and support from Jonas Enger I would definitely not have got started so quickly in the lab. Thanks for helping me solve all kinds of practical problems in the lab and for introducing me to all the initially rather scary equipment.

Thanks also to the rest of the group, both present and former members! In particular I wish to thank Rikard and Kristin, who have been my roommates for several years. You contribute to a very nice atmosphere in the group! Thanks also to the people in the other groups within the Centre for Biophysical Imaging.

I also wish to thank Elzbieta Petelenz, with whom I spent many fun hours both in the lab and privately. Thanks for always taking your time to answer my questions regarding the biology of yeast, even though I probably asked the same questions many times before... And thank you for supplying me with Polish specialities from time to time, the pastry in the middle of my thesis writing was greatly appreciated!

Rose-Marie Wikström, the best head of administration ever. I am sure that without you this department would not function at all!

My thanks also goes to the three Martins, who took good care of me when I was new and introduced me to the life as a Ph.D. student! Thanks also to the rest of the former atomic physics group.

Mats Rostedt, for always solving all my computer related problems, regardless of it being an exchange of my hard drive in the middle of my thesis writing, configuring the serial ports on a Mac, or for getting access to more computational power for my numerical simulations. Thank you!

Thanks to Jan-Åke Wiman, who helped me construct and fabricate a number of tools and parts for my experimental setup.

Thanks also to Miles Padgett, Stephen Keen, Jonathan Leach and all the other people in the Optics group at the University of Glasgow, who made my visit in the group such a nice memory. Even though I was only there for a few months, you really made me feel as part of the group!

Thanks also goes to Stefan Hohmann, Thomas Nyström and all the other people at the Department of Cell and Molecular Biology with whom I have had fruitful collaborations with. Thanks also to all other co-authors during the years.

I am also grateful to Sheila Galt, first my examiner for my master's thesis and then one of my co-supervisors during my Ph.D. Thank you for always being so positive and supportive.

I also wish to thank Oliver Garner at Leica Microsystems, who always has been keen on digging out the information I requested regarding all obscure parts of the microscope, and for being genuinely interested in the development of our experimental setup.

Another person I wish to thank is my mentor Inger Jansson, who have given me much support and valuable thoughts regarding my Ph.D and my future career. Thanks also to all the other girls in the mentor program. We really had a fun time together!

Thanks to all the badminton players, for making me staying (reasonably) fit during my Ph.D!

Thanks also to Lars Weiner, Carl Egefeldt and Jonas Karlsson - my mathematics and physics teachers at Tranemo Gymnsieskola. Without you I wouldn't have chosen to study physics at the university in the first place!

Thanks also to all my friends who contribute to a rich life outside work.

Finally I am very grateful for the support from my family: mum and Jan-Olof, dad and Clarence, and my sister Karin. I also want to thank my grandfather Gösta, who is endlessly proud of me doing a Ph.D.

Bibliography

[1] B. F. Brehm-Stecher and E. A. Johnson. Single-cell microbiology: Tools, technologies, and applications. *Microbiology and Molecular Biology Reviews*, 68(3):538–559, 2004.

[2] H. A. Svahn and A. van den Berg. Single cells or large populations? *Lab on a Chip*, 7(5):544–546, 2007.

[3] D. Longo and J. Hasty. Dynamics of single-cell gene expression. *Molecular Systems Biology*, 2:64, 2006.

[4] D. Di Carlo and L. P. Lee. Dynamic single-cell analysis for quantitative biology. *Analytical Chemistry*, 78(23):7918–7925, 2006.

[5] H. Kitano. Systems biology: A brief overview. *Science*, 295(5560):1662–1664, 2002.

[6] J. R. S. Newman, S. Ghaemmaghami, J. Ihmels, D. K. Breslow, M. Noble, J. L. DeRisi, and J. S. Weissman. Single-cell proteomic analysis of *S. cerevisiae* reveals the architecture of biological noise. *Nature*, 441(7095):840–846, 2006.

[7] J. Ansel, H. Bottin, C. Rodriguez-Beltran, C. Damon, M. Nagarajan, S. Fehrmann, J. Francois, and G. Yvert. Cell-to-cell stochastic variation in gene expression is a complex genetic trait. *PLoS Genetics*, 4(4):e1000049, 2008.

[8] Z. Darzynkiewicz, E. Bedner, X. Li, W. Gorczyca, and M. R. Melamed. Laser-scanning cytometry: A new instrumentation with many applications. *Experimental Cell Research*, 249(1):1–12, 1999.

[9] I. Biran and D. R. Walt. Optical imaging fiber-based single live cell arrays: A high-density cell assay platform. *Analytical Chemistry*, 74(13):3046–3054, 2002.

[10] S. Lindstrom, R. Larsson, and H. A. Svahn. Towards high-throughput single cell/clone cultivation and analysis. *Electrophoresis*, 29(6):1219–1227, 2008.

[11] K. R. King, S. H. Wang, D. Irimia, A. Jayaraman, M. Toner, and M. L. Yarmush. A high-throughput microfluidic real-time gene expression living cell array. *Lab on a Chip*, 7(1):77–85, 2007.

[12] R. J. Taylor, D. Falconnet, A. Niemistö, S. A. Ramsey, S. Prinz, I. Shmulevich, T. Galitski, and C. L. Hansen. Dynamic analysis of MAPK signaling using a high-throughput microfluidic single-cell imaging platform. *Proceedings of the National Academy of Sciences of the United States of America*, 106(10):3758–3763, 2009.

[13] Dina Petranovic and Jens Nielsen. Can yeast systems biology contribute to the understanding of human disease? *Trends in Biotechnology*, 26(11):584–590, 2008.

[14] Z. E. Perlman, M. D. Slack, Y. Feng, T. J. Mitchison, L. F. Wu, and S. J. Altschuler. Multidimensional drug profiling by automated microscopy. *Science*, 306(5699):1194–1198, 2004.

[15] Y. Shav-Tal, R. H. Singer, and X. Darzacq. Imaging gene expression in single living cells. *Nature Reviews Molecular Cell Biology*, 5(10):855–862, 2004.

[16] N. C. Shaner, P. A. Steinbach, and R. Y. Tsien. A guide to choosing fluorescent proteins. *Nature Methods*, 2(12):905–909, 2005.

[17] A. Miyawaki, A. Sawano, and T. Kogure. Lighting up cells: labelling proteins with fluorophores. *Nature Reviews Molecular Cell Biology*, pages S1–S7, 2003.

[18] The official web site of the Nobel foundation. www.nobelprize.org, 2008-11-23.

[19] M. B. Elowitz, A. J. Levine, E. D. Siggia, and P. S. Swain. Stochastic gene expression in a single cell. *Science*, 297(5584):1183–1186, 2002.

[20] J. M. Raser and E. K. O'Shea. Control of stochasticity in eukaryotic gene expression. *Science*, 304(5678):1811–1814, 2004.

[21] J. Yu, J. Xiao, X. J. Ren, K. Q. Lao, and X. S. Xie. Probing gene expression in live cells, one protein molecule at a time. *Science*, 311(5767):1600–1603, 2006.

[22] J. Elf, G. W. Li, and X. S. Xie. Probing transcription factor dynamics at the single-molecule level in a living cell. *Science*, 316(5828):1191–1194, 2007.

[23] L. Cai, C. K. Dalal, and M. B. Elowitz. Frequency-modulated nuclear localization bursts coordinate gene regulation. *Nature*, 455(7212):485–490, 2008.

[24] J. El-Ali, P. K. Sorger, and K. F. Jensen. Cells on chips. *Nature*, 442(7101):403–411, 2006.

[25] S. Takayama, E. Ostuni, P. LeDuc, K. Naruse, D. E. Ingber, and G. M. Whitesides. Laminar flows - subcellular positioning of small molecules. *Nature*, 411(6841):1016–1016, 2001.

[26] J.W Bigger. Treatment of staphylococcal infections with penicillin - by intermittent sterilisation. *The Lancet*, 244(6320):497–500, 1944.

[27] N. Q. Balaban, J. Merrin, R. Chait, L. Kowalik, and S. Leibler. Bacterial persistence as a phenotypic switch. *Science*, 305(5690):1622–1625, 2004.

[28] J. T. Mettetal, D. Muzzey, C. Gomez-Uribe, and A. van Oudenaarden. The frequency dependence of osmo-adaptation in *Saccharomyces cerevisiae*. *Science*, 319:482–484, 2008.

[29] P. Hersen, M. N. McClean, L. Mahadevan, and S. Ramanathan. Signal processing by the HOG MAP kinase pathway. *Proceedings of the National Academy of Sciences of the United States of America*, 105(20):7165–7170, 2008.

[30] M. R. Bennett, W. L. Pang, N. A. Ostroff, B. L. Baumgartner, S. Nayak, L. S. Tsimring, and J. Hasty. Metabolic gene regulation in a dynamically changing environment. *Nature*, 454(7208):1119–1122, 2008.

[31] D. Di Carlo, L. Y. Wu, and L. P. Lee. Dynamic single cell culture array. *Lab on a Chip*, 6(11):1445–1449, 2006.

[32] J. Ryley and O. M. Pereira-Smith. Microfluidics device for single cell gene expression analysis in *Saccharomyces cerevisiae*. *Yeast*, 23(14-15):1065–1073, 2006.

[33] A. R. Wheeler, W. R. Throndset, R. J. Whelan, A. M. Leach, R. N. Zare, Y. H. Liao, K. Farrell, I. D. Manger, and A. Daridon. Microfluidic device for single-cell analysis. *Analytical Chemistry*, 75(14):3581–3586, 2003.

[34] A. Ashkin and J. M. Dziedzic. Optical trapping and manipulation of viruses and bacteria. *Science*, 235(4795):1517–1520, 1987.

[35] A. Ashkin, J. M. Dziedzic, and T. Yamane. Optical trapping and manipulation of single cells using infrared-laser beams. *Nature*, 330(6150):769–771, 1987.

[36] J. R. Moffitt, Y. R. Chemla, S. B. Smith, and C. Bustamante. Recent advances in optical tweezers. *Annual Review of Biochemistry*, 77:205–228, 2008.

[37] H. Zhang and K. K. Liu. Optical tweezers for single cells. *Journal of the Royal Society Interface*, 5(24):671–690, 2008.

[38] M. Ericsson, D. Hanstorp, P. Hagberg, J. Enger, and T. Nystrom. Sorting out bacterial viability with optical tweezers. *Journal of Bacteriology*, 182(19):5551–5555, 2000.

[39] L. Sacconi, I. M. Tolic-Norrelykke, C. Stringari, R. Antolini, and F. S. Pavone. Optical micromanipulations inside yeast cells. *Applied Optics*, 44(11):2001–2007, 2005.

[40] I. M. Tolic-Norrelykke, L. Sacconi, C. Stringari, I. Raabe, and F. S. Pavone. Nuclear and division-plane positioning revealed by optical micromanipulation. *Current Biology*, 15(13):1212–1216, 2005.

[41] N. Arneborg, H. Siegumfeldt, G. H. Andersen, P. Nissen, V. R. Daria, P. J. Rodrigo, and J. Gluckstad. Interactive optical trapping shows that confinement is a determinant of growth in a mixed yeast culture. *FEMS Microbiology Letters*, 245(1):155–159, 2005.

[42] P. M. P. Lanigan, K. Chan, T. Ninkovic, R. H. Templer, P. M. W. French, A. J. de Mello, K. R. Willison, P. J. Parker, M. A. A. Neil, O. Ces, and D. R. Klug. Spatially selective sampling of single cells using optically trapped fusogenic emulsion droplets: a new single-cell

proteomic tool. *Journal of the Royal Society Interface*, 5:S161–S168, 2008.

[43] P. M. P. Lanigan, T. Ninkovic, K. Chan, A. J. de Mello, K. R. Willison, D. R. Klug, R. H. Templer, M. A. A. Neil, and O. Ces. A microfluidic platform for probing single cell plasma membranes using optically trapped smart droplet microtools (SDMs). *Lab on a Chip*, (DOI: 10.1039/b816857a), 2009.

[44] M. Reicherter, T. Haist, E. U. Wagemann, and H. J. Tiziani. Optical particle trapping with computer-generated holograms written on a liquid-crystal display. *Optics Letters*, 24(9):608–610, 1999.

[45] A. Köhler. Gedanken zu einem neuen beleuchtungsverfahren für mikrophotographische zwecke. *Zeitschrift für wissenschaftliche Mikroskopie*, 10:433–440, 1893.

[46] K. Sott, E. Eriksson, E. Petelenz, and M. Goksor. Optical systems for single cell analyses. *Expert Opinion on Drug Discovery*, 3(11):1323–1344, 2008.

[47] Invitrogen Corp. www.invitrogen.com, 2008-11-23.

[48] J. W. Lichtman and J. A. Conchello. Fluorescence microscopy. *Nature Methods*, 2(12):910–919, 2005.

[49] L. D. Lavis and R. T. Raines. Bright ideas for chemical biology. *ACS Chemical Biology*, 3(3):142–155, 2008.

[50] D. C. Prasher, V. K. Eckenrode, W. W. Ward, F. G. Prendergast, and M. J. Cormier. Primary structure of the *Aequorea victoria* green-fluorescent protein. *Gene*, 111(2):229–233, 1992.

[51] M. Chalfie, Y. Tu, G. Euskirchen, W. W. Ward, and D. C. Prasher. Green fluorescent protein as a marker for gene-expression. *Science*, 263(5148):802–805, 1994.

[52] R. N. Day and F. Schaufele. Fluorescent protein tools for studying protein dynamics in living cells: a review. *Journal of Biomedical Optics*, 13(3), 2008.

[53] R. Y. Tsien. The green fluorescent protein. *Annual Review of Biochemistry*, 67:509–544, 1998.

[54] N. C. Shaner, G. H. Patterson, and M. W. Davidson. Advances in fluorescent protein technology. *Journal of Cell Science*, 120(24):4247–4260, 2007.

[55] S. D. Kohlwein. The beauty of the yeast: Live cell microscopy at the limits of optical resolution. *Microscopy Research and Technique*, 51(6):511–529, 2000.

[56] N. C. Shaner, M. Z. Lin, M. R. McKeown, P. A. Steinbach, K. L. Hazelwood, M. W. Davidson, and R. Y. Tsien. Improving the photostability of bright monomeric orange and red fluorescent proteins. *Nature Methods*, 5(6):545–551, 2008.

[57] K.R. Spring. Fluorescence microscopy. In *Encyclopedia of Optical Engineering*. Marcel Dekker, Inc., New York, 2003.

[58] Semrock IDEX Corporation. http://www.semrock.com, 2008-12-03.

[59] M. Abramowitz. Microscope basics and beyond. volume 1. Olympus America Inc., New York, 2003.

[60] S. K. Sia and G. M. Whitesides. Microfluidic devices fabricated in poly(dimethylsiloxane) for biological studies. *Electrophoresis*, 24(21):3563–3576, 2003.

[61] D. B. Weibel, W. R. DiLuzio, and G. M. Whitesides. Microfabrication meets microbiology. *Nature Reviews Microbiology*, 5(3):209–218, 2007.

[62] H. Andersson and A. van den Berg. Microfluidic devices for cellomics: a review. *Sensors and Actuators B-Chemical*, 92(3):315–325, 2003.

[63] A. L. Paguirigan and D. J. Beebe. Microfluidics meet cell biology: Bridging the gap by validation and application of microscale techniques for cell biological assays. *Bioessays*, 30(9):811–821, 2008.

[64] S. Pennathur. Flow control in microfluidics: Are the workhorse flows adequate? *Lab on a Chip*, 8(3):383–387, 2008.

[65] J. C. McDonald, D. C. Duffy, J. R. Anderson, D. T. Chiu, H. K. Wu, O. J. A. Schueller, and G. M. Whitesides. Fabrication of microfluidic systems in poly(dimethylsiloxane). *Electrophoresis*, 21(1):27–40, 2000.

[66] D. C. Duffy, J. C. McDonald, O. J. A. Schueller, and G. M. Whitesides. Rapid prototyping of microfluidic systems in poly(dimethylsiloxane). *Analytical Chemistry*, 70(23):4974–4984, 1998.

[67] D. J. Beebe, G. A. Mensing, and G. M. Walker. Physics and applications of microfluidics in biology. *Annual Review of Biomedical Engineering*, 4:261–286, 2002.

[68] E. M. Purcell. Life at low Reynolds-number. *American Journal of Physics*, 45(1):3–11, 1977.

[69] J. P. Brody, P. Yager, R. E. Goldstein, and R. H. Austin. Biotechnology at low Reynolds numbers. *Biophysical Journal*, 71(6):3430–3441, 1996.

[70] G. M. Walker, H. C. Zeringue, and D. J. Beebe. Microenvironment design considerations for cellular scale studies. *Lab on a Chip*, 4(2):91–97, 2004.

[71] T. M. Squires and S. R. Quake. Microfluidics: Fluid physics at the nanoliter scale. *Reviews of Modern Physics*, 77(3):977–1026, 2005.

[72] A. E. Kamholz and P. Yager. Theoretical analysis of molecular diffusion in pressure-driven laminar flow in microfluidic channels. *Biophysical Journal*, 80(1):155–160, 2001.

[73] P. Tabeling. *Introduction to Microfluidics*. Oxford University Press Inc., New York, 2005.

[74] R. F. Ismagilov, A. D. Stroock, P. J. A. Kenis, G. Whitesides, and H. A. Stone. Experimental and theoretical scaling laws for transverse diffusive broadening in two-phase laminar flows in microchannels. *Applied Physics Letters*, 76(17):2376–2378, 2000.

[75] A. E. Kamholz and P. Yager. Molecular diffusive scaling laws in pressure-driven microfluidic channels: deviation from one-dimensional Einstein approximations. *Sensors and Actuators B-Chemical*, 82(1):117–121, 2002.

[76] A. Ashkin, J. M. Dziedzic, J. E. Bjorkholm, and S. Chu. Observation of a single-beam gradient force optical trap for dielectric particles. *Optics Letters*, 11(5):288–290, 1986.

[77] K. C. Neuman, E. H. Chadd, G. F. Liou, K. Bergman, and S. M. Block. Characterization of photodamage to *Escherichia coli* in optical traps. *Biophysical Journal*, 77(5):2856–2863, 1999.

[78] H. Schneckenburger, A. Hendinger, R. Sailer, M. H. Gschwend, W. S. L. Strauss, M. Bauer, and K. Schutze. Cell viability in optical tweezers: high power red laser diode versus Nd:YAG laser. *Journal of Biomedical Optics*, 5(1):40–44, 2000.

[79] H. Liang, K. T. Vu, P. Krishnan, T. C. Trang, D. Shin, S. Kimel, and M. W. Berns. Wavelength dependence of cell cloning efficiency after optical trapping. *Biophysical Journal*, 70(3):1529–1533, 1996.

[80] U. Mirsaidov, W. Timp, K. Timp, M. Mir, P. Matsudaira, and G. Timp. Optimal optical trap for bacterial viability. *Physical Review E*, 78(2):7, 2008.

[81] M. Goksor, J. Enger, and D. Hanstorp. Optical manipulation in combination with multiphoton microscopy for single-cell studies. *Applied Optics*, 43(25):4831–4837, 2004.

[82] J. Enger, M. Goksor, K. Ramser, P. Hagberg, and D. Hanstorp. Optical tweezers applied to a microfluidic system. *Lab on a Chip*, 4(3):196–200, 2004.

[83] G. Whyte, G. Gibson, J. Leach, M. Padgett, D. Robert, and M. Miles. An optical trapped microhand for manipulating micron-sized objects. *Optics Express*, 14(25):12497–12502, 2006.

[84] J. Liesener, M. Reicherter, T. Haist, and H. J. Tiziani. Multifunctional optical tweezers using computer-generated holograms. *Optics Communications*, 185(1-3):77–82, 2000.

[85] M. Reicherter, S. Zwick, T. Haist, C. Kohler, H. Tiziani, and W. Osten. Fast digital hologram generation and adaptive force measurement in liquid-crystal-display-based holographic tweezers. *Applied Optics*, 45(5):888–896, 2006.

[86] F. Belloni, S. Monneret, F. Monduc, and M. Scordia. Multiple holographic optical tweezers parallel calibration with optical potential well characterization. *Optics Express*, 16(12):9011–9020, 2008.

[87] A. van der Horst and N. R. Forde. Calibration of dynamic holographic optical tweezers for force measurements on biomaterials. *Optics Express*, 16(25):20987–21003, 2008.

[88] J. E. Curtis and J. P. Spatz. Getting a grip: Hyaluronan-mediated cellular adhesion. In *Proceedings of SPIE*, volume 5514, pages 455–466, 2004.

[89] G. M. Akselrod, W. Timp, U. Mirsaidov, Q. Zhao, C. Li, R. Timp, K. Timp, P. Matsudaira, and G. Timp. Laser-guided assembly of heterotypic three-dimensional living cell microarrays. *Biophysical Journal*, 91(9):3465–3473, 2006.

[90] P. Jordan, J. Leach, M. Padgett, P. Blackburn, N. Isaacs, M. Goksor, D. Hanstorp, A. Wright, J. Girkin, and J. Cooper. Creating permanent 3D arrangements of isolated cells using holographic optical tweezers. *Lab on a Chip*, 5(11):1224–1228, 2005.

[91] K. Uhrig, R. Kurre, C. Schmitz, J. E. Curtis, T. Haraszti, A. E. M. Clemen, and J. P. Spatz. Optical force sensor array in a microfluidic device based on holographic optical tweezers. *Lab on a Chip*, 9(5):661–668, 2009.

[92] U. Mirsaidov, J. Scrimgeour, W. Timp, K. Beck, M. Mir, P. Matsudaira, and G. Timp. Live cell lithography: Using optical tweezers to create synthetic tissue. *Lab on a Chip*, 8(12):2174–2181, 2008.

[93] K. C. Neuman and S. M. Block. Optical trapping. *Review of Scientific Instruments*, 75(9):2787–2809, 2004.

[94] A. Ashkin. Forces of a single-beam gradient laser trap on a dielectric sphere in the ray optics regime. *Biophysical Journal*, 61(2):569–582, 1992.

[95] W. M. Lee, P. J. Reece, R. F. Marchington, N. K. Metzger, and K. Dholakia. Construction and calibration of an optical trap on a fluorescence optical microscope. *Nature Protocols*, 2(12):3226–3238, 2007.

[96] E. Fallman and O. Axner. Design for fully steerable dual-trap optical tweezers. *Applied Optics*, 36(10):2107–2113, 1997.

[97] S. Keen, J. Leach, G. Gibson, and M. J. Padgett. Comparison of a high-speed camera and a quadrant detector for measuring displacements in optical tweezers. *Journal of Optics A-Pure and Applied Optics*, 9(8):S264–S266, 2007.

[98] N. Mukohzaka, N. Yoshida, H. Toyoda, Y. Kobayashi, and T. Hara. Diffraction efficiency analysis of a parallel-aligned nematic-liquid-crystal spatial light-modulator. *Applied Optics*, 33(14):2804–2811, 1994.

[99] K. D. Wulff, D. G. Cole, R. L. Clark, R. DiLeonardo, J. Leach, J. Cooper, G. Gibson, and M. J. Padgett. Aberration correction in holographic optical tweezers. *Optics Express*, 14(9):4169–4174, 2006.

[100] A. Jesacher, A. Schwaighofer, S. Furhapter, C. Maurer, S. Bernet, and M. Ritsch-Marte. Wavefront correction of spatial light modulators using an optical vortex image. *Optics Express*, 15(9):5801–5808, 2007.

[101] W. J. Hossack, E. Theofanidou, J. Crain, K. Heggarty, and M. Birch. High-speed holographic optical tweezers using a ferroelectric liquid crystal microdisplay. *Optics Express*, 11(17):2053–2059, 2003.

[102] A. Jesacher, S. Furhapter, S. Bernet, and M. Ritsch-Marte. Diffractive optical tweezers in the Fresnel regime. *Optics Express*, 12(10):2243–2250, 2004.

[103] M. Polin, K. Ladavac, S. H. Lee, Y. Roichman, and D. G. Grier. Optimized holographic optical traps. *Optics Express*, 13(15):5831–5845, 2005.

[104] E. R. Dufresne, G. C. Spalding, M. T. Dearing, S. A. Sheets, and D. G. Grier. Computer-generated holographic optical tweezer arrays. *Review of Scientific Instruments*, 72(3):1810–1816, 2001.

[105] J. E. Curtis, C. H. J. Schmitz, and J. P. Spatz. Symmetry dependence of holograms for optical trapping. *Optics Letters*, 30(16):2086–2088, 2005.

[106] J. E. Curtis, B. A. Koss, and D. G. Grier. Dynamic holographic optical tweezers. *Optics Communications*, 207(1-6):169–175, 2002.

[107] J. Leach, K. Wulff, G. Sinclair, P. Jordan, J. Courtial, L. Thomson, G. Gibson, K. Karunwi, J. Cooper, Z. J. Laczik, and M. Padgett. Interactive approach to optical tweezers control. *Applied Optics*, 45(5):897–903, 2006.

[108] C. H. J. Schmitz, J. P. Spatz, and J. E. Curtis. High-precision steering of multiple holographic optical traps. *Optics Express*, 13(21):8678–8685, 2005.

[109] E. Hallstig, L. Sjoqvist, and M. Lindgren. Intensity variations using a quantized spatial light modulator for nonmechanical beam steering. *Optical Engineering*, 42(3):613–619, 2003.

[110] D. Engstrom, J. Bengtsson, E. Eriksson, and M. Goksor. Improved beam steering accuracy of a single beam with a 1D phase-only spatial light modulator. *Optics Express*, 16(22):18275–18287, 2008.

[111] V. Emiliani, D. Sanvitto, M. Zahid, F. Gerbal, and M. Coppey-Moisan. Multi force optical tweezers to generate gradients of forces. *Optics Express*, 12(17):3906–3910, 2004.

[112] B. Alberts, D. Bray, K. Hopkin, A. Johnson, J. Lewis, M. Raff, K. Roberts, and P. Walter. *Essential cell biology.* Garland Science, New York, 2nd edition, 2004.

[113] B. H. Judd. Experimental organisms used in genetics. In *Encyclopedia of Life Sciences.* John Wiley & Sons, Ltd, Chichester, 2001.

[114] A. Goffeau, B. G. Barrell, H. Bussey, R. W. Davis, B. Dujon, H. Feldmann, F. Galibert, J. D. Hoheisel, C. Jacq, M. Johnston, E. J. Louis, H. W. Mewes, Y. Murakami, P. Philippsen, H. Tettelin, and S. G. Oliver. Life with 6000 genes. *Science*, 274(5287):546, 563–567, 1996.

[115] J.C. Mell and S.M. Burgess. Yeast as a model organism. In *Encyclopedia of Life Sciences.* John Wiley & Sons, Ltd, Chichester, 2003.

[116] D. Botstein, S. A. Chervitz, and J. M. Cherry. Genetics - yeast as a model organism. *Science*, 277(5330):1259–1260, 1997.

[117] T. Kataoka, S. Powers, S. Cameron, O. Fasano, M. Goldfarb, J. Broach, and M. Wigler. Functional homology of mammalian and yeast RAS genes. *Cell*, 40(1):19–26, 1985.

[118] C.A. Michels. Genetic techniques of biological research. John Wiley and Sons, Ltd, 2002.

[119] P. Gervais, P. Molin, P. A. Marechal, and C. HerailFoussereau. Thermodynamics of yeast cell osmoregulation: Passive mechanisms. *Journal of Biological Physics*, 22(2):73–86, 1996.

[120] V. Reiser, D. C. Raitt, and H. Saito. Yeast osmosensor Sln1 and plant cytokinin receptor Cre1 respond to changes in turgor pressure. *Journal of Cell Biology*, 161(6):1035–1040, 2003.

[121] S. M. O'Rourke, I. Herskowitz, and E. K. O'Shea. Yeast go the whole HOG for the hyperosmotic response. *Trends in Genetics*, 18(8):405–412, 2002.

[122] V. Reiser, H. Ruis, and G. Ammerer. Kinase activity-dependent nuclear export opposes stress-induced nuclear accumulation and retention of Hog1 mitogen-activated protein kinase in the budding yeast *Saccharomyces cerevisiae*. *Molecular Biology of the Cell*, 10(4):1147–1161, 1999.

[123] H. Martin, M. Flandez, C. Nombela, and M. Molina. Protein phosphatases in MAPK signalling: we keep learning from yeast. *Molecular Microbiology*, 58(1):6–16, 2005.

[124] E. Klipp, B. Nordlander, R. Kruger, P. Gennemark, and S. Hohmann. Integrative model of the response of yeast to osmotic shock. *Nature Biotechnology*, 23(8):975–982, 2005.

[125] A. Gordon, A. Colman-Lerner, T. E. Chin, K. R. Benjamin, R. C. Yu, and R. Brent. Single-cell quantification of molecules and rates using open-source microscope-based cytometry. *Nature Methods*, 4(2):175–181, 2007.

[126] V. Starkuviene and R. Pepperkok. The potential of high-content high-throughput microscopy in drug discovery. *British Journal of Pharmacology*, 152(1):62–71, 2007.

Appendix A

Summary of the appended papers

The work presented in this thesis is highly interdisciplinary, covering topics both within physics and cell biology. This chapter provides a summary of the appended papers, with a focus on the technical developments that were made to enable the acquisition of the single cell data presented in chapter 6.

PAPER I demonstrates how a Y-shaped microfluidic device can be combined with optical tweezers and epi-fluorescence microscopy in order to change the environment of a single cell quickly and reversibly. A steep concentration gradient of NaCl or t-BOOH is established within the device, which is possible due to the laminar flow in micron-scale devices, where two media that are combined into a single microfluidic channel mix only due to diffusion. The gradient is characterized experimentally and verified with theory. By moving a single cell trapped with the optical tweezers transverse to the flow direction, i.e., across this stationary gradient, the environment is shown to be changed in less than 0.2 s, enabling the study of fast processes in the cell. This is demonstrated for a yeast cell subjected to changes of osmolarity of the surrounding medium, where the volume change due to the environmental change can be followed using image analysis. This volume information is relevant for the study of the HOG pathway. In addition we also demonstrate that the spatial redistribution of GFP-tagged proteins induced by the environmental change can be followed over time, thus demonstrating that intracellular processes can be followed *in vivo* using the experimental approach.

PAPER II further demonstrates how optical manipulation and microscopy can be combined with microfluidics in order to study single cell dynamics. In the work presented in this paper, optical tweezers are incorporated in microscope systems designed for epi-fluorescence microscopy, laser scanning microscopy and Raman spectroscopy. In particular, the applications of the experimental setup for studies of a number of cell signalling pathways in yeast are presented. The Y-shaped microfluidic device from **PAPER I** is replaced by a device with three inlet channels. To obtain a better understanding of the environment within the device, the concentration distribution is modelled using the basic equations describing fluid flow coupled to equations describing diffusive mixing. From the simulations the precise distance that a cell needs to be moved to make a complete change of environment is extracted. The dependence of the width of the concentration gradient on the distance from the bottom of the device is also taken into account. In the simulation glucose is the substance that forms the concentration gradient, which is relevant for experiments on a signalling pathway dealing with glucose starvation. The possibility of including a spatial light modulator in the optical setup forming the optical tweezers in order to trap several cells simultaneously, as an approach to make the system more high throughput, is indicated. In addition, two other applications of optical tweezers combined with environmental changes are demonstrated; the oxygenation cycle in red blood cells is studied using Raman spectroscopy, and the association forces between membrane contact sites in *Pisum sativum* and *Arabidopsis thaliana* are investigated.

PAPER III demonstrates how an SLM can be incorporated into the optical setup in order to create several optical traps, thus enabling the study of several single cells in parallel subjected to the same environmental change. The microfluidic device contains three inlet channels that are combined into a single main channel where a temporally stationary concentration gradient is formed. The stress substance is NaCl, relevant for studies of the HOG pathway, and the corresponding concentration distribution within the microfluidic device is modelled numerically, in order to determine the correct distances that the cells should be moved to accomplish a complete environmental change. A 2D array of traps is created by displaying a phase hologram, calculated using a two-dimensional Gerchberg-Saxton algorithm, on the SLM. Environmental changes of yeast cells trapped in the array are demonstrated. The cells' response to the environmental change is monitored using a combination of brightfield and fluorescence microscopy, where both the shrinkage upon osmotic stress and the translocation of fluorescent proteins to the nuclei are followed.

PAPER IV presents a study of the effect of external forces on micron-sized particles trapped with dynamic holographic optical tweezers. Movement of particles trapped with holographic optical tweezers is achieved by updating the phase hologram displayed on the SLM (a parallel aligned nematic liquid crystal phase-only SLM with a range of 2π). The holograms consist of simple blazed gratings. The slow update rate of the SLM results in a relatively long weakening of the stiffness of the optical trap. This could present a problem if the trapped particle is simultaneously subjected to an external force, such as the Stokes drag force from a flow. In the worst case the particle could be lost during the hologram update. In this paper this problem is investigated in more detail, by measuring the displacement of a trapped bead from the equilibrium position during the hologram update, when stepping a particle in a direction transverse to the flow direction. We concluded that the temporary weakening of the trap was depending on the average phase shift per pixel between the two holograms. Thus, for applications where it is important to keep a constant trap stiffness, the trapped object should be moved with as small steps as allowed by the HOT setup, minimizing the phase shift between two consecutive holograms. However, when a quick movement of the trapped object is desired, a step size corresponding to the radius of the object is optimal. For larger steps the risk of loosing the trapped particle is more prominent, due to smaller restoring force of the optical trap.

PAPER V demonstrates how automated image analysis and hologram calculation can be used to bring different cellular features of interest, such as the nuclei, of cells trapped in a holographic optical tweezers array into a single imaging plane, by individually optimizing the axial position of each optical trap. This three dimensional positioning of cells is needed since cells tend to align differently within the optical traps depending on, e.g., size, shape and composition. In the approach presented, an axial stack of images of the trapped cells is first acquired by translating the trapped cells through the image plane by updating the hologram displayed on the SLM. The optimum axial position for each trap is identified from the images by determining in which image each cell is in focus. The corresponding axial coordinates are then used to calculate a new hologram, where the axial position of each cell is optimized to allow all cells or nuclei to be in focus in a single image. In time-lapse fluorescence imaging of single cells this procedure has the advantage that more relevant images can be taken before photobleaching becomes an issue. The approach therefore allows the temporal resolution to be increased, and/or enables imaging over longer periods of time.

PAPER VI demonstrates an alternative approach for accomplishing environmental changes of several cells simultaneously, still enabling information on a single cell level to be acquired over time. In this design cells are positioned in a measurement region on the bottom of the device using optical tweezers, and the environmental change is performed by changing the relative flow rates in the inlet channels. The positioning of cells is automated, enabling repeatability and control of the cell density in the measurement region. The system is demonstrated on a signalling pathway in yeast activated by changes in glucose supply, by monitoring the nuclearization of GFP-tagged proteins upon glucose addition using fluorescence microscopy. The concentration distributions in the two flow configurations representing presence and absence of glucose, respectively, are modelled from the basic equations describing fluid flow and diffusion. Also, the speed of the environmental change within the measurement region is evaluated experimentally, with the conclusion that the environment is completely changed in less than 2 s. To assure that the experimental procedure does not harm the cells a viability study of cells trapped with the optical tweezers was performed. In addition, the system was tested on a yeast strain with GFP tagged to a protein that localizes to the nucleus under numerous stress conditions. We could verify that the cells were not stressed at the start of the experiment, but that the protein translocated into the nucleus upon an environmental change, as expected. The system allows the environment to be changed back and forth as many times as desired, while the cells are monitored using brightfield and epi-fluorescence microscopy. To assure that all relevant information regarding the protein kinetics is captured, axial stacks of images are acquired at every time point.

PAPER VII presents a mathematical model of how turgor pressure and cell wall elasticity (and a few other biophysical and mechanical parameters) relate to the relative size of yeast cells subjected to an osmotic shock. This model was fitted to a number of experimental data sets measuring the volume change as a function of the osmolarity of the medium. One of these data sets is obtained by using the microfluidic system described in **PAPER VI**. The fitting of the model to the experimental data allow values on, e.g., turgor pressure and cell wall elasticity, to be estimated. In addition, the loss of turgor pressure could be related to the degree of activation of the HOG pathway, as measured by the localization of Hog1-GFP to the nucleus or by Western blotting of phosphorylated Hog1.

Appendix B

List of Abbreviations

ATP	Adenosine triphosphate
μTAS	Micro Total Analysis System
CCD	Charged Coupled Device
CFP	Cyan Fluorescent Protein
EMCCD	Electron Multiplier Charge-Coupled Device
FEM	Finite Element Method
FP	Fluorescent Protein
GFP	Green Fluorescent Protein
GMM	Gimbal Mounted Mirror
HOG	High Osmolarity Glycerol
HOTs	Holographic Optical Tweezers
LCS	Laser Scanning Cytometry
LOC	Lab on a Chip
NA	Numerical Aperture
OD	Optical Density
Pe	Péclet number
PCR	Polymerase Chain Reaction
PDMS	Poly(dimethylsiloxane)
PSD	Position Sensitive Detector
Re	Reynolds number
S. cerevisiae	*Saccharomyces cerevisiae*
SLM	Spatial Light Modulator
YFP	Yellow Fluorescent Protein
YNB	Yeast Nitrogen Base
YPD	Yeast Peptone Dextrose

Appendix C

Glossary

4-f configuration Two lenses of focal lengths f_1 and f_2, respectively, are said to be in a 4-f configuration if the spacing between them is $f_1 + f_2$. Thus an object placed in the front focal plane of the first lens is imaged onto the back focal plane of the second lens with a transverse magnification of $-f_2/f_1$.

Aberrations Deviations from the idealized conditions of Gaussian optics.

Acousto-optic modulator A device that can be used for spatial control of light beams, by deflecting the light using sound waves.

Afocal An optical system without a focal length. A collimated incoming laser beam will be collimated also after the optical system.

Aspect ratio The ratio of an objects longer dimension to its shorter dimension. The aspect ratio of a cross section of a microfluidic device of width w and height h has an aspect ratio of w/h if the width is the longer dimension.

ATP Adenosine triphosphate. The principal carrier of chemical energy within cells. When the terminal phosphate groups are hydrolyzed or transferred to another molecule, free energy is released.

Back focal length The distance from the last surface of a lens to its second focal point.

CCD Charged Coupled Device. A solid-state photo detector, which is composed of an array of light sensitive detectors.

Dichroic mirror A mirror used to selectively reflect light according to its wavelength.

Diffusion The spreading of particles as a result of random thermal motion.

Diploid A cell or organism with two sets of chromosomes.

Extrinsic noise Stochasticity in gene expression that gives rise to phenotypic variations. Extrinsic noise arises from factors that are global to a single cell, but that can vary from one cell to another.

Fluorescence The process of absorption of a photon, that excites a molecule to a higher energy level, and the subsequent emission of another photon.

Fluorophore or fluorochrome. A molecule that is able to fluoresce.

Front focal length The distance from the first surface of a lens to its first (object) focal point.

Gimbal mount A mount that allows a mirror to be tilted around its center position without any lateral translation.

Haploid A cell or organism with one set of chromosomes.

Holographic Optical Tweezers An extension of conventional optical tweezers based on diffractive optics, allowing, e.g., several traps to be created simultaneously. When implemented using a spatial light modulator the traps can be moved in close to real-time.

In vivo Experiments performed in living organisms.

Immersion oil An oil with the same refractive index as the cover glass that is applied between the microscope objective lens and the cover glass, in order to minimize geometric aberrations.

Intrinsic noise Intrinsic noise in gene expression regards the stochastic biochemical process of gene expression, and can be defined as the extent to which the activities of two identical copies of the same gene, in the same intracellular environment, fail to correlate.

Kinase An enzyme that transfers the terminal phosphate group of ATP to a substrate.

Laminar flow Laminar flow is a condition in which the flow pattern is predetermined, in contrast to turbulent flow.

Liquid crystal A liquid or liquid-like phase of matter that is anisotropic, making the material birefringent.

MAP kinase A specific protein kinase that respond to extracellular stimuli and transmit the signal intracellularly.

Microarrays A powerful tool that enables simultaneous (up to tens of thousands of genes) measurement of gene expression levels or detection of single nucleotide variations within a genome.

Microfluidics Microfluidics deals with miniaturized fluid handling devices, where at least one dimension is in the range of $10 - 500$ μm.

Molar extinction coefficient A measure of how strongly a chemical species, such as a fluorophore, absorbs light at the wavelength of maximum absorption. It is measured in units of $M^{-1}cm^{-1}$.

Nematic Liquid Crystal The nematic phase is the simplest liquid crystalline phase. Here the molecules have random positional order but are on the average oriented along a specific direction.

Numerical aperture A measure of the light gathering or light focusing capacity of an optical system.

Northern blotting A technique based on gel electrophoresis and mRNA detection (by the use of labelled single stranded DNA) to study and quantify specific RNA levels.

Optical Tweezers A tool based on a strongly focused laser beam that can be used to trap and manipulate small transparent objects, such as cells and bacteria, in three dimensions.

Optically conjugate planes Optical planes that are imaged onto each other.

Ortholog Genes in different species that have evolved from a common ancestral gene by speciation. Normally, orthologs retain the same function in the course of evolution.

Phenotype The morphological, biochemical and behavioral characteristics of an individual organism or cell. The phenotype is determined by both genetic and environmental factors.

Photobleaching The permanent photochemical destruction of a fluorophore.

Phosphatase An enzyme that removes a phosphate group from a substrate by hydrolysis.

Photolithography A lithography method that uses light to print a pattern in a photosensitive material.

Photoresist A photosensitive material that can be made insoluble via exposure to light.

Protein A linear polymer of amino acids in a specific sequence. Proteins are the main macromolecular constituents of cells.

Real-time PCR (PCR = Polymerase Chain Reaction) A kinetic approach used to determine and quantify gene expression, based on the amplification of DNA originating from mRNA. The amount of product measured after each cycle reflects the abundance of the analyzed template gene.

Reporter gene A reporter gene is used to follow gene expression *in vitro* and *in vivo*. The gene of interest is fused to a reporter gene which codes for a protein whose abundance can be easily assayed.

Repressor A protein that inhibits the expression of a particular gene or group of genes by preventing transcription.

Signal transduction A series of biochemical reactions in which a signal initiated at the cell surface is transmitted inside the cell and results in a cellular response.

Spatial Light Modulator An optical device capable of modulating the phase and/or the amplitude of light.

Systems Biology An interdisciplinary research field aiming at obtaining, analyzing and interpreting data from multiple experimental resources. Due to the enormous complexity of biological networks, quantitative and predictive mathematical models are used to explain the behavior of the system.

Transcription Factor A protein required to initiate or regulate gene transcription in eucaryotes.

Quantum yield The fraction of excited molecules that returns to the ground state via fluorescence.

Quenching Non-radiative relaxation of the excited fluorophore due to molecular collision, energy transfer, intersystem crossing or other processes. Leads temporarily to reduced fluorescence.

Wavefront The surface joining all points that have the same phase of the light, i.e., have the same optical path length from the source.

Western blotting A technique based on gel electrophoresis and protein detection (by the use of antibodies) to study and quantify specific protein levels.